RCA Review

High Transmission Focus Mask

September 1983 Volume 44 No. 3

RCARCI 44(3) 371-504 (1983)

The cover shows a scanning electron micrograph of part of the dipole-quadrupole focus mask described in the paper by Hockings, Bloom, and Tamutus in this issue of *RCA Review*. This mask, which is experimental, provides a highly transmitting color-selection structure requiring only moderate voltage biases. It has an electron-beam transmission of about 50% as compared to the 18–22% of a typical shadow mask. As shown, the mask consists of an aperture plate and conducting wires separated by an insulator (the undercut pads visible at crossover points) and is quite rugged.

RCA Review, published quarterly in March, June, September, and December by RCA Laboratories Princeton, New Jersey 08540. Entered as second class matter July 3, 1950 under the Act of March 3, 1879. Second-class postage paid at Princeton, New Jersey, and at additional mailing offices. Effective January 1, 1983, subscription rates as follows: United States: one year $12.00, two years $21.00, three years $27.00; in other countries: one year $14.00, two years $24.50, three years $31.50. Single copies up to five years old $5.00

RCA Review

RCA Review (ISSN 0033-6831) is a technical journal published quarterly by RCA Laboratories in cooperation with the subsidiaries and divisions of RCA.

Contents

September 1983 Volume 44 Number 3 ISSN 0033-6831

A High-Transmission Focus Mask for Color Picture Tubes

E. F. Hockings, S. Bloom, and D. J. Tamutus
RCA Laboratories, Princeton, NJ 08540

Abstract—The behavior of a dipole-quadrupole focus mask for a color picture tube is described. Some proposed methods of fabricating focus masks are reviewed. One method is described in detail since it was used to make a demountable focus mask color picture tube. The performance of this 10-inch diagonal tube is exemplified by a color illustration of a transmitted video image.

1. Introduction

The width of each shadow mask aperture in an in-line color picture tube may be no greater than one-third of the phosphor triad period. This limits the mask transmission to one-third of the incident electron beam, and in practice it is more like one-fifth. To avoid this waste of 80% of the beam at the shadow mask, many methods have been suggested for enlarging the apertures and for providing focusing as well as shadowing; and these methods have recently been discussed[1]. When for example the mask is maintained at several kilovolts below the screen potential, the mask apertures become convergent lenses with a focal power proportional to the axial electric field in the mask-to-screen region. However, these early post-deflection focusing systems had many problems, all arising because the mask was at a much lower potential than the screen. For example, contrast was degraded because unwanted electrons were accelerated to the screen; the overall beam spot was enlarged because the gun-to-mask region was at too low a voltage; and the large potential difference between the mask and screen led to arcing problems.

One form of early focus mask was the "single-grill" structure[2] in

which wires were stretched parallel to the phosphor stripes of a line-type screen. The forementioned problems were then alleviated by the "double-grill" modification, due to Ramberg et al,[3] in which a second array of wires was placed near and normal to the first set. With the two grills close together—about 1/8th inch in practice—a smaller potential difference can produce the required focal power. When the first grill (parallel to the line screen) is at screen potential and the second grill (transverse to the line screen) is at a higher potential, the electron beamlets through the composite rectangular openings are focused horizontally and defocused vertically. This double-grill focus mask, although adequate electron-optically, suffers critically from the mechanical problems of stretched wires.

More recently, quadrupole-type focus masks have been proposed.[4] In a sense, these are logical extensions of the double-grill mask in that the second grill is now brought close to the first grill and anchored to it by insulation at the intersections. With the two grill arrays now essentially coplanar, the electric field lines are almost wholly normal to the beam direction and so most effective in deflecting the electrons. Thus a potential difference of several hundred volts, rather than several kilovolts, suffices. Such low voltages are, of course, a requirement if the thin insulation at the intersections is to withstand breakdown.

Nevertheless, even this quadrupole focus mask, a now-integrated single structure of two orthogonal sets of wires, lacks the robustness and ease-of-handling required for a manufacturable focus mask. In this paper we describe a new design, the dipole-quadrupole focus mask, in which one set of wires of the quadrupole mask is replaced by a selfstanding aperture plate.

The presentation is organized as follows. In Section 2 the behavior of a dipole-quadrupole mask is described; Section 3 reviews past efforts and proposals for the fabrication of multipole-type focus masks of both electrostatic and magnetic varieties; in Section 4 the construction of the present dipole-quadrupole mask is described; the performance of this mask is discussed in Section 5; and Section 6 gives the conclusions.

2. The Dipole–Quadrupole Lens

A section of a dipole–quadrupole focus mask is shown schematically in Figure 1. Each aperture of the plate is bisected by a wire which is held at a potential V_o and is insulated from the plate which is held at $V_o + \Delta V$. Here V_o is the potential of the screen and gun. Each small opening of the composite structure is a lens in which

the two horizontal webs are at $V_o + \Delta V$ and the vertical webs are at $V_o + \Delta V$ and V_o.

If both vertical webs were at V_o, each lens would be a pure quadrupole. Then rays entering in the axial (z) direction at points a and b would be focused inward toward the z axis, and rays entering at points c would be defocused outward away from the axis. On the other hand, if the horizontal webs were absent, the remaining vertical webs would form a pure dipole lens. Then all rays in the yz plane would be bent the same amount toward the $V_o + \Delta V$ vertical web.

In the combination dipole–quadrupole lens of Fig. 1, the ray entering at a is bent strongly toward the left by the sum of the dipolar and quadrupolar forces. The ray at b is deflected more weakly to the left by the difference between the dipolar and quadrupolar forces. The quadrupolar force is only half as strong as it would be for this aperture if all vertical webs were at V_o. The bias voltage that causes the resultant spot width, D, at the screen to decrease to one-third of the phosphor triad period is called the color-purity mask focus voltage, ΔV_{cp}.

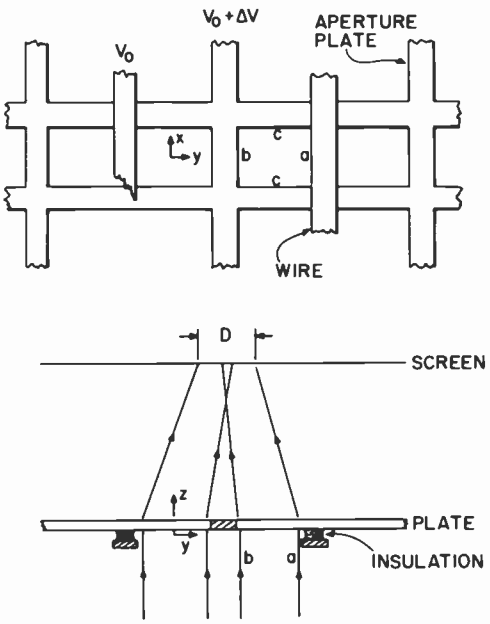

Fig. 1—Front and top views of a dipole-quadrupole focus mask.

3. Proposed Fabrication Method

Various methods of making focus mask structures have been described. These can be classified on the basis of the sequence of their fabrication procedures. The structures comprise conductors and insulators, each of which has to be patterned to produce the array of apertures that form the focus mask. The focus mask assembly procedure may involve either unpatterned or patterned metallic conductors combined with unpatterned or patterned insulators. The combinations of unpatterned-metal and unpatterned-insulator, patterned-metal and unpatterned-insulator, and patterned-metal and patterned-insulator will be used as the basis for the following classification of fabrication methods. The potential sequence of combining unpatterned metal with patterned insulator would require that the metal have a latent pattern, or at least registration or alignment marks, so that the subsequent metal patterning may be aligned to the patterned insulator; therefore this sequence will not be discussed. In addition, the use of patterned-metal and vacuum insulator will be described.

3.1 Unpatterned-Metal and Unpatterned-Insulator

The preparation of a metal–insulator–metal laminate may be followed by steps to pattern the metal and then to pattern the insulator. A focus mask made by this sequence, described by van Esdonk,[5] is composed of one aluminum layer and one nickel layer. One ferromagnetic metal is desired so as to screen the electron beam in the picture tube from the earth's magnetic field. The insulator is a polyimide sheet, such as Kapton, placed between the metal layers. The metal layers are patterned by photoresist followed by etching. Then the insulator is patterned by etching using the metals as resists. Isolated regions of insulator then remain wherever the metal arrays cross each other. No tube performance results have been presented.

Another method that starts with a metal–insulator–metal laminate has been described by Tamutus.[6] The insulator is a positive-acting photosoluble layer and the metal layers are laminated to it. The metal layers are patterned and etched, the structure exposed to light, and the unwanted regions of insulator are removed. Isolated regions of insulator then remain wherever the metal arrays cross each other. This method will be described below in greater detail, since it was used to make the focus mask for a demonstration color picture tube for which some results have been presented.[1]

3.2 Patterned-Metal and Unpatterned-Insulator

A mask made by laminating patterned-metal electrodes onto each side of a polyimide sheet was used by van Alphen and van den Berg[4] to demonstrate the performance of a quadrupole focus mask. The laminate is etched to remove the polyimide from the apertures using the metal grid electrodes as an etching mask. A small insulating stud then remains at each intersection of the metal grids. A method for fabricating a metal–insulator–metal laminate was described by van Esdonk.[7] He starts with an insulating sheet metalized on both sides and then bonds the metal electrode structures to the sheet by diffusion bonding. The insulator is then etched away from the windows of the electrode structure to give the desired focus mask. Another fabrication method has been described by van Oostrum.[8] Here a metal film is deposited upon an aperture-plate–insulator structure such that the desired electrode structures are formed on the walls of each aperture of the focus mask.

No video results have been presented for focus masks made by these methods.

3.3 Patterned-Metal and Patterned-Insulator

Many patents have described methods in which discrete regions of insulator are employed to join together patterned-metal electrodes. Ronde[9] uses insulating grains as spacers and these are bonded with an adhesive to the patterned metal conductors. An insulator of a glass core and a different glass jacket has been described by van Esdonk and Haans.[10] Here the glass core functions as a rigid spacer while the glass of the jacket can be softened to provide the bonding to the electrodes of the focus mask. Koorneef and der Kinderen[11] form one set of conductors around the other orthogonal set of conductors with insulator present at each intersection. Originally the insulator is along the entire length of each conductor; it is then removed from the structure except at the intersections. Another example of partial removal of a patterned insulator was described by van Alphen and Verweel[12] who use insulated wires that are woven to give a quadrupole focus mask assembly; the insulator is then removed from all places except at the intersections.

A method for making focus masks through the use of two sheets of conductors each with insulator-coated ridges has been described by Ronde and van Loosdregt.[13] The sheets are bonded and then the thin portions are etched away leaving an array of crossed, insulated wires. The fabrication of a cylindrical focus mask has been described

by Koorneef.[14] A sheet of polyimide insulator, with a conducting film on one side, is sliced into strips, and the strips are bonded to the webs of an aperture plate that forms the second electrode of the focus mask. An example in which conducting wires are applied so as to cross the apertures in a plate was described by van der Ven.[15] Here, discrete glass insulators are applied by frit techniques.

No tube results have been presented for focus masks made by these methods.

3.4 Patterned-Metal and Vacuum-Insulator

A focus mask color picture tube has been described by Takenaka, Hamano, and Kamohara.[16] They use two shadow masks spaced apart as the two electrodes in a focus mask tube. These masks each have apertures and ridges, and the masks are placed near each other with insulation only at the periphery. Within the active area of the focus mask assembly, the two masks are isolated by the vacuum in the picture tube. Operating conditions were described but tube performance was not.

3.5 Magnetic Quadrupole Masks

In addition to the quadrupole focus masks reviewed above, which are electrostatic, there are also magnetic quadrupole focus masks. One structure[17] uses two mutually perpendicular arrays of soft-magnet strips with hard-magnet disks as separators at the strip intersections; the disks are magnetized normal to the planes of the strips and so make one set of strips into north poles and one set into south poles, thus producing a quadrupole magnetic field in each aperture. In another scheme,[18] a very small magnetizing head is used to write magnetic quadrupoles around apertures in a thin hard-magnet sheet. A third version,[19] a variant of the first, uses two sets of mutually perpendicular hard-magnet strips on either side of a soft-magnet aperture plate. These magnetic focus masks have the advantage of requiring no bias voltage and having no breakdown problem; however, their focal power is not adjustable and they tend to have large overall thicknesses, leading to excessive vignetting. No picture tube results have been presented.

4. Fabrication of Experimental Dipole-Quadrupole Masks

The problems of mask forming and certain aspects of screen preparation were avoided in this work by the use of a flat mask and

screen. The maximum angle of incidence of the beam to the mask should correspond, for a meaningful evaluation, to that in the corners of a 25V 110° color picture tube. It was thought that a 10-inch mask would give a useful demonstration of focus mask behavior. A 10-inch dipole-quadrupole demonstration focus mask was fabricated using the unpatterned-metal and unpatterned-insulator laminate method.[6] The aperture horizontal period of the mask was selected to be 0.030-inch and the vertical period was 0.018-inch. Construction involved the lamination of four positive photoresist layers and two beryllium-copper sheets arranged as resist, metal, resist, resist, metal, and resist. The two outer layers of photoresist were used to pattern the metal for etching and the two inner layers of photoresist were used to provide sufficient electrical insulation between the two metal sheets.

Initially each piece of cleaned and degreased 0.002-inch beryllium-copper, approximately 10-inches square, was laminated on one side with a dry-film positive-acting photoresist. These two resist coatings will become the two inner electrically-insulating layers of the laminate. The mylar sheet used to protect the resist coating on each laminate was then removed and the two laminates were mildly baked to remove some of the excess solvents in the resist layers and to improve stability during later processing.

The two laminates were then cooled and placed photoresist to photoresist and passed through a dry film laminator, thereby laminating new photoresist layers on the top and the bottom of the structure. The speed at which this lamination was accomplished was sufficiently slow for the new photoresist to adhere to the metal sheets and for the inner two photoresist layers to adhere to each other. The laminate was then allowed to return to ambient temperature.

The protective mylar sheets on the outer photoresist layers were then removed and the structure was baked and again allowed to return to ambient. Although the baking procedure somewhat desensitized the photoresist, the formation of nitrogen bubbles in the resist during exposure was prevented. The laminate was now ready for patterning.

The photographic glass positives (photo-tool) used to pattern the photo-resist for etching the two sheets of beryllium-copper were suitably registered in an alignment fixture. With the protective mylar sheets repositioned on the photoresist, the laminate was then inserted into the double-sided aligned photo-tool and then into a double-sided exposure system and exposed. The exposed resists were

developed and the patterned metal was spray etched and then washed.

At this point, the two metal layers have been etched in registration to each other. The positive photoresist used to pattern the metal is still in place and the two inner layers of photoresist are also intact. The inner layers of photoresist completely span the apertures and are visible through the openings in the etched metal. All the photoresist that is visible has to be removed. Because this is a positive-acting photoresist, everything visible is exposed and then removed by developing. This removal requires that the photoresist withstand being baked and being in contact with an etchant, while still retaining some photosensitivity. A scanning electron micrograph of a portion of the finished focus mask is shown in Fig. 2. It can be seen that the insulation is undercut with respect to the metal.

The dry-film photoresist used in making this focus mask structure was an experimental material, and it was useful because it was positive acting, insulative, uniform in thickness, and could be laminated to itself.

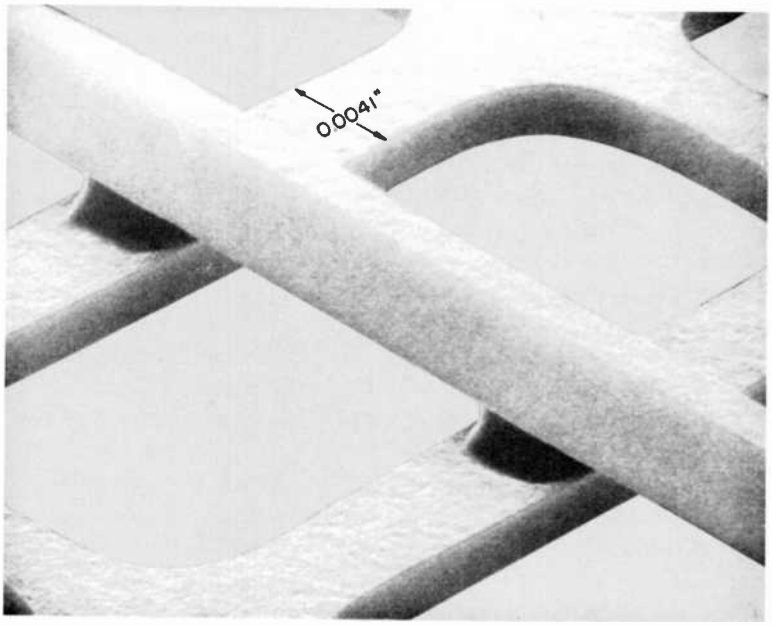

Fig. 2—Scanning electron micrograph of the dipole-quadrupole focus mask showing aperture plate, insulator, and conducting wire.

5. Mask Performance

5.1 Small Masks

The performance of dipole–quadrupole focus masks was first evaluated on small masks. As the mask focus voltage was increased, the beamlets through adjacent apertures were deflected into coincidence and partially focused. The appearance of the spots as the focus voltage was increased is shown in Fig. 3. Light intensity profiles were measured on the phosphor screen along a horizontal line through the centers of the spots with the results shown in Fig. 4. As the mask focus voltage was increased up to 260V the total width of the spots decreased linearly. For higher values of the mask focus voltage the width increased, as shown in Fig. 4 by the curve for 400V. The mask focus voltage for which the total spot width (5% of maximum) was one-third of the phosphor triad period can be seen to be about 210V. At this focus voltage it is then possible to achieve color purity of the display with three beams and three phosphor stripes. Tests were made at increasing angles of incidence and the focus voltage for color purity was found to decrease and to follow a

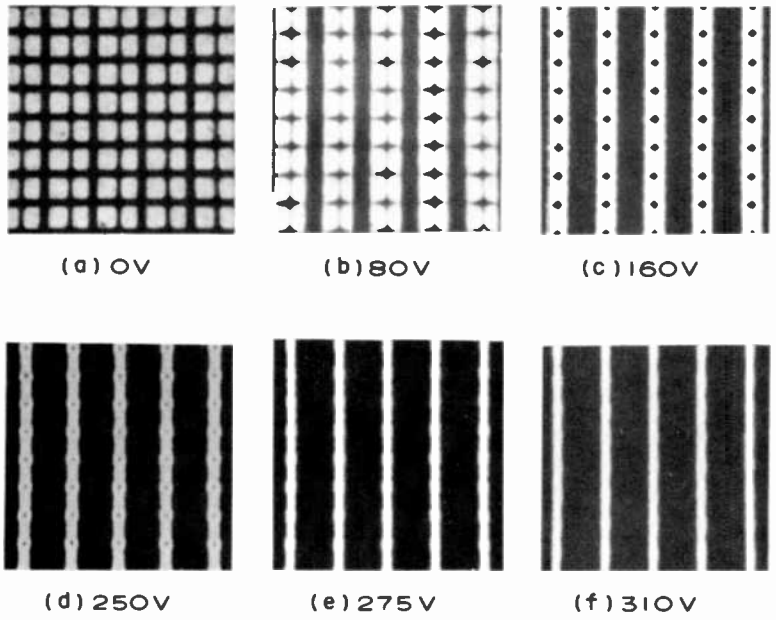

Fig. 3—Spots from a dipole-quadrupole mask for various mask focus voltages with V_o = 10kV. The mask horizontal period is 0.030 inch. For this mask the color purity voltage, ΔV_{cp}, is 210V.

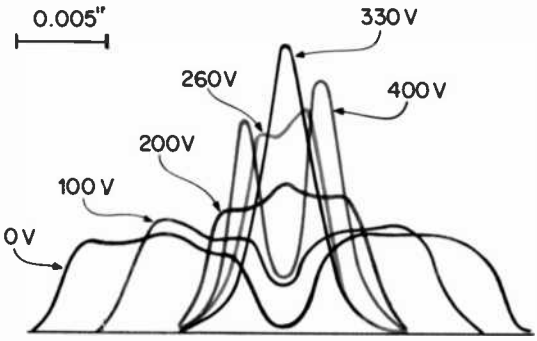

Fig. 4—Line profiles for the dipole-quadrupole mask of Fig. 3 for various mask focus voltages.

cosine-squared dependence upon the angle of incidence. The examination of many small masks showed that the photoresist used here had only moderate insulating capability and that it could not reliably hold off mask focus voltages greater than about 400V.

5.2 Design of Mask Evaluation Tube

The performance of the focus mask was evaluated in a demountable picture tube that was designed with the following constraints. A mask-to-screen spacing of 0.75-inch was selected as being one that would require a low mask focus voltage and thus would not impose a large electrical stress upon the mask insulation. The desired corner angle of incidence and the diagonal size gives a center-of-deflection to mask spacing of 6.6 inches. Since the aperture period on the mask had been selected as 0.030 inch, the phosphor triad period is 0.0334 inch. The breakdown limits of the photoresist insulation led to the restriction of the average mask potential to the vicinity of 10 kV. The vertical conducting wires of the mask were at 10.00kV, and at color purity the aperture plate was at 10.25kV for this particular mask.

The flat phosphor screen was prepared independently of the focus mask and had a line structure with a color triad period of 0.0334 inch. The position of the mask was adjusted with respect to the screen so that when no mask focus voltage was applied, i.e., when the mask was shadowed onto the screen, the mask shadow was aligned with respect to the phosphor stripes.

5.3 Demonstration Tube Results

The 10-inch focus mask demonstration tube was used to display transmitted video, and an example is shown in Fig. 5. A satisfactory picture was obtained with a combined average beam current of only 30 μA. The general vertical line structure just visible in Fig. 5 arises from the use of a screen with a 0.0334-inch period, which is conventional for a 25-inch tube, rather than a screen with a 0.026-inch period, which is conventional for a 10-inch tube. There appears to be no inherent limitation that would prevent the focus mask period from being reduced to the 0.0233-inch required to give a 0.026-inch screen period. There were no local distortions to the beam that might have arisen from any charging of the focus mask insulator.

Horizontal rows of small black dots, as shown in Fig. 3, occurred every mask vertical period but these did not lead to any noticeable degradation of the displayed image. This is consistent with the fact that the mask vertical period of 0.018-inch is considerably smaller than the mask horizontal period of 0.030-inch, and even the latter gave only a small visual perturbation to the display.

Fig. 5—Transmitted video picture on demountable demonstration tube.

The angular dependence of mask focusing could possibly have given rise to a circular pattern of best-focused spots. Such a pattern was avoided by our using a mask focus voltage that gave a spot width that decreased monotonically from the center to the corners of the phosphor screen. Moiré effects, caused by beating between the scanning beam diameter and the focus mask vertical period, were observed. These effects were minimized by the selection of beam diameters that were appropriate for the mask vertical period, as is now done for shadow masks. Picture quality was judged to be insensitive to $\pm 10\%$ variations in the mask focus voltage.

5. Conclusions

The performance of a dipole-quadrupole focus mask has been demonstrated in a functioning color picture tube. The tube is an experimental type and many problems need to be solved before such a focus mask tube can be commercially manufactured. The mask insulator used here will not withstand the thermal processing of conventional tube preparation. More suitable insulators might be, for example, glass or polyimide which have both thermal stability and high breakdown voltages. Furthermore, the 10-inch demonstration tube employed a flat focus mask and a flat screen; this avoided the problems associated with forming the mask to a spherical or cylindrical shape and the problems of preparing a compatible phosphor screen. Although mask forming presents no conceptual difficulties, screen preparation will require methods other than the conventional lighthousing.

The dipole-quadrupole focus mask has been shown to provide a highly transmitting color-selection structure requiring only moderate voltage biases and possessing good structural integrity. These masks have transmissions on the order of 50% compared to the 18–22% of typical shadow masks. The bias voltage necessary to achieve color purity extrapolates linearly to about 625 volts for a 25kV color tube. The presence of the horizontal webs of the aperture plates provides a sturdiness not present in the older focus masks using only long vertical wires, and this sturdiness allows the present construction to be extendible to any size tube.

Acknowledgments

The authors appreciate the many contributions from colleagues whose assistance was important during this focus mask investigation. The phosphor screen was prepared by V. Christiano and G. A.

McMahon. The demountable tube was by C. C. Steinmetz. C.A. Catanese greatly contributed to the technical activity and gave administrative support. Acknowledgment is also made of the roles of R. D. Lohman, P. N. Yocom, and L. S. Cosentino in guiding the activity.

References:

[1] E. F. Hockings, S. Bloom, and C. A. Catanese, "A Focus Mask for Color Picture Tubes using Dipolar and Quadrupolar Lensing," *IEEE Trans. El. Dev.* **ED-30,** p. 912 (1983).
[2] R. Dressler, "The P.D.F. Chromatron—A Single or Multi-Gun Cathode Ray Tube," *Proc. I.R.E.*, **41,** 851 (1953).
[3] E. G. Ramberg, H. B. Law, H. S. Allwine, D. C. Darling, C. W. Henderson, and H. Rosenthal, "Focusing Grill Color Kinescopes," *I.R.E. Convention Record*, **4,** Part 3, p. 128 (1956).
[4] M. van Alphen and J. van den Berg, "Quadrupole Post-Focusing Shadowmask CRT," *Soc. Info. Display Int. Symp. Digest,* p. 46 (1980).
[5] J. van Esdonk, "Method of Manufacturing a Color Display Tube and Color Display Tube Manufactured by Said Method," U.S. Patent 4,164,059 (1979).
[6] D. J. Tamutus, "Method of Fabricating a Color-selection Structure for a CRT," U.S. Patent 4,341,591 (1982).
[7] J. van Esdonk, "Color Selection Lens Electrodes Connected by Diffusion Bonds," U.S. Patent 4,066,923 (1978).
[8] K. J. van Oostrum, "Color Display Tube and Method of Manufacturing such a Color Display Tube," U.S. Patent 4,188,562 (1980).
[9] H. J. Ronde, "Color Selection Means Comprising Lens Electrodes Spaced by Grains of Insulating Materials," U.S. Patent 4,107,569 (1978).
[10] J. van Esdonk and P. F. A. Haans, "Color Television Display Tube and Method of Manufacturing Same," U.S. Patent 4,121,131 (1978).
[11] J. Koorneef and A. J. der Kinderen, "Color Selection Means for Color Display Tube and Method of Making Same," U.S. Patent 4,197,482 (1980).
[12] W. M. van Alphen and J. Verweel, "Shadow Mask Each Aperture of Which is Defined by A Quadrupolar Lens," U.S. Patent 4,059,781 (1977).
[13] H. J. Ronde and P. C. van Loosdregt, "Method of Manufacturing a Cathode Ray Tube for Displaying Colored Pictures," U.S. Patent 4,160,311 (1979).
[14] J. Koorneef, "Process for Manufacturing a Color Picture Tube, Color Picture Tube Manufactured by this Process and Device for Carrying out the Process," German Patent 2,700,135 (1977).
[15] R. F. L. M. van der Ven, "Color Picture Tube," German Patent 2,814,391 (1978).
[16] S. Takenaka, E. Hamano, and E. Kamohara, "Mask-focusing Color Picture Tube," European Patent Application 58992 (1982).
[17] J. Verweel, "Magnetic Post-focusing in Shadowmasks for Color Picture Tubes," *Soc. Info. Display Int. Symp. Digest*, p. 48 (1980).
[18] J. Verweel, "Shadow Mask having Magnetic Quadrupoles Around Each Mask Aperture," U.S. Patent 4,135,111 (1979).
[19] J. Verweel, "Magnetic Focusing for CTV Tube Masks," *Soc. Info. Display Int. Symp. Digest,* p. 54 (1982).

A General Scattering Theory

John Howard*
RCA Astro Electronics, Princeton, NJ 08540

Abstract—A fundamentally different approach to the problems of electromagnetic wave propagation through a medium containing a distribution of scatterers is presented. The new theory includes the effects of scatterers in the near field of the transmitting and/or receiving antennas, a factor that currently accepted theories do not include. Near-field effects are important especially in the case of satellite microwave communications where the near field of the large ground antennas includes an appreciable fraction or even the whole of the rain path. The theory is based on the Lorentz form of Reciprocity Theorem and may be used to estimate attenuation and depolarization of microwaves through precipitation.

1. Introduction

Current interest in microwave propagation studies through precipitation particles has been prompted by proposals for terrestrial and satellite communication systems operating above 10 GHz.[1,2] At these frequencies the presence of precipitation particles in the transmission medium causes attenuation and depolarization of the transmitted radiation.[3,4] Both effects may represent a severe limitation on system performance, and in particular, the depolarization effect is of considerable importance to the possible use of two orthogonal polarizations as separate communication channels in future satellite and terrestrial communication systems.[5]

A theoretical approach to the problem of microwave attenuation due to various meteorological phenomena was first given by Ryde[6] in 1946. In his paper Ryde computed the attenuation and the intensity of the radar echoes produced by fog, cloud, rain, hail, and

* Presently with The Narda Microwave Corp., Hauppauge, NY 11788.

snow on the basis of electromagnetic theory for wavelengths in the centimeter band. He showed that the principal cause of microwave attenuation is rain. Ryde assumed spherical drops throughout his work and, therefore, depolarization effects due to departure of raindrop shape from sphericity were not reported.

Van de Hulst[7] treated a similar problem of wave propagation in a medium containing independent particles that scatter and absorb the incident energy. The effect of the particles on the transmitted wave is expressed in terms of an effective complex index of refraction. Van de Hulst's approach is very useful in that it predicts both the attenuation and phase shift introduced by the particles. Both are important in estimating rain-induced depolarization of the transmitted radiation.

In 1965 Medhurst[8] repeated and extended Ryde's work on rain. He made a systematic comparison between theoretically predicted rainfall attenuation levels and those found by experiment. He concluded that the agreement was not completely satisfactory, and that there was a marked tendency for observed attenuations to occur well above levels which according to the theoretical predictions could not be exceeded. Medhurst gave two possible reasons for this. The first reason was the neglect in the theory of multiple scattering effects along the path. Ryde had assumed that the interaction between drops was negligible when the distance between the drops was greater than five times their diameter, as normally will be the case. The second possible source of error in the theory was that the rain structure was more complex than had been assumed, in that the precipitation may tend to contain clusters of two or more closely spaced drops.

Mink[9], using a controlled experiment, showed however that for no variations in the rainfall rate and drop-size composition along the transmission path, there still existed a large discrepancy between theory and measurements.

This observation was also taken up by Crane,[10] who suggested that Van de Hulst's theory was incomplete in that it did not include the effects that rain has on microwave radiation when in the near field of an antenna. Crane modified the existing theory by including antenna pattern correction factors for the near field. He further supported his theoretical modifications with experimental evidence. He concluded that rain in the near field of large antenna systems may cause different values of attenuation than predicted on the basis of Van de Hulst's theory. His results also showed measurable polarization effects both for phase and amplitude.

In 1978 Haworth et al[11] expressed doubt as to the correctness of

Crane's conclusions. They suggested that the antenna correction factors of Crane resulted from the neglect of the near-field effects on the boresight amplitudes and especially phases of the antenna responses, and that when proper account is taken of these effects the antenna correction factors will disappear. They commented on the importance of conclusively clarifying the effects of rain in the near field of an antenna especially for microwave satellite communications.

Knowledge of whether rain in the near field of an antenna has different effects on microwave propagation than in the far field is of extreme importance. Although in terrestrial microwave communications the near field of both antennas might be only a small portion of the total path of the link, in satellite microwave communications the near field of the large ground-station antenna could include an appreciable fraction or even the whole of the rain path.

In this paper, we investigate the scattering effects that rain, or any other scatterer, in the near field of one or both antennas has on a microwave communication link. From this investigation a new theoretical approach to the problem of electromagnetic wave propagation through a medium containing a distribution of scatterers has been developed. The new theory includes this effect of the near field regions of the two antennas; it is found that their contribution is negligible.

2. Analysis

The analysis is given in four sections. Sec. 2.1 deals with propagation in the absence of precipitation and an expression for the received wave is derived. In Sec. 2.2, a raindrop is introduced and the received wave due to its scattered radiation is deduced. Sec. 2.3 considers the received wave due to a uniform distribution of similar sized raindrops contained within an elemental volume. Sec. 2.4 extends the analysis to obtain expressions for the attenuation and phase shift due to a thick precipitation layer.

2.1 E. M. Wave Propagation in the Absence of Precipitation

Consider the situation of two aperture antennas directed towards each other as shown in Fig. 1. Let $\mathbf{E}_1,\mathbf{H}_1$ be the field of the transmitter (antenna 1) and $\mathbf{E}_2,\mathbf{H}_2$ be the field of the receiver (antenna 2) when it acts as a transmitter.

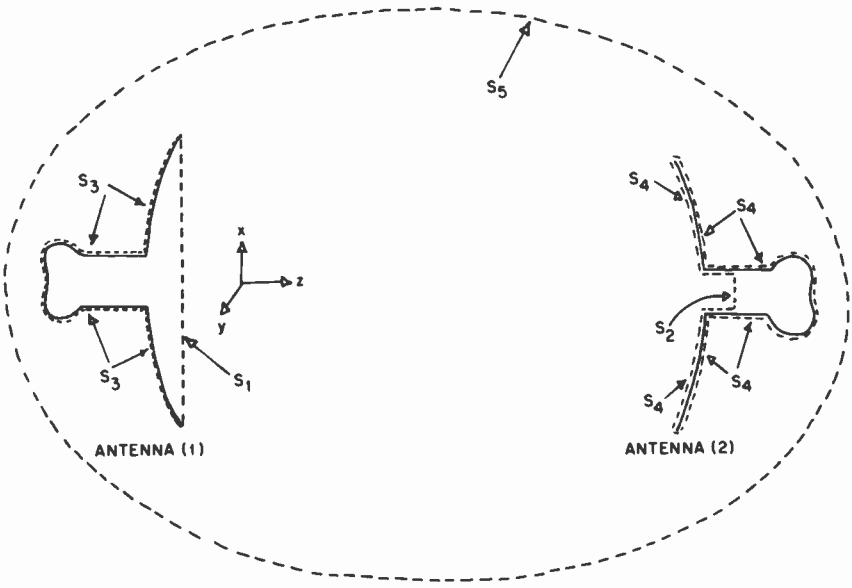

Fig. 1—Propagation in the absence of precipitation.

Consider the volume V, bounded by the surface S_1, S_2, S_3, S_4, and S_5. Within this volume there are no impressed currents and both fields ($\mathbf{E}_1$,$\mathbf{H}_1$ and $\mathbf{E}_2$,$\mathbf{H}_2$) satisfy Maxwell's equations in free space i.e.,

$$\begin{aligned}
\nabla \times \mathbf{E}_1 &= -jw\,\mu_0\,\mathbf{H}_1 \\
\nabla \times \mathbf{H}_1 &= \quad jw\,\epsilon_0\,\mathbf{E}_1 \\
\nabla \times \mathbf{E}_2 &= -jw\,\mu_0\,\mathbf{H}_2 \\
\nabla \times \mathbf{H}_2 &= \quad jw\,\epsilon_0\,\mathbf{E}_2
\end{aligned} \qquad [1]$$

Also

$$\begin{aligned}
\nabla \cdot (\mathbf{E}_1 \times \mathbf{H}_2 - \mathbf{E}_2 \times \mathbf{H}_1) = {} & \mathbf{H}_2 \cdot \nabla \times \mathbf{E}_1 - \mathbf{E}_1 \cdot \nabla \times \mathbf{H}_2 \\
& - \mathbf{H}_1 \cdot \nabla \times \mathbf{E}_2 + \mathbf{E}_2 \cdot \nabla \times \mathbf{H}_1
\end{aligned} \qquad [2]$$

Using Eq. [2] in Eqs. [1], we obtain

$$\begin{aligned}
\nabla \cdot (\mathbf{E}_1 \times \mathbf{H}_2 - \mathbf{E}_2 \times \mathbf{H}_1) &= -jw\,\mu_0\,\mathbf{H}_1 \cdot \mathbf{H}_2 - jw\,\epsilon_0\,\mathbf{E}_1 \cdot \mathbf{E}_2 \\
&\quad + jw\,\mu_0\,\mathbf{H}_1 \cdot \mathbf{H}_2 + jw\,\epsilon_0\,\mathbf{E}_1 \cdot \mathbf{E}_2 \\
&= 0.
\end{aligned}$$

Hence, using Gauss' theorem, we have

$$\iint_{S_1+S_2+\ldots S_5} (\mathbf{E}_1 \times \mathbf{H}_2 - \mathbf{E}_2 \times \mathbf{H}_1) \cdot \hat{\mathbf{n}} dS = 0, \qquad [3]$$

where $\hat{\mathbf{n}}$ is taken as the outward normal on the respective surfaces. Equation [3] is in fact the Lorentz form of Reciprocity Theorem for free space.

Consider now each surface in turn.

(a) Surface S_1

The surface S_1 is taken as the aperture plane of antenna 1. Assuming large antennas, compared to the wavelength, and assuming matched polarizations, the fields over this surface can be written as,

$$\mathbf{E}_1 = \hat{\mathbf{i}}\, E_1$$
$$\mathbf{H}_1 = \hat{\mathbf{j}} \sqrt{\epsilon_0/\mu_0}\, E_1$$
$$\mathbf{E}_2 = \hat{\mathbf{i}}\, E_2$$
$$\mathbf{H}_2 = -\hat{\mathbf{j}} \sqrt{\epsilon_0/\mu_0}\, E_2.$$

Also, for this surface, $\hat{\mathbf{n}} = -\hat{\mathbf{k}}$. Hence

$$\iint_{S_1} (\mathbf{E}_1 \times \mathbf{H}_2 - \mathbf{E}_2 \times \mathbf{H}_1) \cdot \hat{\mathbf{n}} dS = 2\sqrt{\epsilon_0/\mu_0} \iint_{S_1} \mathbf{E}_1 E_2\, dS. \qquad [4]$$

(b) Surface S_2

This surface is located in the transmission line connected to antenna 2. It is assumed, for simplicity of analysis, that the line is matched and only the normal transmission line mode exists. Hence, on surface S_2 we have,

$$\mathbf{E}_1 = \hat{\mathbf{u}}\, B_i\, f(x,y)$$
$$\mathbf{H}_1 = (\hat{\mathbf{k}} \times \hat{\mathbf{u}}) \frac{B_i}{Z_0} f(x,y)$$
$$\mathbf{E}_2 = \hat{\mathbf{u}}\, A\, f(x,y)$$
$$\mathbf{H}_2 = -(\hat{\mathbf{k}} \times \hat{\mathbf{u}}) \frac{A}{Z_0} f(x,y) \qquad [5]$$

where B_i is the complex amplitude of inward travelling wave due to antenna 1 transmitting, A is the complex amplitude of outward travelling wave due to antenna 2 transmitting, Z_0 the wave impedance of the transmission line, $\hat{\mathbf{u}}$ a unit vector normal to $\hat{\mathbf{k}}$, $f(x,y)$ the distribution function of the transmission line mode.

Also, $\hat{\mathbf{n}} = \hat{\mathbf{k}}$. Then

$$(\mathbf{E}_1 \times \mathbf{H}_2 - \mathbf{E}_2 \times \mathbf{H}_1)\cdot\hat{\mathbf{n}} = -2\frac{A\,B_i}{Z_0} f^2(x,y)\,[\hat{\mathbf{u}} \times (\hat{\mathbf{k}} \times \hat{\mathbf{u}})]\cdot\hat{\mathbf{k}}$$
$$= -2\frac{A\,B_i}{Z_0} f^2(x,y)\,[(\hat{\mathbf{k}} \times \hat{\mathbf{u}})\cdot(\hat{\mathbf{k}} \times \hat{\mathbf{u}})]$$
$$= -2\frac{A\,B_i}{Z_0} f^2(x,y).$$

Hence

$$\iint_{S_2} (\mathbf{E}_1 \times \mathbf{H}_2 - \mathbf{E}_2 \times \mathbf{H}_1)\cdot\hat{\mathbf{n}}\,dS = -2\,\frac{A\,B_i}{Z_0}\iint_{S_2} f^2(x,y)\,dx\,dy. \quad [6]$$

(c) Surfaces S_3 and S_4

The integral over these surfaces vanishes. To show this, we note that $\mathbf{E}_1$ and $\mathbf{E}_2$ are parallel with the normal $\hat{\mathbf{n}}$ everywhere over S_3 and S_4 which are assumed to be perfectly conducting surfaces. Hence we can write $\mathbf{E}_1 = \hat{\mathbf{n}}E_1$ and $\mathbf{E}_2 = \hat{\mathbf{n}}E_2$ over these surfaces. Thus

$$(\mathbf{E}_1 \times \mathbf{H}_2 - \mathbf{E}_2 \times \mathbf{H}_1)\cdot\hat{\mathbf{n}} = [E_1\,(\hat{\mathbf{n}} \times \mathbf{H}_2)\cdot\hat{\mathbf{n}} - E_2\,(\hat{\mathbf{n}} \times \mathbf{H}_1)\cdot\hat{\mathbf{n}}]$$
$$= [E_1\,(\hat{\mathbf{n}} \times \hat{\mathbf{n}})\cdot\mathbf{H}_2 - E_2\,(\hat{\mathbf{n}} \times \hat{\mathbf{n}})\cdot\mathbf{H}_1]$$
$$= 0.$$

Therefore

$$\iint_{S_3+S_4} (\mathbf{E}_1 \times \mathbf{H}_2 - \mathbf{E}_2 \times \mathbf{H}_1)\cdot\hat{\mathbf{n}}\,dS = 0. \quad [7]$$

(d) Surface S_5

Surface S_5 is taken to be a large sphere tending to infinity. Hence on this surface we have

$$\mathbf{E}_1 = -\hat{\mathbf{n}} \times \mathbf{H}_1\sqrt{\mu_0/\epsilon_0}$$
$$\mathbf{E}_2 = -\hat{\mathbf{n}} \times \mathbf{H}_2\sqrt{\mu_0/\epsilon_0}$$

and

$$(\mathbf{E}_1 \times \mathbf{H}_2 - \mathbf{E}_2 \times \mathbf{H}_1)\cdot\hat{\mathbf{n}} = -\sqrt{\mu_0/\epsilon_0}\,[(\hat{\mathbf{n}} \times \mathbf{H}_1) \times \mathbf{H}_2]\cdot\hat{\mathbf{n}}$$
$$+\sqrt{\mu_0/\epsilon_0}\,[(\hat{\mathbf{n}} \times \mathbf{H}_2) \times \mathbf{H}_1]\cdot\hat{\mathbf{n}}$$
$$= \sqrt{\mu_0/\epsilon_0}\,[\hat{\mathbf{n}}\,(\mathbf{H}_2\cdot\mathbf{H}_1) - \mathbf{H}_1\,(\mathbf{H}_2\cdot\hat{\mathbf{n}})]\cdot\hat{\mathbf{n}}$$
$$-\sqrt{\mu_0/\epsilon_0}\,[\hat{\mathbf{n}}\,(\mathbf{H}_1\cdot\mathbf{H}_2) - \mathbf{H}_2\,(\mathbf{H}_1\cdot\hat{\mathbf{n}})]\cdot\hat{\mathbf{n}}$$
$$= 0.$$

Therefore

$$\iint_{S_5} (\mathbf{E}_1 \times \mathbf{H}_2 - \mathbf{E}_2 \times \mathbf{H}_1) \cdot \hat{\mathbf{n}} dS = 0. \quad [8]$$

Finally, using Eqs. [4], [6], [7], and [8], we have

$$2\sqrt{\epsilon_0/\mu_0} \iint_{S_1} E_1 E_2 \, dS - 2 \frac{A B_i}{Z_0} \iint_{S_2} f^2(x,y) \, dS = 0,$$

i.e.,

$$B_i = \frac{Z_0}{A} \sqrt{\epsilon_0/\mu_0} \left(\iint_{S_1} E_1 E_2 \, dS \left[\iint_{S_1} f^2(x,y) \, dS \right]^{-1} \right). \quad [9]$$

2.2 E. M. Wave Propagation In the Presence of a Single Particle

Consider the arrangement shown in Fig. 2. It is similar to Fig. 1 except that an arbitrarily shaped raindrop (or any scatterer) is now introduced.

Let $\mathbf{E}_3,\mathbf{H}_3$ be the field due to the transmitter (antenna 1) in the presence of precipitation and $\mathbf{E}_2,\mathbf{H}_2$ be the field of the receiver (antenna 2) when it acts as a transmitter in free space. (N.B., $\mathbf{E}_2,\mathbf{H}_2$ here are the same as defined in Sec. 2.1; however, $\mathbf{E}_3,\mathbf{H}_3$ are not the same as $\mathbf{E}_1,\mathbf{H}_1$ defined in the same section. This will become clear in Sec. 2.4.) Let $\mathbf{E}_{S_1},\mathbf{H}_{S_1}$ be the scattered field in free space due to $\mathbf{E}_3,\mathbf{H}_3$ incident on the raindrop. Both $\mathbf{E}_{S_1},\mathbf{H}_{S_1}$ and $\mathbf{E}_2,\mathbf{H}_2$ satisfy Maxwell's free-space equations in the volume V bounded by the surfaces S_2, S_3 . . . S_7. Hence, following the initial analysis in Sec. 2.1, we have

$$\iint_{S_2+S_3+\ldots S_7} (\mathbf{E}_{S_1} \times \mathbf{H}_2 - \mathbf{E}_2 \times \mathbf{H}_{S_1}) \cdot \hat{\mathbf{n}} dS = 0 \quad [10]$$

where $\hat{\mathbf{n}}$ is the outward normal on the respective surfaces.

Consider now the various surface integrals.

(a) Surfaces S_3, S_4, and S_5

By a similar analysis to that given in Sec. 2.1,

$$\iint_{S_3+S_4+S_5} (\mathbf{E}_{S_1} \times \mathbf{H}_2 - \mathbf{E}_2 \times \mathbf{H}_{S_1}) \cdot \hat{\mathbf{n}} dS = 0. \quad [11]$$

(b) Surface S_2

Also following Sec. 2.1, it can be shown that

$$\iint_{S_2} (\mathbf{E}_{S_1} \times \mathbf{H}_2 - \mathbf{E}_2 \times \mathbf{H}_{S_1}) \cdot \hat{\mathbf{n}} dS = -2 \frac{A B_s}{Z_0} \iint_{S_2} f^2(x,y)\, dS, \quad [12]$$

where A, Z_0 and $f(x,y)$ are the same as defined previously in Sec. 2.1 and B_s is the complex amplitude of the inward travelling wave at S_2 due to the scattered field $\mathbf{E}_{S_1}$,$\mathbf{H}_{S_1}$ which itself is due to $\mathbf{E}_3$,$\mathbf{H}_3$.

(c) Surface S_7

Both $\mathbf{E}_{S_1}$,$\mathbf{H}_{S_1}$, and $\mathbf{E}_2$,$\mathbf{H}_2$ give rise to travelling waves in the same direction across S_7. This fact may be used to show

$$\iint_{S_7} (\mathbf{E}_{S_1} \times \mathbf{H}_2 - \mathbf{E}_2 \times \mathbf{H}_{S_1}) \cdot \hat{\mathbf{n}} dS = 0. \quad [13]$$

(d) Surface S_6

This surface is taken to be that of the raindrop. Consider a point 0 anywhere in the scatterer as shown in Fig. 2. At this point, the fields $\mathbf{E}_3$,$\mathbf{H}_3$ and $\mathbf{E}_2$,$\mathbf{H}_2$ can be written as

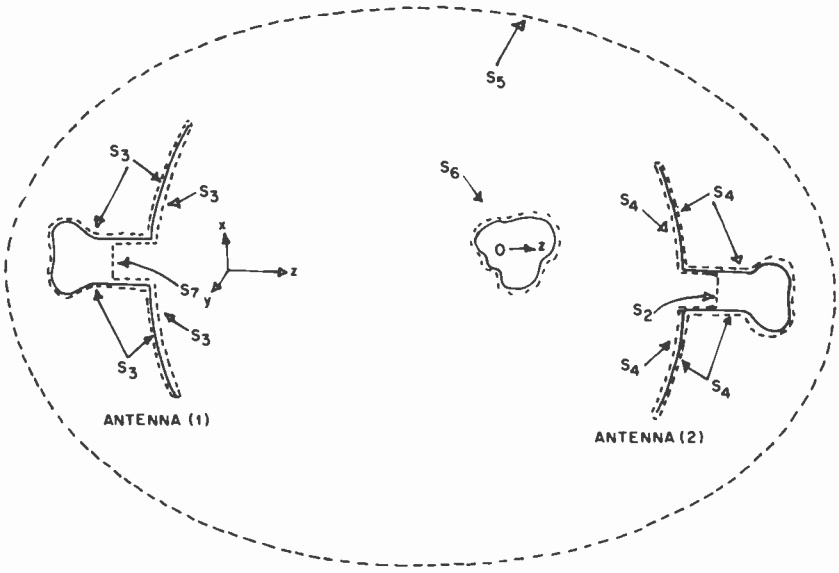

Fig. 2—Propagation in the presence of a single scatterer.

$$\mathbf{E}_3 = \hat{\mathbf{i}}\, E_{30}$$
$$\mathbf{H}_3 = \hat{\mathbf{j}}\, E_{30}\sqrt{\epsilon_0/\mu_0}$$
$$\mathbf{E}_2 = \hat{\mathbf{i}}\, E_{20}$$
$$\mathbf{H}_2 - \hat{\mathbf{j}}\, E_{20}\sqrt{\epsilon_0/\mu_0} \qquad [14]$$

where E_{30} is the complex amplitude of $\mathbf{E}_3$ at 0 and E_{20} is the complex amplitude of $\mathbf{E}_2$ at 0.

Eq. [14] assumes that both $\mathbf{E}_3$ and $\mathbf{E}_2$ are linearly polarized in the same direction. This is justifiable within the narrow common volume illuminated by the two antennas.

Now, over the region occupied by the raindrop, we can express $\mathbf{E}_3$,$\mathbf{H}_3$ and $\mathbf{E}_2$,$\mathbf{H}_2$ as approximately plane waves travelling in opposite directions. Thus, taking the point 0 as the origin of the z' axis (see Fig. 2),

$$\mathbf{E}_3 = \hat{\mathbf{i}}\, E_{30} \exp\{-j\, k\, z'\}$$
$$\mathbf{H}_3 = \mathbf{j}\, E_{30}\sqrt{\epsilon_0/\mu_0} \exp\{-j\, k\, z'\}$$
$$\mathbf{E}_2 = \hat{\mathbf{i}}\, E_{20} \exp\{j\, k\, z'\}$$
$$\mathbf{H}_2 = -\hat{\mathbf{j}}\, E_{20}\sqrt{\epsilon_0/\mu_0} \exp\{j\, k\, z'\} \qquad [15]$$

From the above, it can be seen that

$$\mathbf{E}_2 = \left(\frac{E_{20}}{E_{30}^*}\right)\mathbf{E}_3^*$$
$$\mathbf{H}_2 = \left(\frac{E_{20}}{E_{30}^*}\right)\mathbf{H}_3^* \qquad [16]$$

where * denotes the complex conjugate. Using Eq. [16], we have

$$\iint_{S_6} (\mathbf{E}_{S_1} \times \mathbf{H}_2 - \mathbf{E}_2 \times \mathbf{H}_{S_1}) \cdot \hat{\mathbf{n}}\, dS = -\left(\frac{E_{20}}{E_{30}^*}\right) \iint_{S_6} (\mathbf{E}_3^* \times \mathbf{H}_{S_1} + \mathbf{E}_{S_1} \times \mathbf{H}_3^*) \cdot \mathrm{n}\, dS. \qquad [17]$$

It is now recalled that the scattered field $\mathbf{E}_{S_1}$,$\mathbf{H}_{S_1}$ is in fact due to $\mathbf{E}_3$,$\mathbf{H}_3$ incident on the raindrop. The integral on the right hand side of Eq. [17] can be shown[12] to be related to the forward scattering complex vector amplitude $\mathbf{F}(0)$ of a scatterer by the following (see Appendix 2):

$$\iint_{S_6} (\mathbf{E}_3^* \times \mathbf{H}_{S_1} + \mathbf{E}_{S_1} \times \mathbf{H}_3^*) \cdot \hat{\mathbf{n}}\, dS = -\frac{4\pi}{jk}\sqrt{\epsilon_0/\mu_0}\,(\mathbf{E}_{30}^* \cdot \mathbf{F}(0)). \qquad [18]$$

For any scatterer, we have*

$$\mathbf{F}(0) = \hat{\mathbf{i}}\, E_{30}\, \frac{S(0)}{jk} \qquad [19]$$

where $S(0)$ is the forward scattering complex scalar amplitude of a scatterer as defined by Van de Hulst (see Appendix 1).

Using Eqs. [17], [18], and [19] and remembering that $\mathbf{E}^*_{30} = \hat{\mathbf{i}}\, E^*_{30}$, we obtain,

$$\iint_{S_6} (\mathbf{E}_{S_1} \times \mathbf{H}_2 - \mathbf{E}_2 \times \mathbf{H}_{S_1}) \cdot \hat{\mathbf{n}} dS = -\frac{4\pi}{k^2} \sqrt{\epsilon_0/\mu_0}\, E_{30}\, E_{20}\, S(0). \qquad [20]$$

Finally, using Eqs. [11], [12], [13], and [20] in Eq. [10], we have

$$-2\, \frac{A\, B_s}{Z_0} \iint_{S_2} f^2(x,y)\, dS - \frac{4\pi}{k^2} \sqrt{\epsilon_0/\mu_0}\, E_{30}\, E_{20}\, S(0) = 0,$$

i.e.,

$$B_s = -2\, \frac{\pi\, Z_0}{A\, k^2} \sqrt{\epsilon_0/\mu_0} \left(\frac{E_{30}\, E_{20}\, S(0)}{\iint_{S_2} f^2(x,y)\, dS} \right). \qquad [21]$$

2.3 E. M. Wave Propagation In the Presence of Scatterers In An Elemental Volume

From Eq. [15] it is noted that in the region occupied by the raindrop,

$$\mathbf{E}_3 = \hat{\mathbf{i}}\, E_3 = \hat{\mathbf{i}}\, E_{30} \exp\{-j\, k\, z'\}$$
$$\mathbf{E}_2 = \hat{\mathbf{i}}\, E_2 = \hat{\mathbf{i}}\, E_{20} \exp\{j\, k\, z'\} \qquad [22]$$

where E_3 and E_2 are the complex scalar amplitudes of $\mathbf{E}_3$ and $\mathbf{E}_2$, respectively. Hence, over this region,

$$E_{30}\, E_{20} = E_3\, E_2. \qquad [23]$$

The above equation shows that the product E_3E_2 can be assumed constant over the region occupied by the raindrop. In fact it can be assumed that E_3E_2 is constant over an elemental volume dv in space. The wave picked up by the receiving antenna from any rain-

* F(0) and S(0) are dependent on the scatterer shape

drop located within this volume is thus obtained by using Eqs. [23] and [21] as,

$$B_s = -2\,\frac{\pi\,Z_0}{A\,k^2}\sqrt{\epsilon_0/\mu_0}\left(\frac{E_3E_2\,S(0)}{\iint_{S_2} f^2(x,y)\,dS}\right). \qquad [24]$$

If the elemental volume dv contains similar sized raindrops uniformly distributed in dv and if N is the number of raindrops per unit volume, then by applying Single Scattering theory it follows from Eq. [24] that the wave picked up by the receiving antenna due to scattered radiation from the raindrops in dv is given by

$$B_S^{dv} = -2\,\frac{\pi\,Z_0}{A\,k^2}\sqrt{\epsilon_0/\mu_0}\left(\frac{E_3E_2\,N\,S(0)}{\iint_{S_2} f^2(x,y)\,dS}\right)dv \qquad [25]$$

2.4 E. M. Wave Propagation in the Presence of a Distribution of Scattering

The analysis is now extended to include a precipitation region containing many raindrops. Consider the arrangement shown in Fig. 3. Let the precipitation be contained between the planes $z = z_1$ and $z = z_2$. Further, let the elemental volume dv be located at plane z.

It is recalled that in Eq. [25], E_3 is taken to be the complex scalar amplitude of $\mathbf{E}_3$ in the elemental volume dv. Further, $\mathbf{E}_3,\mathbf{H}_3$ was tacitly assumed in Sec. 2.2 to be the field due to the transmitting antenna (i.e., antenna 1) in the presence of precipitation. In fact it is this field which induces the scattered field $\mathbf{E}_{S_1},\mathbf{H}_{S_1}$ of each raindrop.

Now, when no precipitation is present, $\mathbf{E}_3,\mathbf{H}_3$ is identical to the field $\mathbf{E}_1,\mathbf{H}_1$ in Sec. 2.1. When precipitation is present, $\mathbf{E}_3$ and $\mathbf{E}_1$ are related via the effective complex refractive index $\tilde{m}$ of the precipitation region (see Appendix 1) as,

$$\mathbf{E}_3 = \mathbf{E}_1 \exp\{-jk\,(\tilde{m} - 1)\,(z - z_1), \qquad [26]$$

where, $z_1 \leq z \leq z_2$. With reference to Fig. 3, Eq. [26] gives the transmitter field (i.e., the field due to antenna 1 in the presence of precipitation) in the elemental volume dv. Hence, using Eq. [25], we obtain the wave picked up by the receiving antenna due to scattering by raindrops in dv,

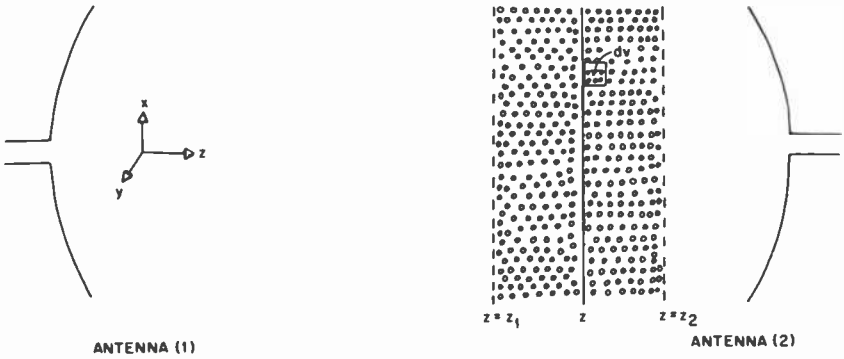

Fig. 3—A distribution of scatterers.

$$B_S^{dv} = -2 \frac{\pi Z_0}{A k^2} \sqrt{\epsilon_0/\mu_0} \left(\frac{E_1 E_2 N S(0) \exp\{-jk(\bar{m} - 1)(z - z_1)\}}{\iint_{S_2} f^2(x,y)\, dS} \right) \quad [27]$$

where E_1 and E_2 are taken as the complex scalar amplitudes of the field vectors $\mathbf{E}_1$ and $\mathbf{E}_2$, respectively, in dv.

Assuming single scattering and that a sufficient number of drops are present in the elemental volume, the wave picked up by the receiving antenna, due to scattering from all the raindrops in the precipitation region, is obtained by integrating Eq. [27], i.e.,

$$\Sigma B_S^{dv} = -2 \frac{\pi Z_0}{A k^2} \sqrt{\epsilon_0/\mu_0} \left(\frac{\iiint_{vol} E_1 E_2 N S(0) \exp\{-jk(\bar{m} - 1)(z - z_1)\}}{\iint_{S_2} f^2(x,y)\, dS} dv \right) \quad [28]$$

where vol indicates integration over the precipitation volume, i.e., the region between $z = z_1$ and $z = z_2$.

Now, the beamwidth of the two antennas, transmitter and receiver, is very small. Therefore, the volume integral in Eq. [28] may be written

$$\int_{z_1}^{z_2} \left[\int_{-\infty}^{\infty} \int_{-\infty}^{\infty} E_1 E_2 \, dx \, dy \right] N S(0) \exp\{-jk(\bar{m} - 1)(z - z_1)\} \, dz \quad [29]$$

and Eq. [28] becomes

$$\Sigma B_S^{dv} = -2\frac{\pi Z_0}{A k^2}\sqrt{\epsilon_0/\mu_0}\int_{z_1}^{z_2}\left(\left[\int_{-\infty}^{\infty}\int_{-\infty}^{\infty} E_1 E_2\, dx\, dy\right] N S(0)\right.$$
$$\left.\exp\{-jk(\tilde{m}-1)(z-z_1)\}\left[\iint_{S_2} f^2(x,y)\, dS\right]^{-1} dz\right) \qquad [30]$$

At this stage it is useful to draw attention to two important equations. In Sec. 2.1 it was shown that the received wave in the absence of precipitation is given by

$$B_i = \frac{Z_0}{A}\sqrt{\epsilon_0/\mu_0}\left(\frac{\iint_{S_1} E_1 E_2\, dS}{\iint_{S_2} f^2(x,y)\, dS}\right). \qquad [9]$$

The other important result is Eq. [30]. This gives the received wave due to scattering from all the raindrops in the precipitation region. The total wave received in the presence of precipitation is

$$B_T = B_i + \Sigma B_S^{dv}$$
$$= B_i\left[1 + \Sigma\frac{B_S^{dv}}{B_i}\right]. \qquad [31]$$

Now, from Eqs. [9] and [30], we obtain

$$\Sigma\frac{B_S^{dv}}{B_i} = -2\frac{\pi}{k^2}\int_{z_1}^{z_2}\left[\int_{-\infty}^{\infty}\int_{-\infty}^{\infty} E_1 E_2\, dx\, dy\right] N S(0)$$
$$\exp\{-jk(\tilde{m}-1)(z-z_1)\}\left[\iint_{S_2} E_1 E_2\, dS\right]^{-1} dz \qquad [32]$$

Using this in Eq. [31], we have

$$B_T = B_i\left[1 - \frac{2\pi}{k^2}\int_{z_1}^{z_2}\left[\int_{-\infty}^{\infty}\int_{-\infty}^{\infty} E_1 E_2\, dx\, dy\right] N S(0)\right.$$
$$\left.\exp\{-jk(\tilde{m}-1)(z-z_1)\}\left[\iint_{S_2} E_1 E_2\, dS\right]^{-1} dz\right] \qquad [33]$$

If we define α and β as the total attenuation in Nepers and phase shift in radians, respectively, due to the precipitation, then

$$B_T = B_i \exp\{-(\alpha + j\beta)\}. \qquad [34]$$

Hence, comparing Eqs. [33] and [34], we obtain

$$\exp\{-(\alpha + j\beta)\} = 1 - \frac{2\pi}{k^2}\int_{z_1}^{z_2}\left[\int_{-\infty}^{\infty}\int_{-\infty}^{\infty} E_1 E_2\, dx\, dy\right] N S(0) \exp\{-jk(\tilde{m}-1)(z-z_1)\}\left[\iint_{S_1} E_1 E_2\, dS\right]^{-1} dz \quad [35]$$

Now, $\tilde{m}$ and S(0) are related by Eq. [A7] (see Appendix 1). Using Eq. [A7] in Eq. [35] gives

$$\exp\{-(\alpha + j\beta)\} = 1 - \int_{z_1}^{z_2}\left[\int_{-\infty}^{\infty}\int_{-\infty}^{\infty} E_1 E_2\, dx\, dy\right] jk(\tilde{m}-1) \exp\{-jk(\tilde{m}-1)(z-z_1)\}\left[\iint_{S_1} E_1 E_2\, dS\right]^{-1} dz \quad [36]$$

In naturally occurring rain, the raindrops will have a drop size distribution, and $\tilde{m}$ will be given by,

$$\tilde{m} = 1 - j\frac{2\pi}{k^3}\sum_a N(a)\, S(0)_a \quad [37]$$

where a is the mean drop radius. If the rate of precipitation is uniform throughout, $\tilde{m}$ will be independent of z and Eq. [36] becomes,

$$\exp\{-(\alpha + j\beta)\} = 1 - jk(\tilde{m}-1)\exp\{jk(\tilde{m}-1)z_1\} \int_{z_1}^{z_2}\left[\int_{-\infty}^{\infty}\int_{-\infty}^{\infty} E_1 E_2\, dx\, dy\right]\exp\{-jk(\tilde{m}-1)z\}\left[\iint_{S_1} E_1 E_2\, dS\right]^{-1} dz \quad [38]$$

The integral $\iint_{S2} E_1 E_2\, dS$ predicts the receiving power at antenna 1 due to antenna 2 transmitting (see Fig. 1). The integral $\int_{-\infty}^{\infty}\int_{-\infty}^{\infty} E_1 E_2\, dS$ can be written as $\iint_A E_1 E_2\, dS$, where A is the beamwidth cross section of the common volume of propagation of the two antennas. Then

$$\iint_A E_1 E_2\, dS = \iint_{S_1} E_1 E_2\, dS.$$

Therefore

$$\int_{-\infty}^{\infty}\int_{-\infty}^{\infty} E_1 E_2 \, dS = \iint_{S_1} E_1 E_2 \, dS \qquad [39]$$

for any plane z normal to the direction of propagation. Using Eq. [39] in Eq. [38] we obtain

$$\exp\{-(\alpha + j\beta)\} = 1 - jk(\bar{m} - 1) \int_{z_1}^{z_2} \exp\{-jk(\bar{m} - 1)(z - z_1)\} \, dz$$

$$= \exp\{-jk(\bar{m} - 1)(z_2 - z_1)$$

and

$$\alpha + j\beta = j\,k\,(\bar{m} - 1)(z_2 - z_1). \qquad [40]$$

Hence

$$\alpha = \text{Re}\,[j\,k\,(\bar{m} - 1)(z_2 - z_1)] \text{ Nepers}$$

$$= 8.686\,k\,(z_2 - z_1)\,\text{Im}\,(1 - \bar{m}) \text{ dB} \qquad [41]$$

$$\beta = \text{Im}\,[j\,k\,(\bar{m} - 1)(z_2 - z_1) \text{ Radians}$$

$$= k\,(z_2 - z_1)\,\text{Re}\,(\bar{m} - 1). \text{ Radians} \qquad [42]$$

Eqs. [41] and [42] are the same as Eqs. [A9] and [A10] in Appendix 1 for the case where the scatterers are in the far field of both transmitting and receiving antennas. Thus, whether rain is in the far field or the near field of each antenna, the result is the same total attenuation and total phase shift.

3. Conclusion

In this paper a new theoretical approach to the problem of electromagnetic wave propagation through a medium containing a distribution of scatterers was presented. The new theory includes the effects of scatterers in the near-field regions of the transmitting and receiving antennas, a factor that the currently accepted theory of Van de Hulst[7] does not include. Near-field effects are important especially in the case of satellite microwave communications where the near field of the large ground station antenna includes an appreciable fraction or even the whole of the rain path.

The conclusion from the analysis presented is that scatterers, such as rain in a normal precipitation environment, whether in the near or the far field of the transmitting and receiving antennas, will introduce the same attenuation and phase shift, and therefore the same depolarization.

From the foregoing, it is evident that R. K. Crane's[10] conclusion that the near fields of the antennas must be included in the calculation of the attenuation and phase-shift effects due to precipitation, when such near fields are an appreciable part of the rain path (i.e., in a satellite link), could be in error.

Appendix 1—Wave Propagation in a Medium Containing Scatterers

Let a fixed particle of arbitrary shape and composition be illuminated by a plane scalar wave. The origin of coordinates is chosen somewhere in the particle. The disturbance of the incident wave can be expressed by

$$u_0 = \exp\{-j\,k\,z\} \qquad [A1]$$

The scattered spherical wave in the forward direction in the distant field is then given by,

$$u = \frac{S(0)}{j\,k\,r}\exp\{-j\,k\,r\} \qquad [A2]$$

where r is the distance from the particle to the point of observation and $S(0)$ the forward scattering scalar complex amplitude of a single scatterer. Combining Eqs. [A1] and [A2], we have

$$u = \frac{S(0)}{j\,k\,r}\exp\{-j\,k\,r + j\,k\,z\}\,u_0 \qquad [A3]$$

If the point of observation is (x,y,z), then if x and y are much smaller than z, we obtain

$$r = z + \frac{x^2 + y^2}{2z}$$

Adding the amplitudes of u_0 and u of the incident and scattered waves we obtain,

$$u_0 + u = u_0\,[1 + (S(0)/j\,k\,z)\exp\{-jk\,([x^2 + y^2]/2z)\} \qquad [A4]$$

In the case of a medium containing many scatterers, which are all identical and identically orientated, only particles in the 'active' volume, i.e., the volume of propagation between the transmitting and receiving antenna, which coincides with the few central Freznel zones as seen from the observation point, will influence the forward travelling wave. The total applitude at the observation point is then given by

$$u = u_0 \left[1 + S(0) \sum_N \frac{1}{j\,k\,z} \exp \left\{ -jk \left(\frac{x^2 + y^2}{2z} \right) \right\} \right]$$

where the summation Σ_N is extended over all the particles in the 'active' volume. If these particles are numerous, the summation sign may be replaced by

$\int N\,dx\,dy\,dz.$

Direct integration gives

$$u = u_0 \left[1 - \frac{2\pi}{k^2} N\,l\,S(0) \right], \qquad \text{[A5]}$$

where l is the length of precipitation in the z-direction. The result may formally be represented as the influence of a complex refractive index of the medium containing scatterers as a whole. If we assume a complex refractive index $\tilde{m}$ for the medium, then, the amplitude of the wave is changed by the medium in the proportion,

$$\exp \{-j\,k\,l\,(\tilde{m} - 1)\} = 1 - j\,k\,l\,(\tilde{m} - 1). \qquad \text{[A6]}$$

Also, from Eqs. [A5] and [A6] we obtain

$$\tilde{m} = 1 - j\frac{2\pi}{k^3} N\,S(0). \qquad \text{[A7]}$$

From Eq. [A6], we have

$$\exp \{-(\alpha + j\beta)\} = \exp \{-j\,k\,l\,(\tilde{m} - 1)\}, \qquad \text{[A8]}$$

where α is the total attenuation in nepers and β is the total phase shift in radians. From Eq. [A8] we obtain

$$\alpha = \text{Re}\,[j\,k\,(\tilde{m} - 1)\,l] \text{ Nepers}$$
$$= 8.686\,k\,l\,\text{Im}\,(1 - \tilde{m}) \text{ dB} \qquad \text{[A9]}$$

$$\beta = \text{Im}\,[j\,k\,(\tilde{m} - 1)\,l]$$
$$= k\,l\,\text{Re}\,(\tilde{m} - 1) \text{ Radians} \qquad \text{[A10]}$$

Eqs. [A9] and [A10] are the same as Eqs. [41] and [42] in Sec. 2.4.

Appendix 2—The Forward Scattering Complex Vector Amplitude

Consider

$$\iint_S (\mathbf{E}_i^* \times \mathbf{H}_S + \mathbf{E}_S \times \mathbf{H}_i^*) \cdot \hat{\mathbf{u}}_n\,dS \qquad \text{[A11]}$$

where $\hat{\mathbf{u}}_n$ is the outward normal on the surface S. This is Eq. [21] in Sec. 2.2 where

$$E_i = \mathbf{A} \exp\{-jk\,\mathbf{u}\cdot\mathbf{r}\}$$

$$H_i = \sqrt{\epsilon_0/\mu_0}\,(\mathbf{u}\times\mathbf{A}) \exp\{-jk\,\mathbf{u}\cdot\mathbf{r}\}. \qquad \text{[A12]}$$

where $\mathbf{u}$ is the unit vector in the direction of observation. Using Eq. [A12] in [A11], we obtain

$$\iint_S (\mathbf{E}_i^*\times\mathbf{H}_S + \mathbf{E}_S\times\mathbf{H}_i^*)\cdot\hat{\mathbf{u}}_n\,dS = \iint_S (\mathbf{A}^*\times\mathbf{H}_S)\cdot\hat{\mathbf{u}}_n \exp\{-jk\,\mathbf{u}\cdot\mathbf{r}\}\,dS + \sqrt{\epsilon_0/\mu_0}\iint_S [\mathbf{E}_S\times(\mathbf{u}\times\mathbf{A})]\cdot\hat{\mathbf{u}}_n \exp\{-jk\,\mathbf{u}\cdot\mathbf{r}\}\,dS. \qquad \text{[A13]}$$

Now

$$\begin{aligned}(\mathbf{A}^*\times\mathbf{H}_S)\cdot\hat{\mathbf{u}}_n &= \hat{\mathbf{u}}_n\cdot[\mathbf{A}^*\times\mathbf{H}_S]\\ &= \mathbf{A}^*\cdot[\mathbf{H}_S+\hat{\mathbf{u}}_n]\\ &= -\mathbf{A}^*\cdot(\hat{\mathbf{u}}_n\times\mathbf{H}_S)\end{aligned} \qquad \text{[A14]}$$

and

$$\begin{aligned}[\mathbf{E}_S\times(\mathbf{u}\times\mathbf{A}^*)]\cdot\hat{\mathbf{u}}_n &= \hat{\mathbf{u}}_n\cdot[\mathbf{E}_S\times(\mathbf{u}\times\mathbf{A}^*)]\\ &= (\mathbf{u}\times\mathbf{A}^*)\cdot(\hat{\mathbf{u}}_n\times\mathbf{E}_S)\\ &= (\hat{\mathbf{u}}_n\times\mathbf{E}_S)\cdot(\mathbf{u}\times\mathbf{A}^*)\\ &= \mathbf{A}^*\cdot[(\hat{\mathbf{u}}_n\times\mathbf{E}_S)\times\mathbf{u}]\\ &= -\mathbf{A}^*\cdot[\mathbf{u}\times(\hat{\mathbf{u}}_n\times\mathbf{E}_S)]\end{aligned} \qquad \text{[A15]}$$

Using Eqs. [A14] and [A15] in Eq. [A13] and defining for convenience $e^K = e^{jk\mathbf{u}\cdot\mathbf{r}}$, we have

$$\begin{aligned}\iint_S (\mathbf{E}_i^*\times\mathbf{H}_S + \mathbf{E}_S\times\mathbf{H}_i^*)\cdot\hat{\mathbf{u}}_n\,dS &= -\mathbf{A}^*\cdot\iint_S (\hat{\mathbf{u}}_n\times\mathbf{H}_S)\,e^K\,dS\\ &\quad - \sqrt{\epsilon_0/\mu_0}\,\mathbf{A}^*\cdot\iint_S [\mathbf{u}\times\hat{\mathbf{u}}_n\times\mathbf{E}_S]\,e^K\,dS\\ &= -\mathbf{A}^*\cdot\iint_S (\hat{\mathbf{u}}_n\times\mathbf{H}_S)\,e^K\,dS - \sqrt{\epsilon_0/\mu_0}\\ &\quad \mathbf{A}^*\cdot\left[\,\mathbf{u}\times\iint_S (\hat{\mathbf{u}}_n\times\mathbf{E}_S)\,e^K\,dS\,\right]\\ &= \mathbf{A}^*\cdot\left[\,-\iint_S (\hat{\mathbf{u}}_n\times\mathbf{H}_S)\,e^K\,dS - \sqrt{\epsilon_0/\mu_0}\right.\end{aligned}$$

$$\mathbf{u} \times \iint_S (\hat{\mathbf{u}}_n \times \mathbf{E}_S)\, e^K\, dS \Bigg]. \qquad \text{[A16]}$$

From Eq. (8.105) of Ref. [12], we have for the forward scattering complex vector amplitude $\mathbf{F}_t(\mathbf{u})$

$$\begin{aligned}
\mathbf{F}_t(\mathbf{u}) &= \frac{jk}{4\pi}\left[\sqrt{\mu_0/\epsilon_0}\,\mathbf{u} \times \left[\mathbf{u} \times \iint_S (\hat{\mathbf{u}}_n \times \mathbf{H}_S)\, e^K\, dS\right]\right. \\
&\quad \left. - \mathbf{u} \times \iint_S (\hat{\mathbf{u}}_n \times \mathbf{E}_S)\, e^K\, dS\right] \\
&= \frac{jk}{4\pi}\sqrt{\mu_0/\epsilon_0}\left[\mathbf{u} \times \left[\mathbf{u} \times \iint_S (\hat{\mathbf{u}}_n \times \mathbf{H}_S)\, e^K\, dS\right]\right. \\
&\quad \left. - \sqrt{\epsilon_0/\mu_0}\,\mathbf{u} \times \iint_S (\hat{\mathbf{u}}_n \times \mathbf{E}_S)\, e^K\, dS\right] \\
&= \frac{jk}{4\pi}\sqrt{\epsilon_0/\mu_0}\left[\mathbf{u}\left[\mathbf{u} \cdot \iint_S (\hat{\mathbf{u}}_n \times \mathbf{H}_S)\, e^K\, dS\right]\right. \\
&\quad - (\mathbf{u} \cdot \mathbf{u}) \iint_S (\hat{\mathbf{u}}_n \times \mathbf{H}_S)\, e^K\, dS \\
&\quad \left. - \sqrt{\epsilon_0/\mu_0}\,\mathbf{u} \times \iint_S (\hat{\mathbf{u}}_n \times \mathbf{E}_S)\, e^K\, dS\right]. \qquad \text{[A17]}
\end{aligned}$$

Then

$$\begin{aligned}
\mathbf{A}^* \cdot \mathbf{F}_t(\mathbf{u}) &= \frac{jk}{4\pi}\sqrt{\mu_0/\epsilon_0}\left[\mathbf{A}^* \cdot \mathbf{u}\left[\mathbf{u} \cdot \iint_S (\hat{\mathbf{u}}_n \times \mathbf{H}_S)\, e^K\, dS\right]\right. \\
&\quad - \mathbf{A}^* \cdot \iint_S (\hat{\mathbf{u}}_n \times \mathbf{H}_S)\, e^K\, dS - \sqrt{\epsilon_0/\mu_0} \\
&\quad \left.\mathbf{A}^* \cdot \left[\mathbf{u} \times \iint_S (\hat{\mathbf{u}}_n \times \mathbf{E}_S)\, e^K\, dS\right]\right] \\
&= \frac{jk}{4\pi}\sqrt{\mu_0/\epsilon_0}\left[-\mathbf{A}^* \cdot \iint_S (\hat{\mathbf{u}}_n \times \mathbf{H}_S)\, e^K\, dS\right. \\
&\quad \left. - \sqrt{\epsilon_0/\mu_0}\, A^* \cdot \left[\mathbf{u} \times \iint_S (\hat{\mathbf{u}}_n \times \mathbf{E}_S)\, e^K\, dS\right]\right]
\end{aligned}$$

$$= \frac{jk}{4\pi}\sqrt{\mu_0/\epsilon_0}\,\mathbf{A}^* \cdot \left[-\iint_S (\hat{\mathbf{u}}_n \times \mathbf{H}_S)\, e^K\, dS \right.$$
$$\left. - \sqrt{\epsilon_0/\mu_0}\,\mathbf{u} \times \iint_S (\hat{\mathbf{u}}_n \times \mathbf{E}_S)\, e^K\, dS \right] \qquad [A18]$$

Using Eq. [A16] in Eq. [A18], we obtain

$$\mathbf{A}^* \cdot \mathbf{F}_t(\mathbf{u}) = \frac{jk}{4\pi}\sqrt{\mu_0/\epsilon_0} \left[\iint_S (\mathbf{E}_i^* \times \mathbf{H}_S + \mathbf{E}_S \times \mathbf{H}_i) \cdot \hat{\mathbf{u}}_n\, dS \right]$$

Thus

$$\iint_S (\mathbf{E}_i^* \times \mathbf{H}_S + \mathbf{E}_S \times \mathbf{H}_i^*) \cdot \hat{\mathbf{u}}_n\, dS = \frac{4\pi}{jk}\sqrt{\epsilon_0/\mu_0}\,[\mathbf{A}^* \cdot \mathbf{F}_t(\mathbf{u})] \qquad [A19]$$

If S is S_6, the surface of the scatterer in Sec. 2.2, then

$$\iint_{S_6} (\mathbf{E}_i^* \times \mathbf{H}_S + \mathbf{E}_S \times \mathbf{H}_i^*) \cdot \hat{\mathbf{n}}\, dS = -\iint_{S_6} (\mathbf{E}_i^* \times \mathbf{H}_S + \mathbf{E}_S \times \mathbf{H}_i^*) \cdot \hat{\mathbf{u}}_n\, dS$$

where $\hat{\mathbf{u}}_n = -\hat{\mathbf{n}}$. Therefore

$$\iint_{S_6} (\mathbf{E}_i^* \times \mathbf{H}_S + \mathbf{E}_S \times \mathbf{H}_i^*) \cdot \hat{\mathbf{n}}\, dS = -\frac{4\pi}{jk}\sqrt{\epsilon_0/\mu_0}\,[\mathbf{A}^* \cdot \mathbf{F}_t(\mathbf{u})] \qquad [A20]$$

References:

[1] B. J. Easterbrook and D. Turner, "Prediction of Attenuation by Rainfall in the 10.7–11.7 GHz Communication Band," *Proc. IEEE*, **114**, p. 557 (1967).
[2] L. C. Tillotson, "A Model of a Domestic Satellite Communication System," *Bell Syst. Tech. J.*, **47**, p. 2111 (1968).
[3] D. C. Hogg and T. S. Chu, "The Role of Rain in Satellite Communications," *Proc. IEEE*, **63**(9), p. 1308 (1975).
[4] D. C. Hogg and T. S. Chu, "Propagation of Radio Waves at Frequencies Above 10 GHz," *IEE Conf. Publ.* 98, (1973).
[5] W. E. Lothaller, "System Considerations for European Communication Satellites," *IEEE Int'l. Conf. on Communication*, Philadelphia, Pa., pp. 2-1 to 2-7 (1972).
[6] J. W. Ryde, "Attenuation of Centimetre Waves by Rain, Hail, and Clouds," Rept. 8516, General Electric Co. Research Labs., Wembley, England, (1944).
[7] H. C. Van de Hulst, *Light-Scattering by Small Particles*, New York: J. Wiley, p. 28 (1957).
[8] R. G. Medhurst, "Rainfall Attenuation of Centimeter Waves: Comparison of Theory and Measurement," *IEEE Trans. Antennas Propagation*, **AP 13**, p. 550 (1965).
[9] J. W. Mink, "Rain-Attenuation Measurements of Millimeter Waves Over Short Paths," *Electron. Lett.*, **9**(10), p. 198 (1973).
[10] R. K. Crane, "The Rain Range Experiment—Propagation Through a Simulated Rain Environment," *IEEE Trans. Antennas Propagation*, **AP 22**, p. 321, (1974).
[11] D. P. Haworth, N. J. McEwan, and P. A. Watson, "Effect of Rain in the Near Field of an Antenna," *Electron. Lett.*, **14**(4), p. 94, (1978).
[12] J. Van Bladel, *Electromagnetic Fields*, New York: McGraw-Hill, p. 254 (1964).

An Analytic Method for Calculating the Magnetic Field Due to a Deflection Yoke

Basab B. Dasgupta
RCA Consumer Electronics, 600 N. Sherman Drive,
Indianapolis, IN 46201

Abstract—An analytical method is developed for calculating the magnetic field produced by a magnetic deflection yoke. The method can be applied to get quantitatively correct results for an air-cored saddle coil or a toroidal coil wound on a magnetic core and qualitative results for a saddle coil in the presence of a core. The final result appears in the form of angular Fourier expansions of the field components about the yoke axis where each Fourier component is expressed as a simple one-dimensional integral of known functions. As an example of application of our formalism, the magnetic field functions $H_0(z)$ and $H_2(z)$ are calculated for a specific yoke and compared with their values computed by a completely numerical scheme. The agreement between the two sets of values is very satisfactory.

1. Introduction

Calculation of the magnetic field produced by a magnetic deflection yoke used in color televisions is a formidable problem, mainly because of the peculiar geometry of the yoke. All analytical calculations that can be found in the literature[1–6] have been confined to treating the fields at points on or near the yoke axis and/or restricted to yokes of very simple unrealistic geometries. Recently, a number of very sophisticated computer programs have been developed that compute the field numerically at any point inside the television tube.[7–9] These programs, although very accurate, are expensive to run and do not shed much light on the physical aspect of the problem. In this paper we report an analytical and accurate

method for calculating the magnetic field at an arbitrary point in space due to a saddle-shaped pair of coils *without* a magnetic core. The result appears in the form of Fourier expansions of each component of the magnetic field in a polar angle about the z-axis, and each Fourier component is in the form of an integral of a closed-form expression over z, the z axis being the yoke axis. With some modifications the result can be qualitatively applied to a saddle-wound coil and quantitatively applied to a toroidal coil in the presence of a magnetic core. This result would be very useful in understanding the dependence of the various field components on location of the field point, the geometry of the coil and its wire distribution. It would also save computer time in computing various quantities of interest to yoke designers that depend on the magnetic field components.

The paper is organized as follows. The calculation of magnetic field due to a saddle-shaped coil is divided into two parts: (a) calculation of field due to the main body of the yoke, which is assumed to be a current sheet with a certain surface current density distribution (determined by the actual angular distribution of the wires in the coil), and (b) calculation of field due to the end-turns, which are assumed to be circular arcs with a certain prescribed distribution along the z-direction. The first part is presented in Sec. 2 and the second part in Sec. 3. In Sec. 4 we discuss the modifications necessary to make our results applicable to a coil in the presence of a magnetic core. Sec. 5 is devoted to a numerical calculation of the magnetic field functions $H_0(z)$ and $H_2(z)$, which are of interest in the third-order aberration theory,[2,3] for a yoke under development at RCA on the basis of our theory. The same two functions are also calculated using an elaborate computer technique by following the methods described in Ref. [8], and the results are compared with our results. The agreement is very satisfactory. We conclude in Sec. 6 by suggesting some possible applications of our results.

2. Field Due to a Current Sheet of Revolution

We will use a cylindrical coordinate system (ρ, θ, z) in our derivation. We will assume the main deflecting part of the yoke to be a current sheet symmetric about the z-axis with a profile described by the function $\rho_0(z)$ (see Fig. 1). This profile is very similar to the profile of the neck of the cathode-ray tube and is usually expressed by a polynomial in z. The surface current density on the sheet $K(\rho_0, \theta, z)\mathbf{a}_K$ has a magnitude which can be expressed as a Fourier series

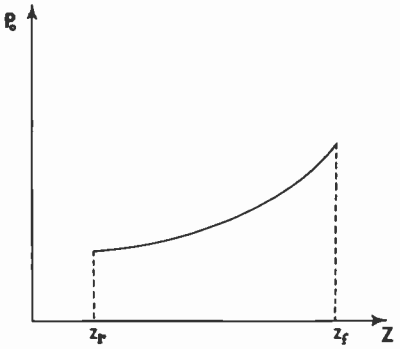

Fig. 1—The profile of the current sheet representing a saddle coil in the ρ-z plane.

$$K(\rho_0, \theta, z) \equiv \frac{I\lambda(\theta, z)}{\rho_0(z)} = \frac{I}{\rho_0(z)} \sum_{m = 1,3,5\ldots} f_m(z) \cos m\theta. \quad [1]$$

Here I is the current in each turn of the coil and $\lambda d\theta$ is the number of turns passing between the angles θ and $\theta + d\theta$ at a cross-section located at z. In writing Eq. [1] it is assumed that the x-axis lies along the horizontal direction if the coil is supposed to produce horizontal deflection and along the vertical direction if the coil is supposed to produce vertical deflection. The direction of the current density expressed by the unit vector $\boldsymbol{a}_K$ is *assumed* to be given by

$$\boldsymbol{a}_K = (\cos\theta\ \rho_0'\ \boldsymbol{a}_x + \sin\theta\ \rho_0'\ \boldsymbol{a}_y + \boldsymbol{a}_z)/(1 + \rho_0'^2)^{1/2}, \quad [2]$$

where $\boldsymbol{a}_x$, $\boldsymbol{a}_y$, $\boldsymbol{a}_z$ are unit vectors along x, y, z, axes and a prime indicates derivative with respect to z. Physically this means that the current flows along the profile of the coil-sheet in the (ρ, z) plane and along the radial lines in the (x, y) planes. Note, however, that this assumption does *not* imply that there is no bias in the coil, because λ in Eq. [1] is allowed to be z-dependent.

The magnetic field at an arbitrary point (ρ, θ, z) due to this current sheet can be obtained by applying the Biot-Savart law[10]

$$\boldsymbol{H}(\rho, \theta, z) = \int \frac{\boldsymbol{K}(\rho_0, \theta_0, z_0) \times \boldsymbol{R}\ ds}{4\pi R^3} \quad [3]$$

where ds is an element of surface area located at (ρ_0, θ_0, z_0) on the sheet and given by

$$ds = \rho_0(1 + \rho_0'(z_0)^2)^{1/2} d\theta_0 dz_0 \quad [4]$$

$$\boldsymbol{R} = (\rho\cos\theta - \rho_0\cos\theta_0)\boldsymbol{a}_x + (\rho\sin\theta - \rho_0\sin\theta_0)\boldsymbol{a}_y + (z - z_0)\boldsymbol{a}_z \quad [5]$$

$$R = \{\rho^2 + \rho_0^2 - 2\rho\rho_0\cos(\theta - \theta_0) + (z - z_0)^2\}^{1/2} \quad [6]$$

and the integration in Eq. [3] extends over the entire surface area of the sheet. After some straight-forward algebra it can be shown that the cylindrical components of $\boldsymbol{H}$ are given by

$$H_\rho(\rho, \theta, z) = \frac{1}{4\pi} \int dz_0 \int_0^{2\pi} d\theta_0 \, K(\rho_0, \theta_0, z_0) \frac{\rho_0 \sin(\theta_0 - \theta)}{R^3} [\rho_0'(z_0)(z - z_0) + \rho_0(z_0)], \quad [7]$$

$$H_\theta(\rho, \theta, z) = \frac{1}{4\pi} \int dz_0 \int_0^{2\pi} d\theta_0 \, K(\rho_0, \theta_0, z_0) \frac{\rho_0}{R^3} \times [-\cos(\theta_0 - \theta) \{\rho_0'(z_0)(z - z_0) + \rho_0(z_0)\} + \rho_0(z_0)], \quad [8]$$

$$H_z(\rho, \theta, z) = \frac{1}{4\pi} \int dz_0 \int_0^{2\pi} d\theta_0 \, K(\rho_0, \theta_0, z_0) \frac{\rho_0}{R^3} \rho_0'(z_0) \sin(\theta - \theta_0). \quad [9]$$

The z_0 integrals in Eqs. [7]–[9] extend from the rear-end to the front-end of the yoke.

Using the symmetry of the coil the magnetic field components can be expanded in the following way:

$$H_\rho(\rho, \theta, z) = \sum_n H_\rho^n(\rho, z) \sin n\theta \quad [10]$$

$$H_\theta(\rho, \theta, z) = \sum_n H_\theta^n(\rho, z) \cos n\theta \quad [11]$$

$$H_z(\rho, \theta, z) = \sum_n H_z^n(\rho, z) \sin n\theta. \quad [12]$$

The summations in Eqs. [10]–[12] and all sums over indices m and n in our subsequent discussion are implied to run over the odd positive integers. The nth harmonic component of H_ρ can be calculated using the usual Fourier formula

$$H_\rho^n(\rho, z) = \frac{1}{\pi} \int_0^{2\pi} H_\rho(\rho, \theta, z) \sin n\theta d\theta. \quad [13]$$

Substituting Eqs. [1] and [7] into Eq. [13] and changing the variable $(\theta_0 - \theta)$ to α we get

$$H_\rho^n(\rho, z) = \sum_m \frac{I}{4\pi^2} \int_0^{2\pi} d\theta \sin n\theta \int dz_0 f_m(z_0) [\rho_0'(z_0)(z - z_0) + \rho_0]$$

$$\times \int_{-\theta}^{2\pi-\theta} d\alpha \frac{\cos m(\alpha + \theta)\sin\alpha}{[\rho^2 + \rho_0^2 - 2\rho\rho_0\cos\alpha + (z - z_0)^2]^{3/2}} \quad [14]$$

If we now write

$$\cos m(\alpha + \theta)\sin n\theta = \tfrac{1}{2}[\sin\{(n + m)\theta + m\alpha\} - \sin\{(n - m)\theta - m\alpha\}] \quad [15]$$

and integrate partially with respect to θ, it is easy to show that only the term with $m = n$ survives in the summation appearing in Eq. [14] and gives

$$H_\rho^n(\rho, z) = -\frac{I}{4\pi}\int dz_0 f_n(z_0)[\rho_0'(z_0)(z - z_0) + \rho_0] \times \int_0^{2\pi} d\alpha \frac{\sin n\alpha \sin\alpha}{[\rho^2 + \rho_0^2 - 2\rho\rho_0\cos\alpha + (z - z_0)^2]^{3/2}}. \quad [16]$$

The integral over α can be performed by introducing the variable $\phi = \alpha/2$, expanding $\sin n\alpha$ as

$$\sin n\alpha \equiv \sin 2n\phi = \sum_{k=1}^{n} (-1)^{k+1} \binom{2n - k}{k - 1} 2^{2n-2k+1} \sin\phi \cos^{2n-2k+1}\phi \quad [17]$$

and integrating term by term.

The final result for H_ρ^n can be expressed as

$$H_\rho^n(\rho, z) = -\frac{I}{2\pi}\sum_{k=1}^{n} (-1)^{k+1} \binom{2n - k}{k - 1} 2^{2n-2k+1} B\left(\frac{3}{2}, \frac{2n - 2k + 3}{2}\right) \int dz_0 f_n(z_0)[\rho_0'(z_0)(z - z_0) + \rho_0(z_0)] \frac{1}{q^{3/2}} \times F\left(\frac{2n - 2k + 3}{2}, \frac{3}{2}; n - k + 3; \frac{4\rho\rho_0}{q}\right) \quad [18]$$

where

$$q = (\rho + \rho_0)^2 + (z - z_0)^2 \quad [19]$$

Here $F(a, b; c; x)$ is the hypergeometric function[11] and $B(x, y)$ is the beta function.[12]

Similar manipulations can be carried out to determine $H_\theta^n(\rho, z)$ and $H_z^n(\rho, z)$. For H_θ^n we get

$$H_\theta^n(\rho, z) = -\frac{I}{4\pi}\int dz_0 f_n(z_0)[\rho_0'(z_0)(z - z_0) + \rho_0(z_0)] \times \int_0^{2\pi} d\alpha \frac{\cos n\alpha \cos\alpha}{[\rho^2 + \rho_0^2 - 2\rho\rho_0\cos\alpha + (z - z_0)^2]^{3/2}} + \frac{I\rho}{4\pi}\int dz_0 f_n(z_0) \int_0^{2\pi} d\alpha \frac{\cos n\alpha}{[\rho^2 + \rho_0^2 - 2\rho\rho_0\cos\alpha + (z - z_0)^2]^{3/2}} \quad [20]$$

To do the α integrals we now need the following expansion

$$\cos n\alpha \equiv \cos 2n\phi = \sum_{k=1}^{n+1} (-1)^{k+1} \binom{2n}{2k-2} \cos^{2n-2k+2}\phi \sin^{2k-2}\phi \quad [21]$$

The final expression for H_θ^n is

$$H_\theta^n(\rho, z) = -\frac{I}{2\pi}\sum_{k=1}^{n+1}(-1)^{k+1}\binom{2n}{2k-2} B\left(\frac{2k-1}{2}, \frac{2n-2k+5}{2}\right) \times \int dz_0 f_n(z_0)[\rho_0'(z_0)(z - z_0) + \rho_0(z_0)]\frac{1}{q^{3/2}} F\left(\frac{2n-2k+5}{2}, \frac{3}{2}; n+3; \frac{4\rho\rho_0}{q}\right) + \frac{I}{4\pi}\sum_{k=1}^{n+1}(-1)^{k+1}\binom{2n}{2k-2} B\left(\frac{2k-1}{2}, \frac{2n-2k+3}{2}\right) \times \int dz_0 f_n(z_0)[\rho'(z_0)(z - z_0) + \rho_0(z_0) + \rho]\frac{1}{q^{3/2}} F\left(\frac{2n-2k+3}{2}, \frac{3}{2}; n+1; \frac{4\rho\rho_0}{q}\right). \quad [22]$$

Similarly, H_z^n can be written in the final form as

$$H_z^n(\rho, z) = \frac{\rho I}{4\pi}\sum_{k=1}^{n}(-1)^{k+1}\binom{2n-k}{k-1} 2^{2n-2k+1} B(1, n-k+1) \int dz_0 f_n(z_0)\rho_0'(z_0)\frac{1}{q^{3/2}} F\left(n-k+1, \frac{3}{2}; n-k+2; \frac{4\rho\rho_0}{q}\right). \quad [23]$$

Eqs. [18], [22], and [23] constitute the desired analytical expressions for the magnetic field due to the current sheet.

As a special case we note from Eqs. [16] and [20] that H_ρ^n and H_θ^n are zero on the yoke axis ($\rho = 0$) for all $n \neq 1$ and $H_z^n = 0$ at $\rho = 0$ for all n. The axial magnetic field $H_0(z)$ is equivalent to $H_\rho^1(\rho = 0, z)$ and is given from Eq. [18] by

$$H_0(z) = -\frac{I}{4} \int dz_0 f_1(z) \frac{[\rho_0'(z_0)(z - z_0) + \rho_0(z_0)]}{[\rho_0^2 + (z - z_0)^2]^{3/2}}. \quad [24]$$

3. Field Due to the End Turns

Let us first assume that both the front and rear end-turns can be approximated by certain single effective circular arcs about the z axis with certain mean radii and mean lengths but zero thicknesses. Fig. 2 shows the "effective" front end-turn defined in this way; the top half starts and ends at angles θ_f and $\pi - \theta_f$, respectively, has a radius a, and carries the current in the counter clockwise direction while the bottom half is just its "mirror image" about the x axis. If z_f is the location of the front end-turns and there are N turns in each half of the coil, the magnetic field dH at (ρ, θ, z) due to an element of length dL of this effective end-turn is again given by the Biot-Savart law:

$$dH = \frac{NI(dL \times R)}{4\pi R^3}, \quad [25]$$

where

$$dL = \pm a d\theta_0 a_\theta. \quad [26]$$

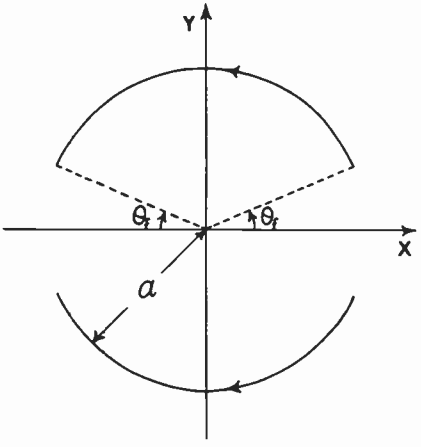

Fig. 2—The "effective" circular front end-turn of a saddle coil.

The upper and lower signs apply to the upper and lower halves of the turn, respectively, and R, R are given by Eqs. [5] and [6] respectively with ρ_0 replaced by a and z_0 replaced by z_f. To get the total field one has to integrate the expression [25] over θ_0 from θ_f to $\pi-\theta_f$ to take into account the upper half of the turn and then from $\pi + \theta_f$ to $2\pi-\theta_f$ to include the contribution of the lower half. After some simple algebra, the components of the field can be easily shown to be

$$H_\rho(\rho, \theta, z) = \frac{NIa(z - z_f)}{4\pi}\int_{\theta_f}^{\pi-\theta_f} \cos(\theta - \theta_0)\left[\frac{1}{R_-^3} + \frac{1}{R_+^3}\right]d\theta_0 \qquad [27]$$

$$H_\theta(\rho, \theta, z) = \frac{NIa(z - z_f)}{4\pi}\int_{\theta_f}^{\pi-\theta_f} \sin(\theta_0 - \theta)\left[\frac{1}{R_-^3} + \frac{1}{R_+^3}\right]d\theta_0 \qquad [28]$$

$$H_z(\rho, \theta, z) = \frac{NIa}{4\pi}\int_{\theta_f}^{\pi-\theta_f}\left[\frac{a - \rho\cos(\theta - \theta_0)}{R_-^3} - \frac{a + \rho\cos(\theta - \theta_0)}{R_+^3}\right]d\theta_0 \qquad [29]$$

where

$$R\pm = [\rho^2 + a^2 \pm 2\rho a\cos(\theta - \theta_0) + (z - z_f)^2]^{1/2}. \qquad [30]$$

All the integrals appearing in Eqs. [27]–[29] can be evaluated in closed-forms, but since we expressed the magnetic field due to the main body of the coil as Fourier series in θ we will do the same thing here and give explicit expressions for the Fourier coefficients. Thus using Eqs. [10] and [27], integrating by parts with respect to θ and after some manipulations, we get

$$H_\rho^n(\rho, z) = \frac{NIa(z - z_f)}{\pi n}\cos n\,\theta_f\int_0^\pi \frac{\cos n\alpha\,\cos\alpha\,d\alpha}{\{\rho^2 + a^2 - 2\rho a\cos\alpha + (z - z_f)^2\}^{3/2}}$$

or

$$H_\rho^n(\rho, z) = \frac{NIa(z - z_f)}{\pi n}\cos n\theta_f \sum_{k=1}^{n+1}(-1)^{k+1}\binom{2n}{2k-2}\frac{1}{q_f^{3/2}}$$
$$\times\left[2B\left(\frac{2k-1}{2}, \frac{2n-2k+5}{2}\right)F\left(\frac{2n-2k+5}{2}, \frac{3}{2}; n+3; \frac{4a\rho}{q_f}\right)\right.$$
$$\left. - B\left(\frac{2k-1}{2}, \frac{2n-2k+3}{2}\right)F\left(\frac{2n-2k+3}{2}, \frac{3}{2}; n+1; \frac{4a\rho}{q_f}\right)\right] \qquad [31]$$

where

$$q_f = (\rho + a)^2 + (z - z_f)^2 \qquad [32]$$

Similarly, using Eqs. [11], [12], [28], and [29] we get

$$H_\theta^n(\rho, z) = -\frac{NIa(z - z_f)}{\pi n} \cos n\theta_f \sum_{k=1}^{n} (-1)^{k+1} \binom{2n - k}{k - 1} 2^{2n-2k+1} \times \frac{1}{q_f^{3/2}} B\left(\frac{3}{2}, \frac{2n - 2k + 3}{2}\right) F\left(\frac{2n - 2k + 3}{2}, \frac{3}{2}, n - k + 3; \frac{4a\rho}{q_f}\right) \qquad [33]$$

and

$$H_z^n(\rho, z) = -\frac{\rho}{(z - z_f)} H_\rho^n(\rho, z) - \frac{NIa^2}{\pi n} \cos n\theta_f \sum_{k=1}^{n+1} (-1)^{k+1} \binom{2n}{2k - 2} \times \frac{1}{q_f^{3/2}} B\left(\frac{2k - 1}{2}, \frac{2n - 2k + 3}{2}\right) F\left(\frac{2n - 2k + 3}{2}, \frac{3}{2}; n + 1; \frac{4a\rho}{q_f}\right). \qquad [34]$$

Again in the special case of $\rho = 0$, Eq. [31] reduces to

$$H_\rho^1(0, z) \equiv H_0(z) = -\frac{NIa(z - z_f)\cos\theta_f}{2[a^2 + (z - z_f)^2]^{3/2}}, \qquad [35]$$

which agrees with the result given in Ref. [2].

Similarly if the rear end-turns are approximated by mean circular arcs of radii b, starting angle θ_r located at $z = z_r$, the Fourier coefficients of the magnetic field produced by them can be obtained from Eqs. [31], [33], and [34] by replacing a by b, the subscript f by r and changing the over-all signs to take into account the opposite direction of current.

Several generalizations of Eqs. [31], [33], and [34] are possible. First of all, we note that not all end-turns start at one angle. If we look at the front end-turns, for example, there are $\lambda(\theta_f, z_f)d\theta_f$ number of turns which start between the angles θ_f and $\theta_f + d\theta_f$, where the function λ is given by Eq. [1], i.e.,

$$\lambda(\theta_f, z_f) = \sum_m f_m(z_f)\cos m\theta_f. \qquad [36]$$

We can easily take into account this angular distribution of turns by writing $\lambda(\theta_f, z_f)d\theta_f$ for N in Eqs. [31], [33], and [34] and inte-

grating over θ_f from 0 to $\pi/2$. If the radius a of the turns were independent of θ_f the net result of this integration would have been replacing the quantity $N\cos n\theta_f$ in these expressions by $\pi f_n(z_f)/4$; but since a depends on θ_f each Fourier component of the magnetic field would involve all wire distribution harmonics $f_m(z_f)$. It is also true in reality that the end-turns do not lie in a single plane but have a certain thickness in the z-direction. This can be included in our theory by replacing $f_m(z_f)$ in Eq. [36] by some distribution of turns along z, $f_m(z_f)dz_f$ say, and integrating the resultant expressions for the field components over z_f. Again one has to keep in mind that the radius a would also be a function of z_f. The main difficulty in a practical computation is that the dependence of a on θ_f and z_f and the distribution of end-turns, $f_m(z_f)$, over their thickness are not very precisely known because they remain to a large extent at the mercy of the winding machine. If these functional relations can somehow be determined, the integrations over θ_f and/or z_f can be done numerically using a simple computer program. A similar comment applies to the rear end-turns as well. Another complexity of the end-turns, especially at the rear end, is that even though the turns might be circular arcs their centers may not lie on the z-axis. One can include this "off-centering" in the present treatment by an appropriate coordinate transformation. Finally, we want to point out that we need not restrict ourselves to circular end-turns; other unconventional shapes of end-turns such as rectangular and hexagonal[13] can also be taken into account in the present theory in a straightforward way.

4. Effect of the Core

The theoretical treatment given so far is valid if there is no magnetic core present in the yoke. When a core is present, it changes the magnetic field substantially. The relative permeability of the typical core material used in commercial yokes is quite high, of the order of 1000, and can be assumed to be infinity for all practical purposes. It can be shown[14] that for a long cylindrical yoke, the effect of such a high-permeability core is to multiply the n-th Fourier component of the magnetic field by the factor $[1 + (\rho_0/\rho_c)^{2n}]$, where ρ_0 and ρ_c are the coil and core radii, respectively; this result can be derived by solving the Laplace's equation for the z-component of the vector potential,

$$\nabla^2 A_z = 0 \qquad [37]$$

in the (ρ, θ) plane and using the usual boundary conditions at $\rho =$

ρ_0 and $\rho = \rho_c$. In view of this result, we can take into account the effect of the core in a qualitative way by introducing the following major simplication in our theory. We assume that the effect of a core on the magnetic field *inside* the yoke produced by the main body of the coil can be simulated by replacing the harmonic components $f_n(z)$ of the turn distribution by the functions

$$\tilde{f}_n(z) = [1 + \{\rho_0(z)/\rho_c(z)\}^{2n}]f_n(z) \qquad [38]$$

in Eqs. [18], [22], and [23]. Physically this means that each cross-section of the yoke is assumed to behave, as far as the effect of the core on the magnetic field is concerned, as if it were part of an infinitely long cylindrical yoke with that cross-section.

In the case of a toroid-shaped coil wound on the core, $\rho_0(z) = \rho_c(z)$ and Eq. [36] reduces to

$$\tilde{f}(z) = 2f_n(z). \qquad [39]$$

This result can be interpreted in terms of an "image" effect.[14] The image theorem states that if a *plane* surface of a magnetic material of infinite permeability is present in the vicinity of a current-carrying wire then the effect of the material on the magnetic field is the same as the one produced by a fictitious wire that is identical to the real wire but located on the other side of the plane surface at a distance equal to the distance of the wire from the surface. For a curved core surface the validity of this theorem, of course, becomes questionable, but if the actual coil sits right on the inner core surface, which is the case in a toroidal coil, the "image coil" coincides with the real coil both in strength and location regardless of the shape of the core surface. The magnetic field inside the yoke should then double compared to the core-free value. Eq. [39] is precisely equivalent to this statement. For a saddle coil, Eq. [38] can also be interpreted in terms of a contribution from an image coil, but in this case each harmonic component requires a different image.

It is more difficult to take into account the effect of the core on the magnetic field produced by the end-turns. The simplest approximation one can make is to assume that the contribution of the end-turns to the magnetic field is not affected by the presence of the core. At first glance this may seem like an unrealistic assumption, since a cylindrical core is known to have "shielding" effects on an external magnetic field. However, if we note that a core is typically only one inch or so in length, whereas the electron beams are deflected over a length of ten inches or more, and the field due to the end-turns is of secondary importance anyway, neglecting the shielding effect does not appear to be an overly crude assumption.

This is especially true for higher harmonics of the end-turn field which are localized near the turns.

For a toroidal coil, the effect of the core on the field produced by the end-turns is probably more drastic because of the proximity of the (radial) end-turns to the core surface, but since in this case the contributions of the end-turns to the field are quite small to begin with (because of the relatively small length of these turns compared to those of a saddle coil), we will simply ignore the end-turns altogether in calculating the field due to a toroidal coil.

5. Numerical Calculation

The numerical results calculated for a specific yoke using the expressions given in Sections 2–4 can be displayed graphically in a number of ways. One can plot each harmonic component of the magnetic fields H_ρ, H_θ, H_z or the total field as a function of ρ at a given z or as a function of z at a given ρ or along some curve in the ρ-z plane. As a first example of such numerical calculation, we have chosen to calculate and plot the magnetic field functions $H_0(z)$ ($\equiv H_y(0, 0, z)$) and $H_2(z)$ defined by

$$H_2(z) = \frac{1}{2}\left(\frac{\partial^2 H_y}{\partial x^2}\right)_{x=0,\, y=0}. \qquad [40]$$

These functions are of considerable interest in the third-order aberration theory,[2,3,15] and a knowledge of them allows one to calculate the aberration coefficients which determine the various deflection errors within the context of this theory. Another reason for choosing these quantities is that they can be experimentally measured with relative ease.

To perform a numerical calculation, one has to know the following quantities: the function $\rho_0(z)$, which represents the profile of the inner surface of the coil in the ρ-z plane; the function $\rho_c(z)$, which is the profile of the inner surface of the core; and the Fourier coefficients $f_n(z)$ of the winding distribution of the coil for each z. The first two functions are typically in the form of polynomials or a series of polynomials that join smoothly. The remaining functions can also be expressed as polynomials in z by fitting their numerical values by a polynomial-fitting routine. All the integrals involved in Eqs. [18], [22], and [23] are then simple one-dimensional integrals which can be done on a relatively small computer using a simple integration routine.

The $H_0(z)$ function due to the main body of the yoke and due to the end-turns of a saddle coil is given by Eqs. [24] and [35], respec-

tively, provided $f_1(z_0)$ in Eq. [24] is replaced by $\tilde{f}_1(z_0)$ defined by Eq. [38]. The $H_2(z)$ function can be calculated from H_ρ^1 and H_θ^3 functions according to a formula discussed in the appendix. The results are given below:

$H_2(z)$ (due to the main body of the yoke)

$$= \frac{I}{16}\int dz_0 \tilde{f}_1(z_0)\left[\frac{3(z-z_0)\rho'(z_0)+6\rho_0(z_0)}{\{\rho_0^2+(z-z_0)^2\}^{5/2}} - \frac{15}{2}\frac{\{\rho_0^2(z-z_0)\rho'(z_0)+\rho_0^3\}}{\{\rho_0^2+(z-z_0)^2\}^{7/2}}\right] - \frac{15I}{32}\int dz_0 \tilde{f}_3(z_0)\frac{\{\rho_0^2(z-z_0)\rho'(z_0)+\rho_0^3\}}{\{\rho_0^2+(z-z_0)^2\}^{7/2}}; \quad [41]$$

$H_2(z)$ (due to circular end turns of a saddle coil of mean radius a located at $z = z_f$ and lying between the angles θ_f and $\pi - \theta_f$ in the upper half and between $\pi + \theta_f$ and $2\pi - \theta_f$ in the lower half)

$$= \frac{NIa}{2\pi}(z-z_f)\left[\frac{5a^2\cos^3\theta_f}{\{a^2+(z-z_f)^2\}^{7/2}} - \frac{3a\cos\theta_f}{\{a^2+(z-z_f)^2\}^{5/2}}\right]. \quad [42]$$

In this paper we have calculated the variation of the quantities $H_0(z)$ and $H_2(z)$ with z for a yoke that is currently under development at RCA. The functions $\rho_0(z_0)$ and $\rho_c(z_0)$ have been computed using a program that determines the design of the arbor cavity used to make the horizontal coil and the design of the core. The functions $f_n(z)$ were determined by a program that Fourier analyzes the angular variation of the incremental area of the arbor cavity cross-section taking into account the fact that not the entire cavity is filled uniformly with wires during winding. The points z_f, z_r were taken in the middle of the coil thickness and the angles θ_f and θ_r were chosen to be approximately half-way between the starting and finishing angles at the front- and rear-ends, respectively. We have also calculated the $H_0(z)$ function for a toroidal coil radially wound on the core of this yoke neglecting the end-turns. Our results are shown in Figs. 3, 4, and 5.

To check the accuracy of these results we have also calculated $H_0(z)$ and $H_2(z)$ by using a very sophisticated and expensive computer program. The mathematical principles behind this program is discussed in Ref. [8]; it involves replacing the coil by an effective "magnetic charge" on the core which produces the same magnetic field everywhere inside the coil. The results of these calculations are also shown in Figs. 3, 4, and 5. The two sets of results are

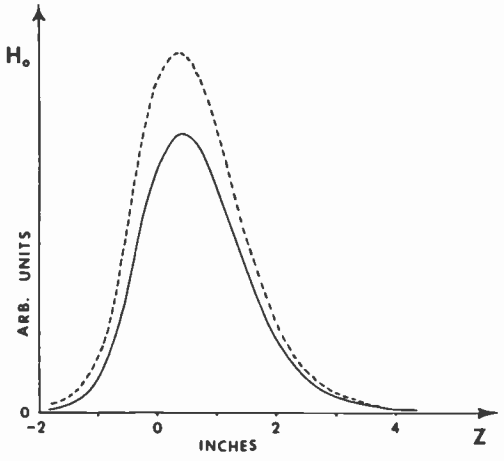

Fig. 3—The axial magnetic field $H_0(z)$ due to a nonradial saddle coil. The solid curve corresponds to the result derived in the present paper and the dashed curve corresponds to the values computed numerically by the method described Ref. [8].

strikingly similar. In particular, the general shapes of the curves and the locations of the maxima and minima are almost identical in the two cases. The two sets of curves even agree closely in absolute numbers. An exact agreement in magnitude for a saddle coil was not expected, partly because of the approximate nature of the way the core is taken into account in our theory and partly because the two theories treat the end-turns somewhat differently.

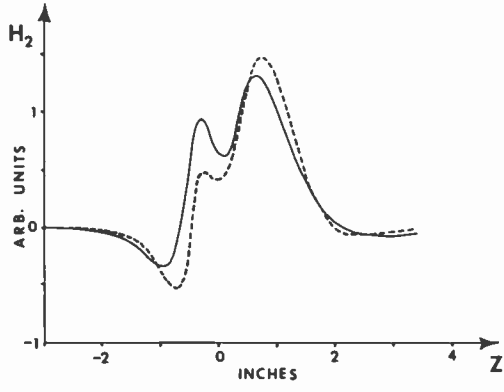

Fig. 4—The magnetic field function $H_2(z)$ due to a nonradial saddle coil. The solid curve corresponds to the result derived in the present paper and the dashed curve corresponds to the values computed numerically by the method described in Ref. [8].

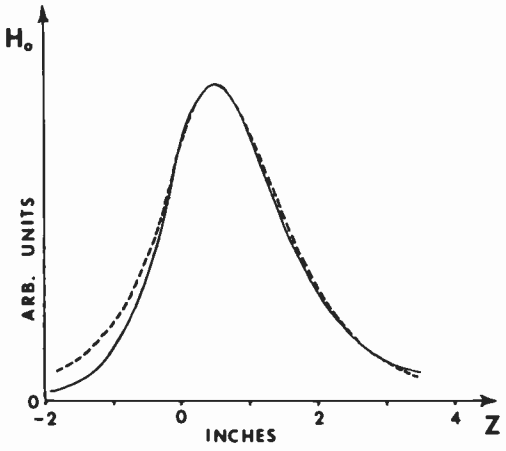

Fig. 5—The axial magnetic field $H_0(z)$ due to a radially wound toroidal coil. The solid curve corresponds to the result derived in the present paper and the dashed curve corresponds to the values computed numerically by the method described in Ref. [8].

In experiments done elsewhere[8,16] the computer-predicted variations of $H_0(z)$ and $H_2(z)$ were found to be in excellent agreement with experimental results for several yokes. Since our results agree very well with the computer calculations, this observation can also be considered as an indirect experimental verification of the present theory.

As a second example of numerical application of our theory we have calculated the various harmonic coefficients of the magnetic field components H_ρ and H_θ due to the end-turns of a saddle coil as a function of ρ using Eqs. [31] and [33] and neglecting the presence of the core. The results are shown in Figs. 6 and 7. Note that the contributions of all harmonics beyond the first are insignificant, but the first harmonic field is largely radial (i.e. pin-cushion shaped) close to the turns.

6. Concluding Remarks

We have developed an analytical method for calculating the magnetic field at an arbitrary point due to a magnetic deflection coil. The method is capable of giving quantitative results for an air-core saddle coil and qualitatively correct results in the presence of a magnetic core. The final numerical calculation of the field requires a simple numerical integration routine over one variable and a

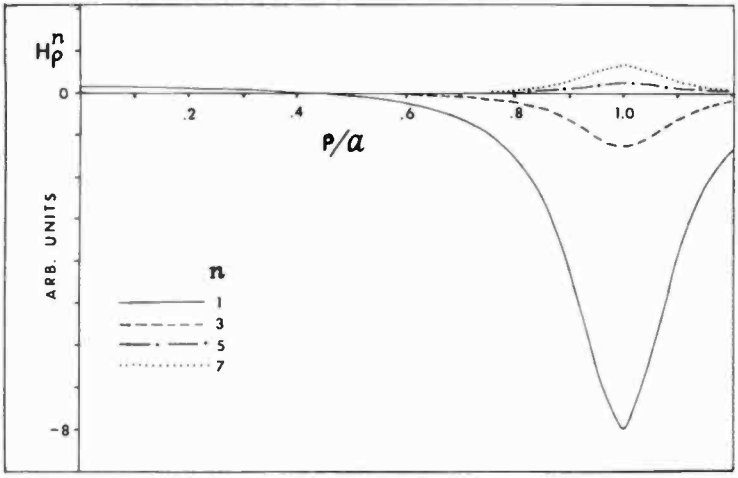

Fig. 6—The radial component of the magnetic field H_ρ as a function of ρ due to the circular end-turns of an air-core saddle coil at a distance 0.1α from the location of the end-turns. $\theta_f = 20°$.

function routine for evaluation of the hypergeometric series; both of these can be made readily available on a relatively small computer. Hence the success of the present method would imply considerable savings of computer CPU time over the numerical methods of computing the field, described in Refs. [7]–[9], and make it fea-

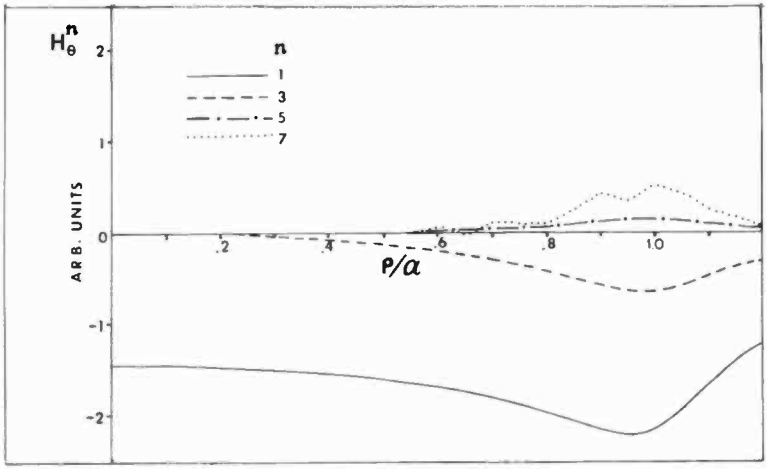

Fig. 7—The tangential component of the magnetic field H_θ as a function of ρ due to the circular end-turns of an air-core saddle coil at a distance $0.1a$ from the location of the end-turns. $\theta_f = 20°$.

sible to do these computations on a small computer. At present, for a saddle coil with a magnetic core, this success is limited because the effect of the core is not considered in a precise way, but we believe that an analytical treatment of the core could be improved, perhaps by some generalized image theorem. The present method can be easily extended to calculate the field due to the main body of a *toroidally* wound coil on a core simply by replacing $f_n(z_0)$ in Eqs. [18], [22], and [23] by $2f_n(z_0)$, the factor 2 being due to the image coil as discussed in Sec. 4. However, the core makes it difficult to calculate the field due to the end-turns of a toroidal coil.

A knowledge of the magnetic field at all points inside a television tube is extremely useful in analyzing the performance of a yoke and, in principle at least, it allows one to calculate all the characteristics relevant to its commercial use. We conclude by listing some important areas of application of our theory.

(1) Knowing the $H_0(z)$ and $H_2(z)$ functions for both coils, calculated in the previous section, one can calculate all the aberration coefficients appearing in the third-order aberration theory[2,3,15] and hence all the deflection errors produced by a yoke as predicted by this theory. Furthermore, one can determine higher-order derivatives of the field near the axis, such as the $H_4(z)$ function in the fifth-order aberration theory, from our expressions of field components.

(2) One can calculate the electron trajectories inside the tube once the magnetic field is known by solving the equations of motion of the electron. This would require a separate computer program similar to the one described in Ref. [9]. One could then determine the peak currents in both coils needed to scan the screen and other features relevant to manufacturing, such as the "pullback" distance.* The convergence errors on the screen can also be determined by first finding the coordinates of the landing points of the three primary beams and then taking the differences of various pairs of coordinates. This is not an accurate method of calculating the errors, however, since the errors are typically about 100 times smaller than the deflections of the beams and, hence, can be "washed out" by the inaccuracies in the computing method itself.

(3) Recently the author has developed a theory that relates the deflection errors directly with the harmonic components of the field.[17] The result involves integrations of expressions con-

* The pullback distance is the distance through which the yoke can be moved back starting from the tube neck before the electron beam strikes the inside glass of the tube.

taining the various field components along the trajectory of the electrons. An analytical expression for the Fourier components of the field would be extremely useful in a numerical computation of the deflection errors using this formalism.

(4) The inductance of a saddle-shaped horizontal coil can be expressed in terms of the variation of the harmonic components H_ρ^n and H_z^n along the inside coil contour.[18] Again analytical expressions for H_ρ^n and H_z^n would greatly facilitate the inductance calculation. In conjunction with the calculation of the peak horizontal current, one can then determine the so-called "stored energy" of the coil which is an important performance characteristic of a yoke.

(5) Since the present theory gives separate expressions for the field due to the main body of the yoke and the field due to the end-turns, one can study the effect of the end-turns on the various deflection errors and hence use the geometry of the end-turns as a useful parameter in the design of a yoke.

(6) Finally, one can investigate the radial variation of the various harmonic components across any given cross-section of the coil. This would tell us how the different harmonics increase in strength as the coil is approached. This knowledge is useful in understanding the importance of the various harmonics in determining the yoke performance.

Appendix

The relationship between $H_2(z)$ defined in Sec. 4 and the Fourier components of the field is best obtained by writing H_y near the yoke axis in two ways. A Taylor expansion in Cartesian coordinates yields.

$$H_y = H_0(z) - [H_2(z) + {}^1\!/_2 H_0''(z)]\, y^2 + H_2(z)x^2 + \ldots \qquad \text{[A-1]}$$

On the other hand H_y can be related to the magnetostatic potential harmonics in the following way.[16] The potential $\psi(\rho, \theta, z)$ has a Fourier expansion given by

$$\psi(\rho, \theta, z) = \phi_1(\rho, z)\sin\theta + \phi_3(\rho, z)\sin 3\theta + \ldots \qquad \text{[A-2]}$$

Near the axis,

$$\phi_1(\rho, z) \cong a_1(z)\rho - a_1''(z)\rho^3/8 \qquad \text{[A-3]}$$

$$\phi_3(\rho, z) \cong a_3(z)\rho^3, \qquad \text{[A-4]}$$

so that

$$H_y \equiv \frac{\partial \psi}{\partial y} = -a_1(z) + (x^2 + 3y^2)a_1''(z)/8 - 3(x^2 - y^2)a_3(z). \quad \text{[A-5]}$$

Comparing Eqs. [A-1] and [A-5], we get

$$H_0(z) = -a_1(z) \quad \text{[A-6]}$$

$$H_2(z) = +\frac{a_1''(z)}{8} - 3a_3(z). \quad \text{[A-7]}$$

Since

$$H_\rho^1(0, z) = H_0(z) = -a_1(z) \quad \text{[A-8]}$$

$$\text{and } H_3^\theta(\rho, z) = -\frac{3}{\rho}\phi_3(\rho, z), \quad \text{[A-9]}$$

we can write Eq. [A-6] as

$$H_2(z) = -\frac{H'\rho''(0, z)}{8} + \left\{\frac{1}{\rho^2} H_3^\theta(\rho, z)\right\}_{\rho = 0}. \quad \text{[A-10]}$$

This formula has been used in the paper to calculate $H_2(z)$.

References:

[1] R. G. E. Hutter, "Electron Beam Deflection—Part II. Applications of the Small-Angle Deflection Theory," *J. Appl. Phys.*, **18**, p. 797 (1947).
[2] J. Haantjes and G. J. Lubben, "Errors of Magnetic Deflection, II," *Philips Res. Rep.*, **14**, p. 65 (1959).
[3] J. Kaashoek, "A Study of Magnetic-Deflection Errors," *Philips Res. Rep.*, Suppl. **11**, p. 1 (1968).
[4] N. H. Dekkers, "A Universal Deflection Unit Generating a Field of Any Order and Azimuth," *J. Phys. D: Appl. Phys.*, **7**, p. 805 (1974).
[5] H. Ohiwa, "The Design of Deflection Coils," *J. Phys. D: Appl. Phys.*, **10**, p. 1437 (1977).
[6] D. E. Lobb, "Properties of Some Useful Two-Dimensional Magnetic Fields," *Nucl. Instrum. Methods*, **64**, p. 251 (1968).
[7] M. E. Carpenter, R. A. Momberger, and T. W. Shultz, "Application of Computer Modeling to Color Television Picture Tube Systems," *IEEE Trans. Consumer Electronics*, **CE-23**, p. 22 (1977).
[8] D. M. Fye, "An Integral Equation Method for the Analysis of Magnetic Deflection Yokes," *J. Appl. Phys.*, **50**, p. 17 (1979).
[9] Y. Yokota and T. Toyofuku, "The Calculation of the Deflection Magnetic Field and The Electron-Beam Trajectory for Color Television," *IEEE Trans. Consumer Electronics*, **CE-25**, p. 91 (1979).
[10] See, e.g., W. H. Hayt, *Engineering Electromagnetics*, 4th Ed., McGraw-Hill, N.Y. (1981), pp. 238–241.
[11] I. S. Gradshteyn and I. M. Ryzhik, *Table of Integrals, Series, and Products*, Academic Press, N.Y. (1980), pp. 389 and 1039–1045.
[12] See pp. 948–949 of Ref. [11].
[13] W. A. L. Heijnemans, M. A. M. Nieuwendijk, and N. G. Vink, "The Deflection Coils of the 30AX Color-Picture System," *Philips Tech. Rev.*, **39**, p. 154 (1980).
[14] B. B. Dasgupta, "Effect of Finite Coil Thickness in a Magnetic Deflection System," *J. Appl. Phys.*, **54**, p. 1626 (1983).

[15] J. Haantjes and G. J. Lubben, "Errors of Magnetic Deflection, I," *Philips Res. Rep.*, **12,** p. 46 (1957).
[16] F. J. Campbell, private communications.
[17] B. B. Dasgupta, "Theory of Large-Angle Deflection of Electrons in the Magnetic Field Inside a Television Tube," *RCA Rev.*, **43,** p. 548 (1982).
[18] B. B. Dasgupta, "Calculation of Inductance of the Horizontal Coil of a Magnetic-Deflection Yoke," *IEEE Trans. Consumer Electronics*, **CE-28,** p. 455 (1982).

A Simple Method to Determine Series Resistance and κ Factor of an MOS Field Effect Transistor

S. T. Hsu
RCA Laboratories, Princeton, NJ 08540

Abstract—A simple method to determine the parasitic source/drain series resistance and κ factor of MOSFET's is presented. The parasitic source/drain series resistance and the κ factor of a MOSFET can be determined by measuring the dc drain current of the device operated in the linear region under moderate gate biases. The results also showed that the mobility of electrons or holes in the surface inversion layer is practically independent of gate bias voltage.

1. Introduction

The advanced MOS technology has led to the fabrication of very small geometry MOS VLSI's. The characteristics of scaled MOSFET's are very sensitive to the parasitic source/drain series resistance and to the effective channel length of the device. These two parameters can severely affect the performance of MOS VLSI. Suciu et al[1] published an experimental derivation method to determine the source/drain series resistance of MOSFET's. Their derivation is very complex. Strong mobility degradation due to gate field is also involved. In a recent article Schwarz et al[2] showed that the gate field should play no direct role in mobility degradation. Methods of determining the parasitic source/drain series resistance and the effective channel length of the MOSFET's were also presented by Chern et al[3] and by Peng et al.[4] Their measurements require more than one MOSFET operated at very large gate voltages.

This paper presents a simple method using a single MOSFET biased at moderate gate voltages and operated in the linear region of the drain current-voltage characteristics to determine the para-

sitic source/drain series resistance and the κ factor of the device. The effective channel length and the effective channel width of MOSFET's can also be determined if the κ factors of two different size MOSFET's are measured.

2. Measurement Method

The drain current of MOSFET's operated in the linear region is given by:

$$I_D = \kappa\{(V_G - V_T - \frac{1}{2}V_D)\, V_D - \frac{2\sqrt{2\epsilon_s qN}}{3\ C_{ox}}[(V_D + 2\phi_F)^{3/2} - (2\phi_F)^{3/2}]\}, \quad [1]$$

where $\kappa = W\mu C_{ox}/L$. Unless specified all the notations are standard ones. In Eq. [1] we have assumed that the substrate is uniformly doped, the mobility of electrons or holes in the surface inversion layer is independent of gate biases, and there is no parasitic source/drain series resistance. When the drain bias voltage is small, the last term of Eq. [1] can be neglected. Eq. [1] is then applicable to MOSFET's made on a substrate with any impurity profile.

There are parasitic series resistance, R_s and R_D, at the source and the drain, respectively, of any parasitic MOSFET's. These parasitic resistances can significantly degrade the characteristic of short channel MOSFET's. The equivalent circuit of a MOSFET is sketched in Fig. 1 where R_l is the input resistance of a current meter. It is obvious that the drain current of Eq. [1] becomes

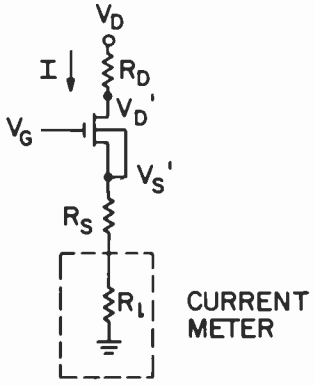

Fig. 1—Equivalent circuit of a MOSFET.

$$I_D = \kappa\{V_G - V_T - I_D\,(R_s + R_l) - \frac{1}{2}[V_D - I_D\,(R_s + R_D + R_l)]\}$$

$$[V_D - I_D\,(R_s + R_D + R_l)]$$
$$\simeq \kappa[V_G - V_T - \frac{1}{2}V_D]\;[V_D - I_D\,(R_T + R_l)], \qquad [2]$$

provided

$$V_G - V_T - (V_d/2) \gg (I/2)|R_D - R_s - R_l|.$$

In Eq. [2] R_T is equal to the sum of R_s and R_D. After some manipulations the following result is obtained:

$$I_D = \frac{\kappa(V_G - V_T - \frac{1}{2}V_D)V_D}{1 + (R_T + R_l)\,\kappa(V_G - V_T - \frac{1}{2}V_D)}. \qquad [3]$$

Therefore

$$\frac{1}{I_D} = \frac{R_T + R_l}{V_D} + \frac{1}{\kappa(V_G - V_T - \frac{1}{2}V_D)V_D} \qquad [3A]$$

The result of Eq. [3A] indicates that I_D^{-1} is a linear function of R_l. When I_D^{-1} is plotted as a function of R_l with V_G as a parameter, a family of parallel straight lines is obtained. The slope of this family of straight lines is equal to V_D^{-1}. The extrapolation of these straight lines intersect the R_l axis at $R_{lo}(V_G)$, such that

$$-R_{lo}(V_G) = R_T + \kappa^{-1}\,(V_G - V_T - \frac{1}{2}V_D)^{-1}. \qquad [4]$$

The $R_{lo}(V_G)$ is, therefore, a linear function of $[V_G - V_T - (V_D/2)]^{-1}$. The slope of this straight line is equal to κ^{-1}. This straight line intersects the $R_{lo}(V_G)$ coordinate at R_T. Therefore, from the plot of $R_{lo}(V_G)$ versus $[V_G - V_T - (V_D/2)]^{-1}$, the parasitic source/drain series resistance and the κ factor of the MOSFET can be determined. The measurement procedure is simple. The accuracy is excellent as can be seen from the experimental data presented in the next section.

3. Experimental Results and Discussion

The MOSFET's used in this work are n- and p-channel test transistors from MOS integrated circuits. The method applies very well to both types of MOSFETs. Therefore, we shall present the results taken from n-channel MOSFETs only. The nominal channel length and channel width of the n-channel MOSFETs used are equal to 2 μm and 50 μm, respectively. The drain current of the MOSFET was plotted in Fig. 2 as a function of gate bias voltages. The drain voltage is equal to 0.1V. The drain current is calculated from the voltage drop across a load resistance of 10Ω. The same measurements were also made for R_l equal to 100Ω, 215Ω, and 422Ω. The results are not shown here. The threshold voltage of the MOSFET was also determined from this I-V curve and was found to be equal to 0.85V. The data are replotted in Fig. 3 in the form of I_D^{-1} versus R_l with V_G as a parameter. A family of parallel straight lines is evident. The slope of the straight lines is equal to 10 V^{-1} which is

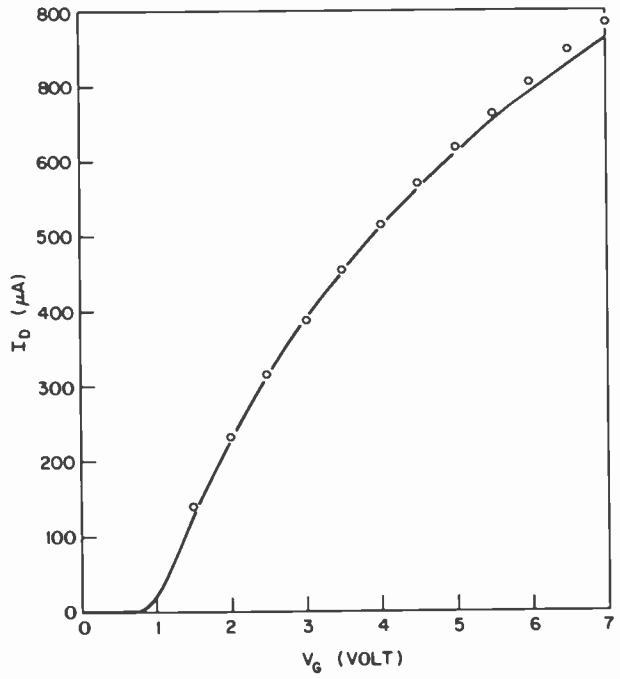

Fig. 2—The linear region transconductance of a typical n-channel MOSFET. Curve is measured and points are calculated.

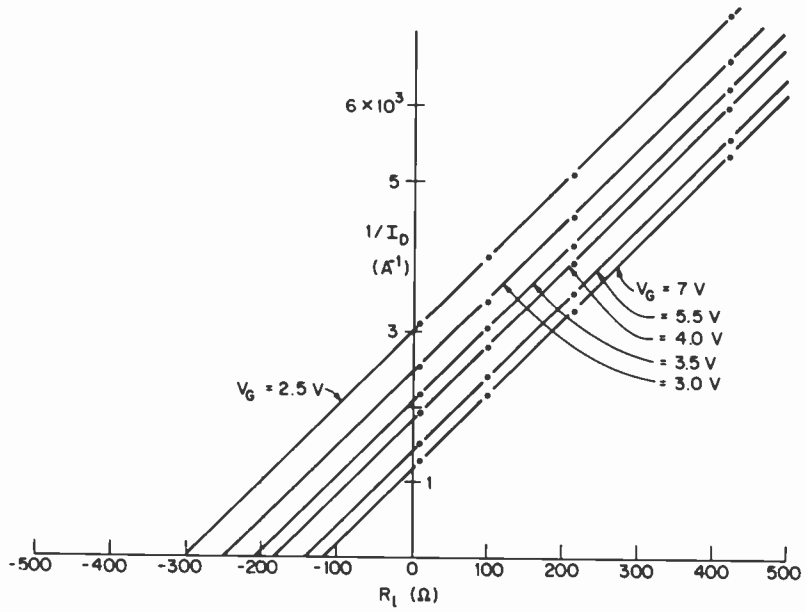

Fig. 3—$1/I_D$ versus R_l of the n-channel MOSFET used in Fig. 2.

equal to V_D^{-1} as is expected. The data taken from $V_G = 2.5$V do not fit a straight line well. This is because the condition of Eq. [2] is marginally satisfied at this gate bias voltage. Extrapolating these straight lines, we obtained $R_{lo}(V_G)$. The results are plotted as a

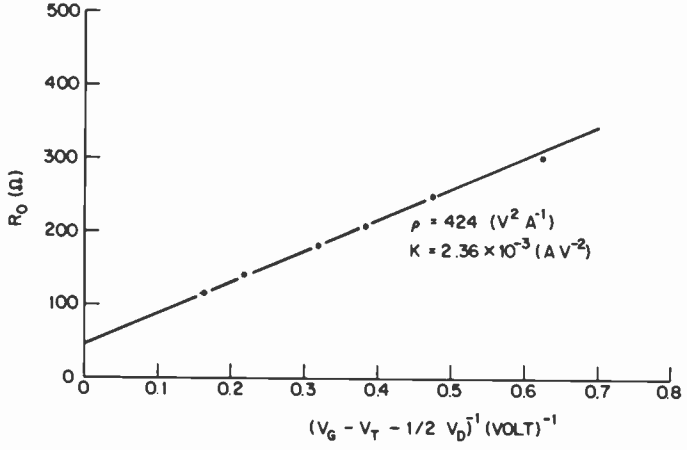

Fig. 4—$R_{lo}(V_G)$ versus $[V_G - V_T - (V_D/2)]^{-1}$ characteristic of the n-channel MOSFET used in Fig. 2.

function of $[V_G - V_T - (V_D/2)]^{-1}$ in Fig. 4. All data points except the one when $V_G = 2.5$V follow a straight line well. This straight line intersects the $R_{lo}(V_G)$ axis at 46. The slope of the straight line is equal to 424 V^2/A. Therefore, the parasitic source/drain series resistance of this MOSFET is equal to 46Ω and the κ factor of the device is equal to 2.36×10^{-3} A/V^2.

The drain current of the device was calculated from Eq. [3] using the measured R_T and κ values and the load resistance of 10Ω to crosscheck the accuracy of this measurement. The calculated data points were superimposed in Fig. 2. The calculated points are slightly larger than the measured values at large gate biases. This is due to a small degradation of effective mobility of electron in the surface inversion layer at large gate fields. At $V_G = 7$V the effective electron mobility is approximately 3% smaller than that at small gate biases.

Acknowledgment

The author would like to thank D. W. Flatley and M. Jones for device fabrication and to S. Davis for electrical measurements.

References:

[1] I. Suciu and R. L. Johnston, "Experimental Derivation of the Source and Drain Resistance of MOS Transistors," *IEEE Trans. Electron Dev.*, **ED-27,** No. 9, p. 1846, Sept. 1980.
[2] S. A. Schwarz and K. K. Thornber, "Comments on Mobility Degradation Due to the Gate Field in the Inversion Layer of MOSFETs," *IEEE Electron Dev. Lett.*, **EDL-4,** No. 1, p. 11, Jan. 1983.
[3] J. G. J. Chern, P. Chang, R. F. Motta and N. Godinho, "A New Method to Determine MOSFET Channel Length," *IEEE Electron Dev. Lett.*, **EDL-1,** No. 9, p. 170, Sept. 1980.
[4] K. L. Peng and M. A. Afeomowitz, "An Improved Method to Determine MOSFET Channel Length," *IEEE Electron Dev. Lett.*, **EDL-3,** No. 12, p. 360, Dec. 1982.

Surface Acoustic Wave Stylus: Part I—Pickup and Recording Devices

S. Tosima,* M. Nishikawa,* T. Iwasa,* and E. O. Johnson*

Abstract—A new type of pickup and recording device was demonstrated using a stylus with a fan-shaped interdigitated transducer electrode (IDT) deposited on its shank. The IDT focusses a beam of Surface Acoustic Waves (SAW) at the stylus tip. The relative transmission or reflection of waves at the tip depends upon the acoustic characteristics of whatever material may contact the tip. The SAW reflected back to the IDT generate an electric signal that can be detected in the driving circuitry to reveal acoustic conditions at the stylus tip. The high concentration of SAW power at the stylus tip allows a very localized determination of such conditions at the contacting material surface. Moreover, when the input electric power level to the IDT is increased, the SAW power density at the stylus tip increases to a level adequate to record information in the contacting surface.

A well-known piezoelectric material, single-crystal quartz, was used as a stylus material to study and demonstrate device principles. Observed phenomena were in good agreement with well established SAW theory; general behavior of the new stylus seems well understood. Simple construction, the ability to concentrate SAW into a small stylus tip area, and very low SAW path losses suggests potentially good performance as pickup and recording devices over a wide range of frequencies.

1. Introduction

Surface acoustic wave (SAW) energy propagates along a material surface within a layer about one wavelength thick. SAW propaga-

* Present address: Corning Research Inc., Machida City, Tokyo, 194–02 Japan.

tion properties are therefore sensitive to acoustic loading on the propagation surfaces.[1,2] If the SAW beam is concentrated by focussing into a small region on the surface, the waves will be particularly sensitive to acoustic loading in that region. The new pickup device described in this paper makes use of the acoustic loading effect from a very small region of a material surface.

The device consists of a pickup stylus with a SAW interdigital transducer (IDT) fabricated on its shank and aimed at the sharpened stylus tip. The electrode fingers are shaped to focus the SAW power at the stylus tip. Wave behavior at the tip depends upon whether or not the tip is touching another material, as well as upon the acoustic characteristics of this material. If no material touches the tip, all the waves are reflected. If a material body touches the tip, some of the wave energy is absorbed in the material. Accordingly, the magnitude and phase of the SAW power reflected back to the IDT is indicative of the acoustic loading at the tip. The reflected wave interferes with the incident wave and modulates the transducer impedance. By this means, information on the acoustic loading at the stylus tip is directly detectable in the external circuitry.

This pickup device detects the acoustic loading at the stylus tip, but not the gross motion of the stylus itself. This is quite different from the principle operative in the widely used audio pickup devices wherein gross mechanical strain in the stylus generates a detectable piezoelectric output signal.

The device can also be used in a recording mode. This capability arises from the high power concentration attainable at the stylus tip when the rf voltage applied to the SAW transducer is increased beyond the level used for readout. The high concentration of SAW power results from three factors: inherent confinement of SAW to an acoustic wavelength of the material surface, focussing effect of the geometry of the stylus tip, and the curved shape of the interdigital transducer (IDT) electrodes.

A watt of electric driving power applied to a stylus operating at several hundred MHz is estimated to result in a SAW power density of the order of 10^6 W/cm^2 at a stylus tip a few μm wide. This level of SAW acoustic power density corresponds to a mechanical stress of about 100 kg-wt/mm^2 and an amplitude of tip motion of several tens of angstroms. Although the SAW power at the stylus tip is not fully transferred to the recording material, it easily transfers a power level sufficient to plastically deform material surfaces touching the stylus tip. This mode of operation, although reminiscent of that of a mechanically vibrating cutting tool, differs in that

the vibrating amplitude of the tip is small and that the stylus itself does not undergo gross vibrational displacement. These features have many practical implications, some favorable, some possibly not.

The purpose of the present work is to study the fundamental behavior of surface acoustic waves in a stylus, and to investigate the dependence of pickup and recording capabilities on various physical parameters, such as radiation resistance, SAW reflectance at the stylus tip, tip size, and the tip contacting force on the material surface. The results of these fundamental studies lead to the optimum conditions for device operation as well as to device design principles.

2. Experimental Arrangement

In these studies, single-crystal quartz was conveniently used as a stylus material. Experimental samples were Y-cut quartz plates, typically 1.5 cm long along an X-axis, 5 mm wide, and 1 mm thick. One end of each plate was sharpened to a 60° angle to make the sharpened tip 10–20 μm wide. The tip was further sharpened into a form like a bow of a boat. The size of the stylus tip is $a \times b$ as shown in Fig. 1 where a is the width along the Z-axis, and b along the Y-axis. These widths were measured with a microscope and have a possible error of about 1–2 μm. Near the tip on the flat surface of the stylus plate, a fan-shaped IDT was deposited as shown in Fig. 1. Each finger of the IDT was curved to take account of the dependence of SAW velocity[3] on the propagation direction. This insured SAW beam focus on the tip. The aperture of the IDT is about 50°, a slightly narrower angle than the tip angle.

About a half of the SAW power generated by the IDT is radiated in a direction opposite to that of the tip. This power, which could have confused our measurements because of multiple reflection effects, was conveniently absorbed with a piece of Scotch tape stuck to the stylus surface behind the IDT. This tape also serves to absorb the SAW power reflected from the tip that passes the IDT without being captured. Only 50% of the SAW power reflected from the tip and returning to the vicinity of the IDT is captured. Conservation of this wasted power was not deemed necessary in these early experiments.

The IDT capacitance C_T was 2.3 pF, and the total impedance of the IDT mostly arises from this capacitance. To compensate this IDT capacitive impedance, a turning inductor was connected in series with the IDT as shown in Figs. 7 and 18. This compensation

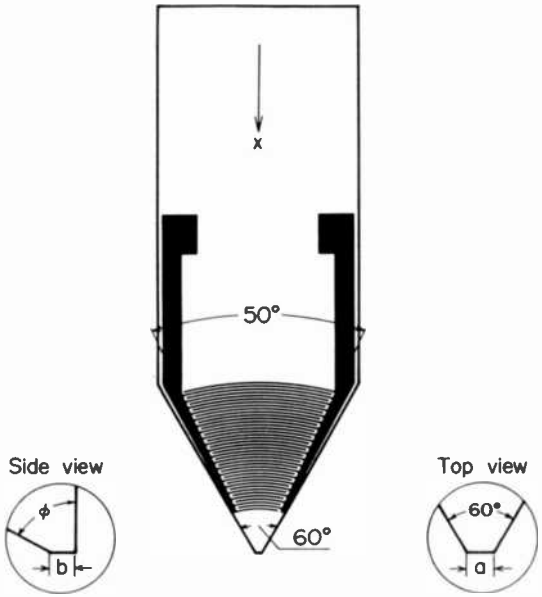

Fig. 1—SAW recording stylus with IDT. The periodicity λ_o of the IDT is 160 μm, and the number N of finger pairs is 20. Distance l between the tip and the IDT center is 2.76 mm. Inserts are top and side views of the stylus tip.

conveniently allows measurement of the impedances associated with the SAW. The IDT radiation resistance and impedance change due to the acoustic loading at the tip were measured with a Hewlett Packard 4815A rf vector impedance meter.

The IDT driving power was supplied by the power source of the vector impedance meter. In these experiments the peak-to-peak voltage V_e supplied to the IDT circuit was about 0.8 mV (see Fig. 18). As described later, the values of the IDT resistance R_f and the circuit series resistance R_S were about 80 Ω and 30 Ω, respectively. The resulting rf power input was about 0.6 nanowatt. The experimental mechanical setup is similar to that of an audio pickup arm. A stylus with a tuning inductor is installed at one end of the arm, and an adjustable counterbalance at the other end to control the stylus contacting pressure.

3. Radiation Resistance

The resistance R_f of the IDT was measured as a function of the driving frequency f when the tip was free from externally applied

acoustic loading. The result is shown in Fig. 2. The oscillatory response (see Fig. 2a) is a typical one with maxima and minima superposed onto the well-known $(\sin x/x)^2$ frequency dependence[4] around the center frequency f_o of 19.68 MHz. This oscillatory response arises from interference between incident waves and waves reflected from the tip. To confirm this interpretation, the surface area between IDT and tip was covered with an absorber.[5] In this case the SAW power launched from both sides of the IDT was absorbed so that no acoustic power was reflected back to the IDT. The effect of wave interference on resistance then disappears as shown in Fig. 2b. The resistance R_f' of the stylus with the absorber at the tip shows a $(\sin x/x)^2$ frequency dependence. Both R_f and R_f' include the same series resistance R_s, typically about 30 Ω. This was determined by replacing the stylus with a capacitor consisting of a

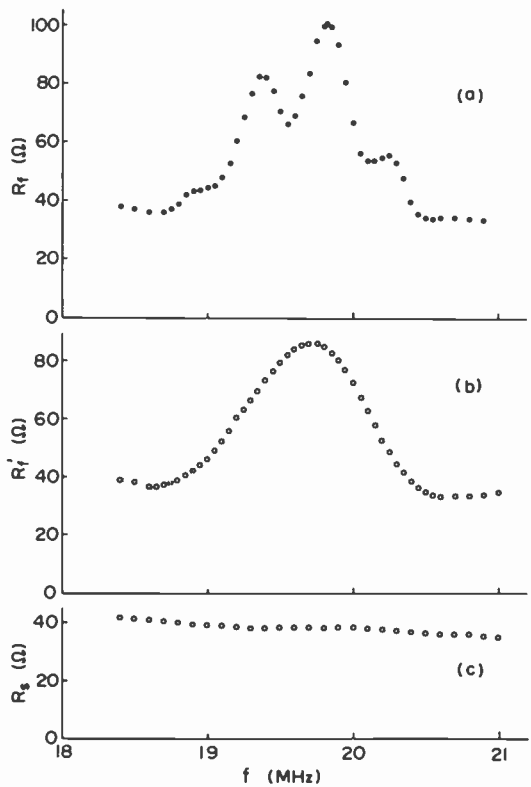

Fig. 2—Real part of circuit impedance. Stylus tip size for this experiment is 12 × 15 μm², and ϕ is about 65°: (a) free tip, (b) tip covered with absorber, and (c) circuit series resistance.

nonpiezoelectric substrate and the same fan-shaped IDT deposited on its surface. The capacitance of this dummy structure is close to the IDT capacitance C_T of an actual stylus. Fig. 2c approximately shows the circuit series resistance R_s, which consists of a tuning circuit component and the IDT electrode component. Little frequency dependence was observed for the series resistance. In similar experiments repeated replacing the IDT with known capacitors, it was found that the series resistance is mostly due to the tuning inductor.

Fig. 3 compares the observed and theoretical frequency dependence of the IDT radiation resistance R_a. The observed value of R_a was obtained by subtracting the circuit series resistance R_s from the observed total resistance R_f. The theoretical curve was calculated using the following equations:

$$R_a = R_a(0)(1 + r\cos\theta), \quad [1]$$
$$R_a(0) = \hat{R}_a(\sin x/x)^2,$$
$$x = N\pi(f - f_o)/f_o,$$
$$\theta = 4\pi l/\lambda = (4l/N\lambda_o)x + \psi,$$

and

$$\psi = 2\pi(2l/\lambda_o - \text{integer}).$$

Here, l is the distance between the tip and the center of the IDT, λ is the SAW wavelength along the x-axis, N is the number of IDT finger pairs, f is the IDT driving frequency, and f_o is the IDT center

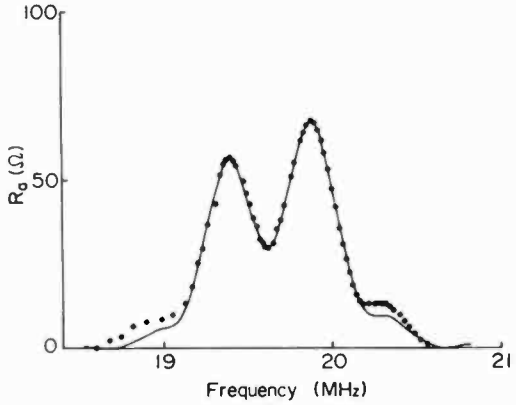

Fig. 3—Radiation resistance of IDT. The solid line is a theoretical curve, and the dots represent experimental values. The tip size is about 20 × 20 μm^2, and ϕ is about 60°.

frequency. In the first of the above equations, the term R_a (0) is the radiation resistance when no SAW are reflected back to the IDT. The second term $r\cos\theta$ in parenthesis represents the effect of the SAW reflected at the tip. In the derivation of Eq. [1], the SAW propagation loss was ignored since it is negligibly small.[6] For details of the derivation of the equations and notations, see Appendix A.

In the calculation of the theoretical curve, the parameter l was 2.76 mm, and ψ was taken as 2.60 radians. The value of ψ was chosen rather arbitrarily because a small error in l gives an appreciable change in ψ. For a detailed discussion, see Appendix A.

The other parameters $\hat{R}_a$ and the reflectance r were taken as 54.2 Ω and 45%, respectively, for the best fit to the observed values. The agreement between theory and experiment is very good, and the frequency dependence of the IDT resistance is well explained by the interference between incident and reflected surface acoustic waves from the stylus tip.

Since the external circuit includes a stray capacitance C_s, the value 54.2 Ω for $\hat{R}_a$ is considered to be affected by C_s. To study the effect of C_s on the IDT characteristics, separate experiments were done using the same fan-shaped IDT deposited on an XY-plate. Reflections were suppressed with absorbers. The observed values of R_a at the center frequency, and the capacitance C_T, were calibrated replacing the IDT with resistors and capacitors of known values. The IDT itself seems to have a stray capacitance. All finger electrodes were removed from the IDT and the remaining capacitance was measured to be about 0.3 pF. This also contributes to the stray capacitance. These measurements gave the value 2.3 pF for C_T, and the value 158 Ω for $\hat{R}_a$.

The electromechanical coupling constant k^2 was calculated to be 0.18% using the expression

$$\hat{R}_a = 2k^2N/\pi^2 f_oC_T, \qquad [2]$$

with C_T = 2.3 pF and $\hat{R}_a$ = 158 Ω. For comparison, k^2 was measured for rectangular-shaped IDTs having straight-finger electrodes deposited on XY-plates. The plates were taken from the same batch as used earlier. The value of 0.21 ± 0.01% for k^2 was obtained and this agrees fairly well with the value of 0.23% reported by Schultz and Matsinger.[7] The value 0.18% for k^2 for the fan-shaped IDT is somewhat smaller than that for a rectangular IDT. In the fan-shaped IDT, the propagation direction is distributed ±25° around the X-axis. Since k^2 is maximum for the X-axis propagation,[3] the

effective value of k^2 for a fan-shaped IDT should be somewhat smaller than the maximum value. Simple averaging of k^2 over the propagation direction gave a value about 90% of the value for the X-axis propagation. If we take the value 0.21% for the latter value, the effective value of k^2 for the fan-shaped IDT is 0.19% and this agrees well with the observed value of 0.18%.

The value of the reflectance r in Eq. (1) is different for different samples, and seems to depend upon the shape of the tip and the accuracy of the IDT location relative to the tip. There is mode conversion from incident SAW to reflected bulk waves depending upon SAW power focussing at the tip. If all of the incident SAW power is converted into bulk waves, the reflectance r should be zero, as discussed in Appendix A. The value of the SAW reflectance r was further studied using an IDT having straight fingers deposited near an edge of a rectangular quartz plate. The fingers were deposited parallel to the edge. The value of r was estimated to be 41% from the oscillatory structure in the IDT resistance-versus-frequency curve of this case. A similar result was obtained using a $LiNbO_3$ plate. The value 45% of r for the present stylus is close to the value found in the rectangular geometry mentioned above.

In the above discussion and in Appendix A, little attention was given to the possibility of mode conversion from bulk waves to SAWs. Some of the bulk waves generated at the tip travel directly to the transducer surface and generate SAW at the surface. The SAW converted from the bulk waves interacts with the IDT electrodes. This component of SAW can not be separated from the one directly reflected at the tip in the present experiments and is involved in the reflected SAW. The other bulk waves travel to the back surface opposite the transducer surface. Some waves are reflected back to the IDT and may affect the IDT resistance. To study this possibility, grooves were cut about 0.2-mm wide and 0.1–0.3 mm deep with a pitch of 0.4–0.6 mm on the back surface. The grooving did not affect the IDT resistance of a stylus with an originally smooth back surface.

Bulk waves are also generated at the IDT[8] and affect the IDT resistance in general. However, spurious structure due to the bulk-wave generation was not observed in the frequency dependence of the IDT resistance as shown in Fig. 2. Good agreement between the observed and theoretical values of radiation resistance R_a also indicates that little power exists in the bulk waves at frequencies near the center frequency f_o.

4. Pickup Device

4.1 Stylus Impedance Change due to Tip Acoustic Loading

When a stylus tip contacts another material, a portion of the incident SAW power is transferred into this material. In addition, there is power transfer into a reflected bulk wave as well as into the SAW beam that returns to the IDT. The amplitude of the reflected SAW is thus modulated and the reflectance r in Eq. (1) changes by an amount Δr. The resistance of the IDT is thereby changed to a new value R_c. Fig. 4 shows the resistance change $\Delta R = (R_c - R_f)$ when a stylus tip contacts a Cu plate. The stylus is the same one used for the radiation resistance measurement shown in Fig. 3. By comparing Figs. 3 and 4, we see that $\Delta R/R_f$ has a peak value (plus or minus) at the frequency where the resistance R_f is either a minimum or maximum. At these frequencies, the input and reflected signals are either in or 180° out of phase, and a strong interaction occurs.

In measuring the total IDT resistance R_f the tuning circuit was adjusted at each frequency such that the imaginary part of the IDT impedance was cancelled when the tip was free. Then when the tip

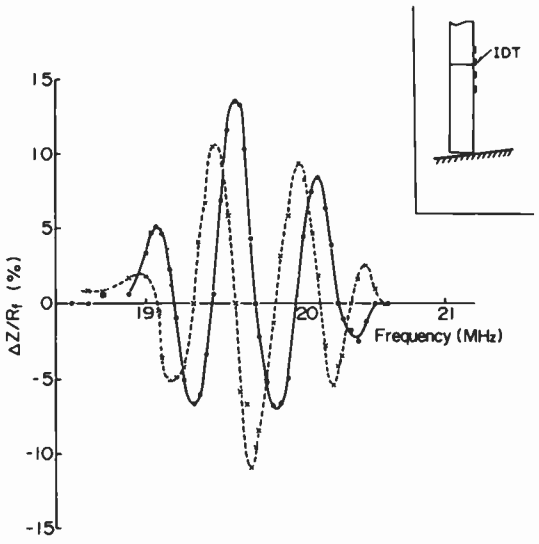

Fig. 4—Impedance change due to acoustic loading. A Cu plate is in contact with the stylus tip. The stylus dead weight is 2.3 g. Dots represent the real component, and crosses the imaginary.

contacts another material, the total impedance changes by an amount ΔZ and an imaginary part appears. The observed result for the imaginary part (crosses) is shown in Fig. 4 along with real part (dots). As expected, the impedance change was observed when the propagation surface side corner of the tip (see Fig. 4 insert) was in contact, but little impedance change was observed when the back surface side corner was in contact. The higher sensitivity to the acoustic loading at the propagation surface side corner than that at the backside corner was further confirmed using a stylus having a tip angle ϕ of 90°.

As derived in Appendix B, the frequency dependence of the impedance change ΔZ is

$$\Delta Z(\mathrm{Re}) = \Delta r \hat{R}_a (\sin x/x)^2 \cos\theta \qquad [3a]$$

and

$$\Delta Z(\mathrm{Im}) = -\Delta r \hat{R}_a (\sin x/x)^2 \sin\theta. \qquad [3b]$$

Fig. 5 shows the theoretical frequency-dependence of the impedance change normalized with respect to $|\Delta r|R_f$. By comparing the theoretical curves in Fig. 5 with the observed ones in Fig. 4, we can see that the frequency dependence of ΔZ is well explained by the reduction in amplitude of the reflected SAW due to power transfer to the contacting material.

Power transfer depends upon contact conditions, the stylus contacting pressure as well as the acoustic properties of the contacting material. Fig. 6 shows the dependence of $\Delta R/R_f$ on stylus dead weight. When the dead weight exceeds a certain value, about 1g in the present case, the impedance change becomes less sensitive to the stylus dead weight. The material dependence of the impedance change $\Delta R/R_f$ and the reflectance change Δr are shown in Table 1. The impedance change for plastics is seen to be smaller than those for the other harder materials.

4.2 Stylus Power and Signal Efficiency

In any signal handling system or transducer, it is usually important to have minimal power losses. This tends to reduce cost and improve signal/noise performance. In the bi-directional IDT of our experiments, about half of the SAW power is launched towards the stylus and the rest in the opposite direction. If the power in the reverse direction is purposely absorbed and discarded, the power transmission loss of the IDT is 3 db. At frequencies below perhaps 1000 MHz,

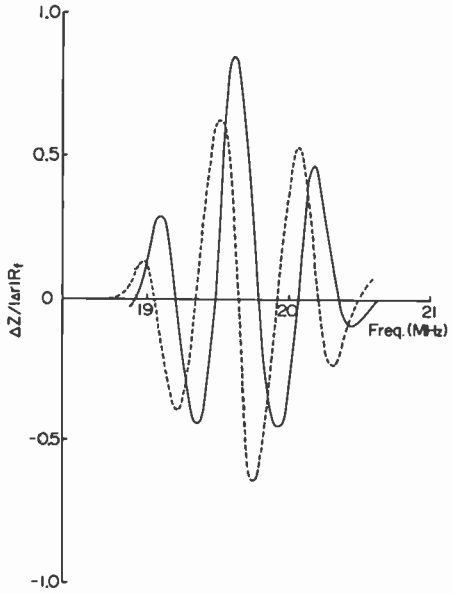

Fig. 5—Theoretical curves for the impedance change ΔZ normalized with $-\Delta r R_f$. The solid and dotted curves are the real and imaginary parts, respectively.

the round trip SAW transmission loss in the stylus material from the IDT to the stylus tip is negligible.

At the stylus tip, the SAW is reflected back to the IDT with amplitude reflectance r and with power reflectance r^2. The remainder

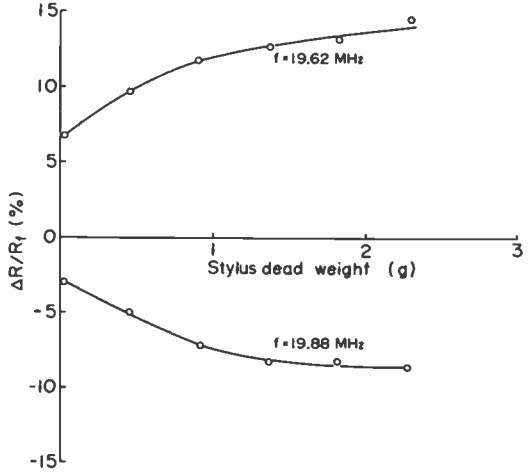

Fig. 6—Dependence of $\Delta R/R_f$ on stylus dead weight.

Table 1—Material Dependence of $\Delta R/R_f$ and Δr at f = 19.62 MHz (Stylus Dead Weight = 2.3 g)

	Cu	Quartz	Glass	Acryl	PVC
$\Delta R/R_f$ (%)	13.6	14.0	9.6	6.2	5.5
$-\Delta r$ (%)	16.0	16.5	11.3	7.3	6.5

of the power is converted into useless bulk waves. The reflected SAW waves suffer a 3-dB loss upon return to the IDT, since half of their power is not captured in the bi-directional IDT and passes on or is reflected back to the tip. Here, the external circuit impedance is assumed to be matched with the IDT impedance. The ratio α of the power recaptured by the IDT to the originally launched SAW power is then given by

$$\alpha = \frac{r^2}{4}.$$

Detailed calculation using the three-port expression of the IDT admittance,[4] see Appendix A, leads us to the modified result for α:

$$\alpha = \frac{r^2}{4}(1 + r\cos\theta + r^2/4). \qquad [4]$$

At frequencies corresponding to the radiation resistance minima, $\cos\theta = -1$, the value of α is maximum and estimated to be 8.4%, or -10.8 dB, using $r = 0.45$ for the free tip as noted earlier.

When the stylus tip is in contact with another material, part of the SAW power is transferred to the material and the reflectance is decreased by Δr. For typical values of Δr see Table 1. Using Eq. [4], the recaptured power is decreased to 2.9% and 5.7% for Cu or PVC, respectively, from the maximum valuc of 8.4% noted above. When signals are recorded on these materials and modulate the acoustic loading at the stylus tip, the recaptured power is also modulated in the range mentioned above. The signal power level we can obtain is then -12.6 dB (5.5%) for Cu and -15.6 dB (2.7%) for PVC.

An improvement of a few db in the above performance could be expected if a somewhat more sophisticated electrode structure were used to reduce the losses at the IDT. Reflectance of SAW power at the stylus tip may be improved by optimizing the tip shape.

4.3 Film Thickness Measurement Demonstration

This was carried out with the arrangement shown in Fig. 7; the stylus was similar to that shown in Fig. 1. The value of this total

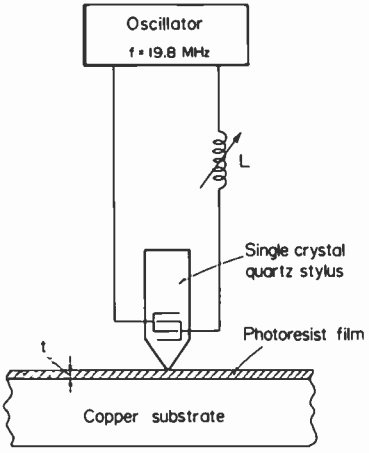

Fig. 7—Apparatus for photoresist film thickness measurement.

resistance was 98.5 ohms when the stylus tip was pulled free of the test sample. When the tip made contact with the sample, the total resistance fell to the values noted in Table 2. Here the multiple values for each value of film thickness correspond to stylus contact at various adjacent locations on the film surface.

The relative input impedance change as a function of film thickness is shown in Fig. 8. The input load resistance changed with film thickness because of acoustic loading effects at the stylus tip. For zero film thickness the stylus tip touches the copper substrate and the acoustic loading is characteristic of the copper itself. As the film thickness is increased, the acoustic loading becomes more and more typical of the film material and decreasingly so of the substrate. Beyond some value of film thickness, depending upon acoustic wavelength and SAW absorption depth, the acoustic loading is purely that due to the film material itself. This is suggested by the results in Fig. 8.

In the present case we believe that the resist material heavily absorbs the SAW at the acoustic frequency used (19.8 MHz). Whatever SAW energy enters the film at this frequency is absorbed in the first few micrometers of path length. Structural features inside the sample beyond this depth cannot be detected. To increase the film thickness observation range, one should use much lower acoustic frequencies, perhaps in the 1 MHz range. This should reduce SAW path absorption. This should be easy to do because all that is needed is a lower frequency oscillator and an appropriately scaled up finger spacing of the IDT.

In conclusion, the feasibility of using a SAW stylus for probing

buried structural features in a sample was demonstrated. A more detailed study is required before practicality compared to other methods can be determined.

5. Recording Device

5.1 Critical Conditions for Recording

To record, the stylus is placed perpendicular to a material surface and the stylus tip contacts the surface with a force (weight) W. An

Table 2—Effect of Film Thickness on Load Resistance

Film Thickness t (μm)	Load Resistance R (ohms)		
(no film in contact with stylus)	98.5		
0.05	95.6		
	95.6		
	95.7		
0.4	95.9		
	96.1		
	96.1		
0.5	96.0		
	96.3		
	96.1		
1.3	96.5	96.5	96.5
	96.6	96.5	
	96.6	96.5	
2.1	96.9	96.7	97.0
	97.0	96.8	96.9
	96.6	96.5	96.9
3.1	97.0	97.3	97.2
	97.0	97.2	
	97.0	97.1	
3.4	97.3	97.3	97.2
	97.7	97.5	97.5
	97.5	97.4	
6.2	97.3		
	97.9		
	97.5		
6.3	97.5		
	97.8		
	97.8		
12.2	97.0		
	98.0		
	98.0		
17.0	97.5		
	97.9		
	97.9		
21.0	97.5		
	98.0		
	97.9		

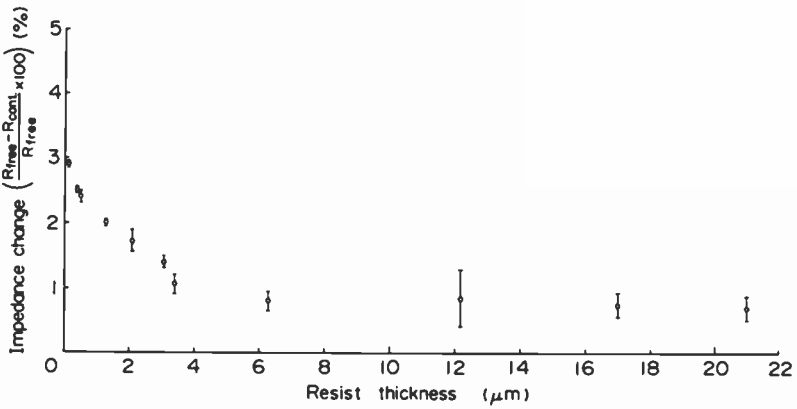

Fig. 8—Effect of resist film thickness on IDT circuit resistance. The tip size of the stylus used in this experiment is about 10 × 10 μm^2 and ϕ is about 70°.

rf pulse with length τ is applied to the IDT through the tuning inductor. Fig. 9 shows the result of recording at various pulse lengths on a polyvinylidene chloride sheet at an applied electric power P_e of 0.62 W. A single pulse was used for each dot. The pulse lengths used for each line of dots were, from right to left, 1.0, 0.75,

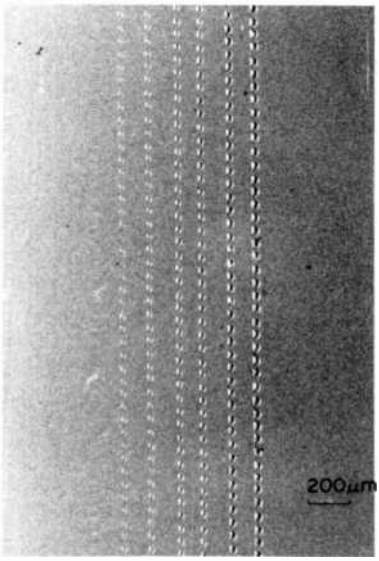

Fig. 9—Recording marks on a polyvinylidene chloride sheet. Tip size is 14 × 18 μm^2, stylus dead weight 0.5, and f is 19.65 MHz. Pulse lengths for each line of dots, from left to right, 1.0, 0.75, 0.50, 0.40, 0.30, 0.25, 0.20, 0.175, 0.15, 0.125, and 0.10 msec. Only results for first six values are clearly visible.

0.50, 0.40, 0.30, 0.25, 0.20, 0.175, 0.15, 0.125, and 0.10 msec. The result of recording, a line of dots, is observable for the first six values of τ, but not for values of τ shorter than 0.2 msec. Accordingly, the critical pulse length τ_c for recording falls between 0.25 and 0.20 msec for a P_e value of 0.62 W. In Fig. 10, the critical pulse length τ_c is plotted against the applied electric power P_e for polyvinylidene chloride (PCS or Saranwrap) and polyvinyl chloride (PVC as used in audio records). When P_e exceeds a certain value, τ_c decreases approximately proportional to P_e^{-2}.

5.2 Frequency Dependence of the Critical Condition

(a) *Frequency Dependence Near the IDT Center Frequency*

Since the radiation resistance is frequency-dependent, the critical condition is also expected to be frequency-dependent. The critical value of the input electric power P_e for recording on a polyvinylidene chloride sheet was measured at various frequencies by applying an rf voltage pulse of a given pulse length τ. The stylus is the same as used for the radiation resistance measurement shown in Fig. 2a. Analysis of the observed radiation resistance using Eq. [1] gave the parameters $\hat{R}_a = 52\ \Omega$, $\psi = -1.975$ radians, and $r = 0.36$. The critical values of P_e for a pulse length of 10 msec are plotted as a function of frequency in Fig. 11 (compare with Fig. 2a). The minima and shoulders (or maxima) of the P_e versus frequency curve correspond to the minima and maxima of the R_f versus frequency curve, respectively. As the frequency f deviates further from the center frequency f_o (19.70 MHz), the critical value of P_e increases. At off-resonance frequencies the radiation resistance R_a becomes lower than the circuit series resistance R_s, and most of the input power is lost in the circuit.

The total acoustic power P_a emanating from an IDT, and the SAW power P_{SAW} propagating to a stylus tip are estimated using the input electric power P_e and the characteristics of the stylus. The total acoustic power P_a includes P_{SAW}, and the power P_{SAW}' radiated from the IDT in a direction opposite from that of the tip. The power P_{SAW}' is absorbed by a piece of Scotch tape stuck to the stylus surface. In consequence, P_a and P_{SAW} can be expressed by:

$$P_a = (R_a/R_f)P_e = [R_a(0)(1 + r\cos\theta)/R_f]P_e \qquad [5]$$

$$P_{SAW} = [(1 - r^2)R_a(0)/2R_f]P_e. \qquad [6]$$

For derivation of these equations, see Appendix C.

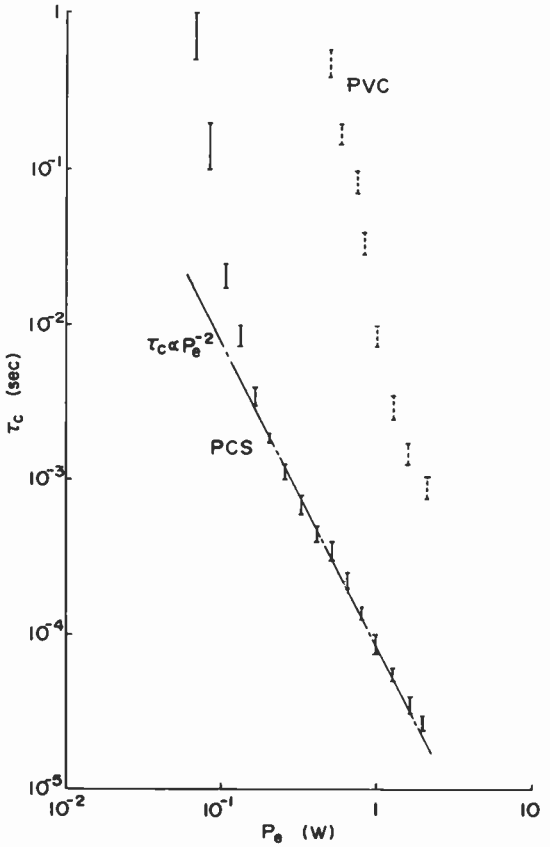

Fig. 10—Critical pulse length τ_c versus P_e plot for polyvinylidene chloride (PCS) and polyvinyl chloride (PVC). Stylus same as in Fig. 2. Stylus dead weight 1 g and f is 19.55 MHz.

The power responsible for recording is not the electrical power P_e but the acoustic power P_{SAW} propagating to the stylus tip. The values of the total acoustic power P_a and the power P_{SAW}, corresponding to the critical values of P_e, were calculated using Eqs. [5] and [6] and are plotted in Fig. 11. Note that the value of P_{SAW} is almost independent of frequency f, indicating that the power responsible for recording is P_{SAW}, as might be expected. The solid curve shown in Fig. 11, associated with the total acoustic power P_a, is calculated using the expression, derived from Eqs. [5] and [6],

$$P_a = [2(1 + r\cos\theta)/(1 - r^2)]P_{SAW} \qquad [7]$$

and the averaged value of 0.42 W for P_{SAW}. Agreement with experiment is seen to be very good.

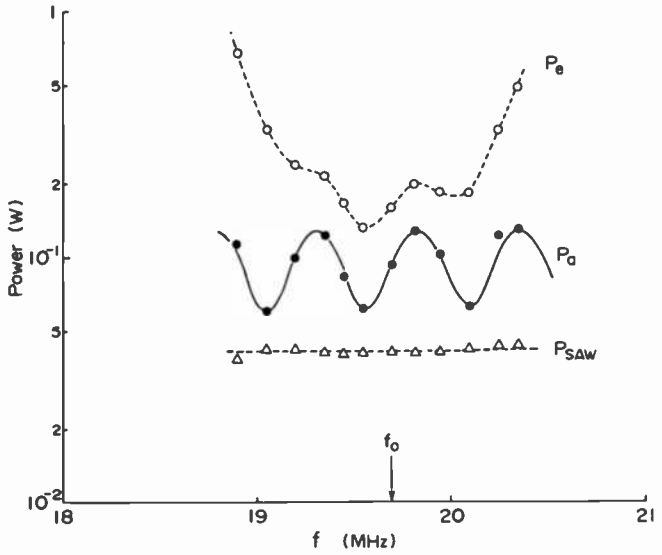

Fig. 11—Frequency dependence of the critical values of P_e, P_a, and P_{SAW} for recording. Pulse length 10 msec. Stylus same as in Figs.2 and 10. Stylus dead weight 0.5 g.

At the minima ($\cos\theta = -1$) of P_a or R_a, about 70% ($= [1 + r]/2$) of the total acoustic power is transmitted to the tip. While at the maxima ($\cos\theta = 1$), only about 30% ($= [1 - r]/2$) is transmitted. This behavior is the result of interference between incident and reflected SAW's. The SAW reflected back from the stylus tip is partially captured by the IDT and partially passes through. This reinforces or interferes with SAW radiated from the IDT in the direction opposite to the tip. In any case, the oppositely moving waves are absorbed by the absorber on the surface behind the IDT. At the minima, the interference is subtractive to reduce the SAW power P_{SAW}' lost in the absorber. At the maxima the interference is additive to increase the absorbed SAW power P_{SAW}'. This results in inefficient recording. The results indicate that the optimum condition for recording (the lowest P_e required) is obtained for the IDT having a radiation minimum close to the center frequency f_o. This condition can be achieved by careful positioning of the IDT on the stylus surface; the frequencies at the minima or the maxima of the radiation resistance depend upon the distance between the IDT and the tip.

(b) *Wide-Range Frequency Dependence*

The recording capability of the stylus is increased when the power P_{SAW} is highly concentrated at the tip. One way to do this is to use

shorter SAW wavelengths. Most of the SAW power is then concentrated within a wavelength of the propagation surface and is thus more highly concentrated at the tip. This dependence was studied in experiments using the same quartz stylus to keep tip geometry and contact conditions invariant. To change the SAW wavelength, the IDT used at a particular frequency was etched off after each experiment and a new IDT having a different center frequency was deposited. The critical electric power P_e was measured by applying an rf voltage pulse; the corresponding value of P_{SAW} was estimated as described in the preceding section. Typical results for P_{SAW} at 1 msec pulse lengths are plotted as a function of f in Fig. 12. As expected, the result shows that the SAW power required for recording decreases as the SAW frequency is increased. The critical value of P_{SAW} is approximately proportional to $f^{-1.5}$. The detailed mechanism for this specific frequency dependence is not clear.

5.3 Dependence of Maximum Input Power on Finger Pair Number

High SAW power at the tip is obtained by increasing the input electric power P_e. However, this is limited by dielectric breakdown between the IDT electrodes, and this is particularly dependent upon the electrode finger pair number N. An rf voltage V_e was applied to the IDT through a tuning inductor, and the critical voltage V_c

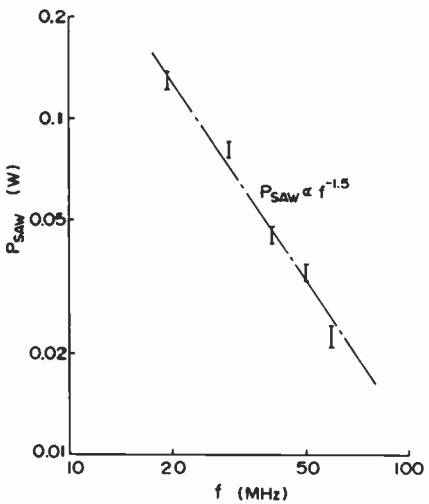

Fig. 12—Frequency dependence of the critical value of P_{SAW}. Tip size 9 × 9 μm², stylus dead weight 0.5 g.

for breakdown was observed for various values of N. The value of P_e and the total acoustic power P_a at breakdown were then estimated. The value of N was changed by removing the same number of finger pairs from both ends of the IDT to keep the average length of finger electrodes of the fan-shaped IDT constant. This also held the distance between the center of the IDT and the stylus tip constant. Experimental results at 19.75 MHz are shown in Table 3. Here C_T is the IDT capacitance, and V_{IDT} is the voltage across the IDT electrodes. The values of V_{IDT} corresponding to V_C were calculated using the following relationships:

$$V_{IDT} = Q\ V_c \qquad [8]$$

$$Q^{-1} = \omega C_T R_f.$$

The threshold voltage for dielectric breakdown across an air gap between two parallel plate electrodes[9] is estimated to be about 1.2 kV, peak to peak, for a similar electrode spacing of 40 μm. Experimental values of V_{IDT} listed in Table 3 are somewhat higher than this value for the parallel plate electrodes. The discrepancy is considered to be due to the difference in electrode geometries.

In Fig. 13, the breakdown limited value of the total acoustic power P_a is plotted against the finger pair number N. The acoustic power P_a is approximately proportional to N^2. As shown in Appendix C, P_a is given in terms of V_{IDT} as

$$P_a = (\omega C_T)^2 R_a(0)(1 + r\cos\theta)V_{IDT}^2/8. \qquad [9]$$

Here, $R_a(0)$ is independent of N.[4] V_{IDT} does not depend on N but on the spacing between finger electrodes. The phase difference θ is also N-independent, since the distance between the center of the IDT and the tip was held constant. The reflectance r was also held invariant using the same stylus throughout the experiments. The N-dependence of P_a appears only through the capacitance C_T which is proportional to N, and this agrees with experiment. The result indicates that higher power can be applied to IDT electrodes having more finger pairs, or a larger IDT capacitance.

Table 3—N-Dependence of C_T, V_c and V_{IDT}.*

N	20	16	12	8
C_T(pF)	2.7	2.3	1.8	1.5
V_c(V)	56	43	34	25
V_{IDT}(kV)	1.6	1.6	1.6	1.7

* For V_c and V_{IDT}, the peak-to-peak value was taken. The stylus tip size was 10 × 10 μm^2 and the spacing between neighboring finger electrodes was about 40 μm.

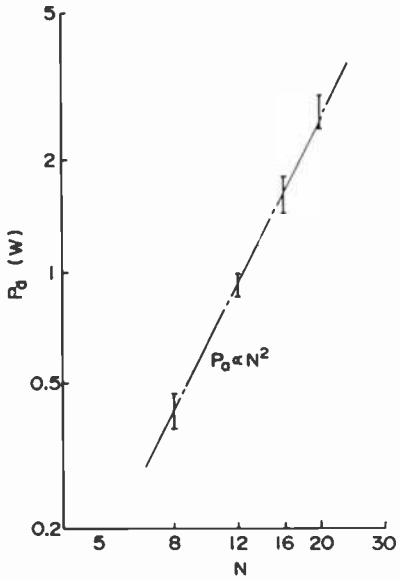

Fig. 13—*N*-dependence of the breakdown-limited value of P_a.

In a strict sense, observed values of IDT capacitance C_T and radiation resistance R_a are subject to the effect of stray capacitance C_s in the circuit. The effect of C_s is discussed in Appendix D. Modification of radiation resistance by C_s is compensated by IDT capacitance, and no modification is necessary for the N-dependence of P_a mentioned in the preceding paragraph.

5.4 Stylus Tip Size and Dead Weight Dependence

Recording capability is different for different styli and seems to depend upon conditions of contact between the stylus tip and recording material surface. Contact conditions include tip size $a \times b$, sharpness of tip edges, and stylus contact pressure determined by stylus dead weight W. Fig. 14 shows typical examples of the dependence of critical pulse length τ_c, for a given P_{SAW}, on stylus dead weight W. When the stylus dead weight exceeds a certain value W_o, the critical pulse length becomes less sensitive to contact pressure. Similar behavior was observed in the stylus impedance change due to the tip acoustic loading. The values of W_o for various tip sizes, $a \times b$, are shown in Table 4. This shows that the contact pressure at W_o is roughly constant for various values of the area ab of the tip. It is to be noted that, except in this instance, the weight used in all

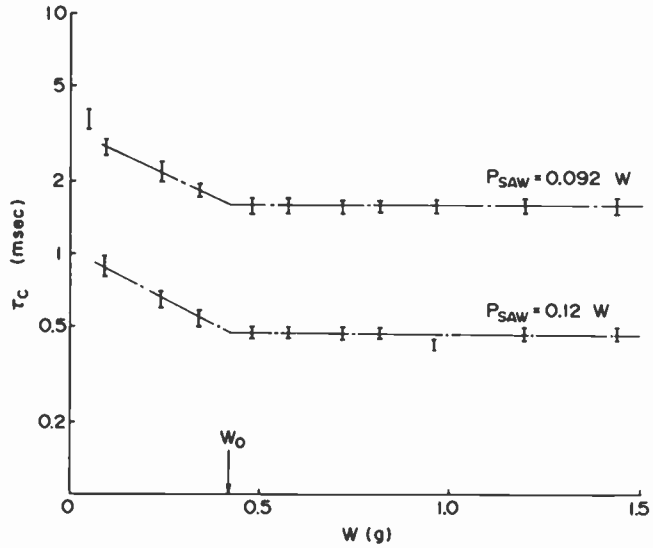

Fig. 14—Dependence of critical pulse length τ_c on stylus dead weight W. Tip size 20 × 20 μm^2 and f is 19.70 MHz.

experiments of this paper were chosen to be larger than W_o to make the observed results relatively insensitive to contact pressure.

Dependence of the critical recording condition on tip size was also studied. A quartz stylus having a tip size of 10 × 10 μm^2 was carefully polished at the tip to enlarge the size first to 14 × 18 μm^2 and then to 25 × 20 μm^2. For each tip size, the critical SAW power necessary for recording was measured. The SAW power density at the tip is defined by $P_{SAW}/a\lambda$ since the SAW power is confined within an acoustic wavelength $\lambda(\sim 160\ \mu m)$ of the propagation surface and is concentrated at the tip having the width a. The results obtained are listed in Table 5 where it can be seen that the critical SAW power density remains roughly constant for a given value of the critical pulse length τ_c. For a ten-fold decrease in τ_c, the critical power density is seen to increase 2 to 3 times.

Table 4—Tip Size Dependence of the Stylus Dead Weight W_o.

Tip size (ab μm^2)	10 × 10	14 × 18	20 × 20	25 × 22	32 × 26
W_o (g)	0.12	0.29	0.42	0.67	1.10
Pressure W_o/ab ($g/\mu m^2 \times 10^{-3}$)	1.2	1.2	1.1	1.2	1.3

Table 5—Dependence of Critical SAW Power on Tip Size.

Tip size (μm^2)	10 × 10	14 × 18	25 × 20
Critical SAW power (watts)			
@ 1 msec (τ_c)	0.075 ± 0.04	0.10 ± 0.01	0.14 ± 0.01
@ 0.1 msec (τ_c)	0.19 ± 0.01	0.24 ± 0.02	0.50 ± 0.05
Critical SAW power density (kw/cm^2)			
@ 1 msec (τ_c)	~4.7	~4.5	~3.5
@ 0.1 msec (τ_c)	~12	~11	~12.5

5.5 Recording Mechanism

The recording mechanism seems to be some combination of the following processes:

1. Heating of the stylus tip from the high SAW power concentration. Heat transfers to the recording surface where a steep rise in temperature thermally alters the material.
2. Acoustic power passes from the stylus tip into the material and is converted to heat. This heat thermally alters the material surface.
3. The material is mechanically altered by the stresses associated with the acoustic power transferred from the tip.

To find out whether recording is due to ordinary thermal heat transfer from the tip (process 1), or due to the acoustic power transferred into the material (process 2 or 3), a small area of the SAW propagation surface, near but not at the tip, was covered with a small amount ($\lesssim$0.1 mg) of an acoustic absorber.[5] The SAW power was thereby partially absorbed by the absorber and converted to heat inside the stylus near the tip. This results in a temperature rise at the tip but, at the same time, reduces the SAW power at the tip. Experiments were done with *h*eat *s*ensitive *p*apers (HSP) (National Chart Paper, Matsushita Comm. Ind. Co.) and *p*olyvinylidene *c*hloride *s*heets (PCS) (Saranwrap). The heat sensitive papers turn blue at temperatures higher than about 70°C. The polyvinylidene chloride sheets deform and melt at temperatures higher than about 60°C and 140°C, respectively. With the heat sensitive papers, recording capability was found to be improved by applying the absorber. That is, the SAW power P_{SAW} necessary for recording was 20 to 30% decreased, even though the SAW power was partially absorbed and the power at the tip was decreased. In this case, process 1 seems most probable. However, in the polyvinylidene chloride sheets, the recording capability decreased. The SAW power required

for recording increased by a factor of 1.8 to 2.7, depending upon pulse length. These results suggest that recording in plastic material, such as polyvinylidene chloride, is not due to ordinary heat transfer from the tip (process 1), but rather to acoustic power transfer (process 2 or 3).

The acoustic power transferred to the material is related to the SAW power P_{tip} at the stylus tip. Before the application of an absorber, P_{tip} is equal to P_{SAW}. For a stylus with an absorber, P_{tip} is estimated from the following expression:

$$P_{tip} = [r_a (1 - r^2)/r (1 - r_a^2)]P_{SAW}. \quad [10]$$

Here r_a and r are the SAW reflectances appearing in the stylus radiation resistance, Eq. [1], with and without the absorber, respectively. Derivation of Eq. [10] is given in Appendix E. For the particular stylus used, $r = 0.33$ and $r_a = 0.14$. Thereby, $P_{tip} = 0.37\ P_{SAW}$.

As seen in Fig. 15, the critical SAW power P_{tip} for the heat sensitive paper (HSP) was decreased about 1/3 by applying the absorber. This clearly shows that the dominant recording mechanism here is not the acoustic power transfer (process 2 or 3), but rather heat generation in the stylus followed by transfer to the recording material (process 1). On the other hand, for the polyvinylidene chloride sheet (PCS) the result for the stylus with or without the absorber is quite similar. However, comparison of the PCS plots indicates some contribution from tip heat transfer at larger values of τ_c. Although the acoustic power transferred from the tip into the material seems to be important for recording, these experiments do not distinguish between processes 2 and 3.

In acoustically very lossy materials, such as plastics, the transferred acoustic power is converted into heat, and process 2 becomes an important recording mechanism. To study the power conversion into heat in a material, recording experiments were done on heat sensitive paper through a polyvinylidene chloride sheet whose 10-μm thickness is comparable to the $12 \times 15\ \mu m^2$ stylus tip size. The result was compared with that of recording directly on the paper. If the acoustic power transferred into the sheet is not converted directly into heat, the sheet would act to impede heat transfer from the tip to the paper: more SAW power would then be required compared to direct recording. On the other hand, if acoustic power is converted into heat in the sheet, the heat should be transferred to the paper surface to assist recording action on the paper; there will be a tendency to require less SAW power than with direct recording. Fig. 16 shows the critical pulse length τ_c versus P_{SAW} plots for the

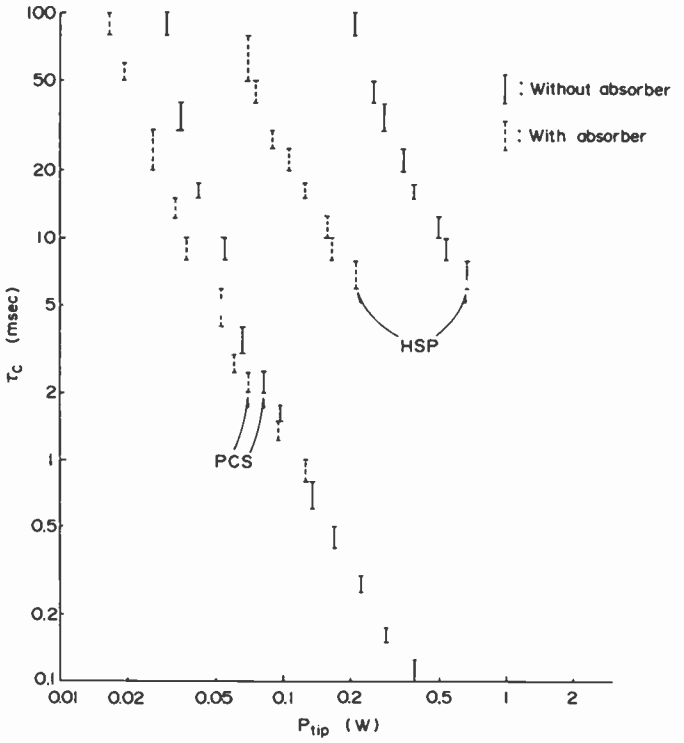

Fig. 15—τ_c versus P_{tip} for polyvinylidene chloride sheet (PCS) and heat sensitive paper (HSP). Tip size 22 × 28 μm^2, stylus dead weight 1 g, and f is 19.80 MHz.

direct and through-the-sheet recordings. For P_{SAW} less than about 0.4 W and times τ_c longer than about 2×10^{-3} second, through-the-sheet recording indeed requires significantly less SAW power than direct recording. The result shows that the acoustic power transferred from the tip is converted to heat in the polyvinylidene chloride sheet, and this heat is then transferred to the paper. This action tends to be less effective for small values of τ_c because of the time required for temperature to rise through the plastic sheet; there may be other reasons as well. The possibility of some mechanical cutting action in the sheet, process 3, is not ruled out. We believe that the recording mechanism in plastic materials is a combination of processes 2 and 3. Generated heat softens the material to ease mechanical energy requirements.

Process 3 should tend to dominate for recording on a metal surface, since the melting temperature and thermal conductivity are high compared with plastic materials, and acoustic path losses are

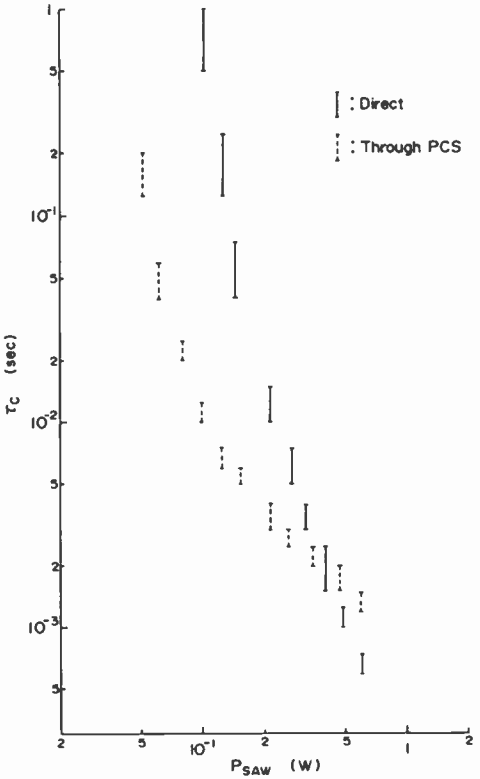

Fig. 16—τ_c versus P_{SAW} for recording directly, or through a polyvinylidene chloride sheet (PCS) located on top of heat sensitive paper. The PCS thickness is about 10 μm and comparable with the tip size 12 × 15 μm². Stylus used in this experiment same as in Figs. 2, 4, and 5. Stylus dead weight is 1 g and *f* is 19.55 MHz.

usually less. To study the possibility of process 3, recording on a copper plate was made with a quartz stylus. A typical example of the results is shown in Fig. 17. Here τ_c was approximately proportional to $P_{SAW}{}^{-2}$. In process 3, the stylus tip sharpness, hardness, and orientation with respect to the recording surface will be important. Unfortunately, quartz probably is not an adequate stylus material for detailed studies of recording on a metal surface. Quartz is a rather fragile material and is difficult to shape into a tip having well defined sharp edges. Irregular edges would tend to have a relatively large effect on the efficiency of direct mechanical cutting.

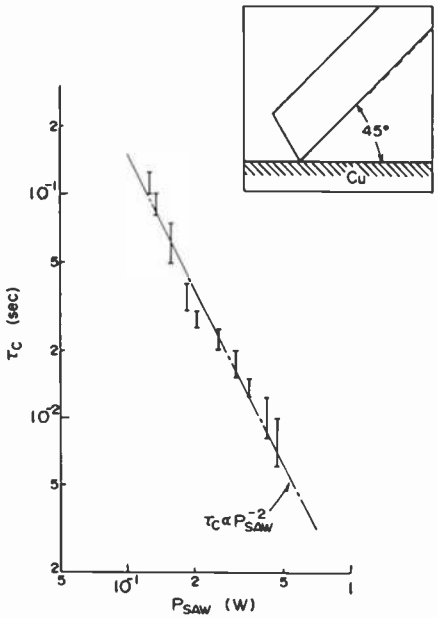

Fig. 17—τ_c versus P_{SAW} for Cu. Tip size 10 × 10 μm^2, stylus dead weight 0.2 g, and f is 19.62 MHz. Stylus axis made an angle of about 45° with the Cu-plate surface, as shown in the insert, so that sharp tip edge contacted the surface.

5. Conclusion

The operating principles of a new type of pickup and recording devices were demonstrated. Both devices have basically the same structure, a sharp-pointed stylus wherein surface acoustic waves (SAW) are generated from an interdigitated electrode (IDT) structure mounted on the stylus shank. These waves are focussed on the stylus tip. The SAW power concentration at the tip is the essential feature of operation and is achieved by a combination of three factors: the focussing action of the IDT electrode structure, the geometry of the stylus tip, and SAW confinement to a layer approximately one wavelength deep along the propagating surface. The difference between pickup and recording modes is in the level of applied power. Power higher than a critical value is required for recording; power for readout operation is much lower than this critical value.

In the pickup mode the surface acoustic wave incident to the

stylus tip is partially reflected or absorbed to a degree depending upon whether or not the tip is free, or whether it contacts another material. This other material may have purposely recorded information on its surface or it may be a film of unknown depth that one wishes to probe. In either case, the SAW reflected back to the IDT electrode contains information about acoustic conditions at the stylus tip. These reflected waves change the electrical input impedance of the IDT and provide an easily measurable signal in the associated attached circuitry. In the recording mode, on the other hand, high SAW power at the stylus tip deforms the material surfaces touching the tip. The recording mechanism is a combination of thermal and mechanical processes.

Experiments made with single-crystal quartz styli are in good agreement with well established SAW theory. Device operation was studied in terms of the stylus characteristics: IDT structure, operating frequency, radiation resistance, reflection effects, and conditions at the stylus tip. The information from these fundamental studies should be useful for determining the optimum conditions for device operation, and for establishing design principles for practical devices.

The feasibility of using the SAW stylus for recording and subsequent playback at audio frequencies was demonstrated in a cooperative experiment with RCA Engineering Laboratories, Tokyo, Japan. Symphony music was recorded on a blank vinyl disc using a SAW stylus and then played back with reasonable performance using another SAW stylus having the same structure used in the present work.

Acknowledgments

The authors express their appreciation to Messrs. K. Fukazawa and A. Yamada of RCA Engineering Laboratories, Tokyo, Japan, for providing their results on recording and playback experiments at audio frequencies, and for helpful discussions. Thanks are due to Dr. R. Shahbender of the RCA David Sarnoff Research Center, Princeton, for his critical reading of the manuscript and his many suggestions.

Appendix A. Radiation Resistance

The theory of SAW interdigital transducer (IDT) has been presented by Smith et al.,[4] and is convenient for the analysis and the design of IDT electrodes. The IDT they analyzed is rectangular-shaped

with straight fingers; ours is fan-shaped with curved fingers. If the finger curvature is not large, no essential differences in physical behavior will be introduced. To take the IDT geometry difference into account, a slight modification is required in the equation parameters. This was briefly discussed in the main text and will be treated again in the following analysis. Unless specified differently, our notations are the same as those used in Smith's work.

A circuit schematic of the IDT system on the stylus surface is illustrated in Fig. 18. The SAW power is launched from one side (port 1) of the IDT toward the stylus tip (port 0) through the transmission medium (T.M.). At the tip the SAW power is dissipated by mode conversion to bulk waves, and by transfer to the material in contact with the tip. This total power dissipation is described by the load resistance R_L terminating the port 0. The SAW power radiated from the other side (port 2) of the IDT is absorbed, and no power is reflected back. This behavior is described by a characteristic impedance R_o terminating port 2. The three-port expression of the IDT admittance is given in the theory.[4] The SAW propagation between ports 0 and 1 is expressed in the following form:

$$\begin{bmatrix} V_1 \\ I_o \end{bmatrix} = \begin{bmatrix} \cos\theta' & jR_o\sin\theta' \\ jG_o\sin\theta' & \cos\theta' \end{bmatrix} \begin{bmatrix} V_1 \\ I_1 \end{bmatrix}, \qquad \text{[A-1]}$$

with $\theta' = 2\pi l'/\lambda$ and $G_o = 1/R_o$. The voltage V and the current I are the electrically equivalent stress and particle velocity associated with a SAW, respectively. The quantity λ is the SAW wavelength, and l' is the length of the transmission medium, that is, the distance between one end (port 1) of the IDT and the tip. The wavelength λ in the present geometry may not be a constant near the tip, since the wave is not sinusoidal but rather a Bessel function type. Fur-

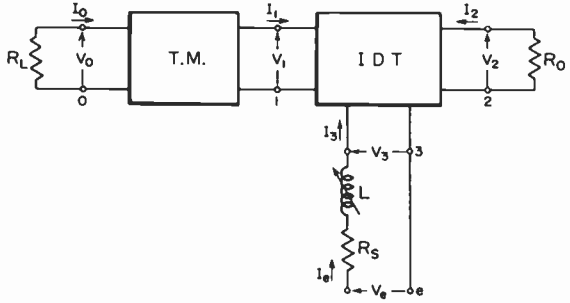

Fig. 18—Schematic circuit diagram of a stylus.

thermore, near the tip, the stylus width becomes narrow resulting in a decrease in SAW velocity.[11] These effects appear in the region close to the tip and are taken into account by slightly adjusting the value of l' from the actual physical length.

The component incident on or reflected back from the tip is obtained by terminating port 0 or 1 with the characteristic impedance R_o. These components are

$$\begin{bmatrix} V_o \\ I_o \end{bmatrix}_{\text{in}} = \exp(-j\theta') \begin{bmatrix} V_1 \\ I_1 \end{bmatrix}_{\text{in}} \qquad \text{[A-2]}$$

for the incident wave, and

$$\begin{bmatrix} V_1 \\ I_1 \end{bmatrix}_{\text{ref}} = \exp(-j\theta') \begin{bmatrix} V_o \\ I_o \end{bmatrix}_{\text{ref}} \qquad \text{[A-3]}$$

for the reflected wave.

The reflectance r, defined by the ratio of the reflected component $I_{o,ref}$ to the incident component $I_{o,in}$ of the current at the tip, is given by

$$r = (R_o - R_L)/(R_o + R_L). \qquad \text{[A-4]}$$

If all of the incident SAW power is dissipated at the tip and no SAW power reflected back to the IDT, R_L becomes R_o, and r becomes 0. When all of the incident power is reflected back as a SAW and the tip is free, the stress V_o at the tip is zero, i.e., $R_o = 0$ and $r = 1$. In the present case, however, a part of the incident power is dissipated into a bulk wave mode that is reflected at the load-free tip, and r is considered to have a value between 0 and 1.

The impedance at port 1 is given by

$$Z_1 = V_1/I_1 = R_o[1 - r\exp(-2j\theta')]/[1 + r\exp(-2j\theta')]. \qquad \text{[A-5]}$$

Terminating port 1 with Z_1 and port 2 with R_o in the three port network of an IDT, the expressions are obtained for the impedance Z_3 at port 3 and for Z_e at the circuit entrance port e. For the quartz styli used, $C_T \sim 2.5$ pF, $\hat{R}_a \sim 50\ \Omega$, and the center frequency was near 20 MHz. The capacitive component $1/\omega C_T$ is about 3 kΩ, a value much larger than the acoustic component in the impedance Z_3. Straightforward calculation leads to the following results:

$$
\begin{aligned}
Z_e &= R_s + j\omega L + Z_3, \\
Z_3 &= 1/j\omega C_T + j\hat{R}_a (\sin 2x\text{-}2x)/2x^2 \\
&\quad + \hat{R}_a(\sin x/x)^2[1 + r\exp(-j\theta)], \\
x &= N\pi(f\text{-}f_o)/f_o, \\
\theta &= 2(\theta' + x) = (4l/N\lambda_o)x + \phi,
\end{aligned}
\qquad \text{[A-6]}
$$

and

$$\phi = 2\pi(2l'/\lambda_o - \text{integer}).$$

Here, $l\,(=l' + N\lambda_o/2)$ is the distance between the center of the IDT and the tip, N is the number of finger pairs in the IDT, λ_o is the acoustic wavelength corresponding to the IDT central driving frequency f_o, and θ is double the difference of the SAW phase at the tip and at the center of the IDT. For the coefficient of x in the expression for θ, the effect of the slight adjustment of l', mentioned before, is negligible in the analysis of the experimental results. For ϕ, however, a slight adjustment or experimental error in l' has an appreciable effect. Since the estimation of the effect is not so easy, the value of ϕ is rather arbitrarily adjusted around the value calculated using the measured length of l' or l.

To measure the radiation resistance, the imaginary part of Z_e is cancelled out by tuning the external inductor L. The real part of Z_e is then given by

$$
\begin{aligned}
R_e\, Z_e &= R_S + R_a, \\
R_a &= \hat{R}_a(\sin x/x)^2(1 + r\cos\theta).
\end{aligned}
\qquad \text{[A-7]}
$$

This latter equation is used for the analysis of the IDT radiation resistance R_a.

Appendix B. Impedance Changes Caused by Acoustic Loading at the Stylus Tip

When the tip is in contact with another material, the incident power is dissipated by transfer of power into the material as well as into bulk modes inside the stylus body. The load resistance R_L is thereby increased by ΔR_L, and the reflectance r is changed by Δr where

$$\Delta r = -2(1 + R_L/R_o)^{-2}(\Delta R_L/R_o). \qquad \text{[B-1]}$$

Power dissipation at the tip causes the amplitude of the reflected SAW to decrease. Thus $\Delta r < 0$. The amplitude decrease in the reflected wave, which interferes with the incident signal, results in a change ΔZ in the impedance Z_e wherein

$$\Delta Z = \Delta r \hat{R}_a (\sin x/x)^2 \exp(-j\theta). \quad [B\text{-}2]$$

In the above discussion, the acoustic loading at the tip was considered to be resistive. Depending on the nature of the acoustic loading, e.g., mass loading, the loading can be inductive or capacitive. Extension to these cases is straightforward.

Appendix C. Electric and Acoustic Powers

The voltages at ports 1 and 2 are

$$V_1 = -2N(\sin x/x)\exp(-jx)[1 - r\exp(-2j\theta')]V_3,$$
$$V_2 = 2N(\sin x/x)\exp(-jx)[1 + r\exp(-j\theta)]V_3.$$

V_3 is the voltage across the IDT electrodes and this corresponds to V_{IDT} in the text. Straightforward calculation leads to the following expressions for power at ports 1, 2, and 3:

$$P_1 = P_{SAW} = -(V_1^* I_1 + V_1 I_1^*)/2 \quad [C\text{-}1]$$
$$= [(1 - r^2)/2(1 + r\cos\theta)]P_3,$$
$$P_2 = P_{SAW'} = -(V_2^* I_2 + V_2 I_2^*)/2$$
$$= [(1 + 2r\cos\theta + r^2)/2(1 + r\cos\theta)]P_3, \quad [C\text{-}2]$$
$$P_3 = P_a = (V_3^* I_3 + V_3 I_3^*)/2 = (1/Z_3 + 1/Z_3^*)V_3^* V_3/2$$
$$= (\omega C_T)^2 \hat{R}_a (\sin x/x)^2 (1 + r\cos\theta) V_3^* V_3. \quad [C\text{-}3]$$

Here $\hat{R}_a = 8N^2/R_o(\omega C_T)^2$. P_3 is equal to the sum of P_1 and P_2. The conversion efficiency from the input power P_e at the circuit entrance port e to P_3 is given by

$$P_3/P_e = R_a/R_f,$$

where

$$R_a = \hat{R}_a (\sin x/x)^2(1 + r\cos\theta).$$

Substituting Eqs. [A-4] and [C-4] into Eq. [C-1], we obtain

$$P_1/P_e = (1 - r^2)\hat{R}_a(\sin x/x)^2/2R_f. \quad [C\text{-}5]$$

Eqs. [C-3], [C-4], and [C-5] correspond to Eqs. [9], [5], and [6] in the text, respectively. The factor 8 in Eq. [9] in the text is due to the definition of V_{IDT} in peak-to-peak value.

Appendix D. Effect of Stray Capacitance

The equivalent circuit of an IDT including a tuning inductor L is illustrated in Fig. 19. The imaginary part of the radiation impedance is small compared with the capacitive impedance of C_T and is neglected in the figure for simplicity. C_s and C_s' represent stray

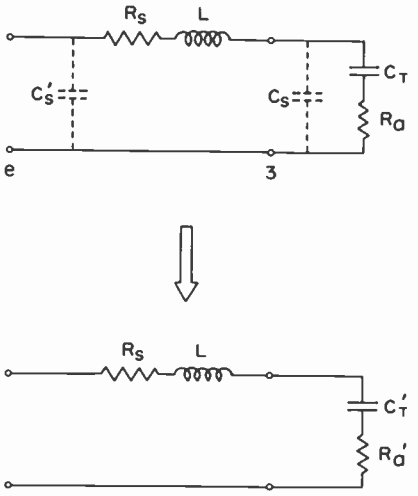

Fig. 19—Effect of stray capacitance on IDT capacitance and radiation resistance.

capacitances of the circuit, and are of the order of 1 pF. Since the shunt impedance of stray capacitance C_s' is much higher than the IDT impedance Z_e (= R_f under tuned condition) at port e, the effect of C_s' is negligibly small. The IDT impedance Z_3 at port 3 is almost capacitive and much higher than R_a. Therefore the effect of stray capacitance is not negligibly small.[1] The IDT capacitance C_T and the radiation resistance R_a are modified by C_s as follows:

$$C_T \rightarrow C_T' = C_T + C_s$$

$$R_a \rightarrow R_a' = R_a/(1 + C_s/C_T)^2.$$

These contributions of the stray capacitance C_s are cancelled out in Eq. [C-3] or Eq. [9], and the expression of P_a is also valid for the circuit including stray capacitance.

Appendix E. Effect of an Absorber on the Propagation Surface

If the propagation surface is partially covered with an absorber, the transmission medium becomes lossy. Eqs. [A-2] and [A-3] are assumed to be modified to

$$\begin{bmatrix} V_o \\ I_o \end{bmatrix}_{in} = \exp(-j\theta' - \alpha) \begin{bmatrix} V_1 \\ I_1 \end{bmatrix}_{in} \qquad [E\text{-}1]$$

and

$$\begin{bmatrix} V_1 \\ I_1 \end{bmatrix}_{\text{ref}} = \exp(-j\theta' - \alpha) \begin{bmatrix} V_o \\ I_o \end{bmatrix}_{\text{ref}}, \qquad \text{[E-2]}$$

respectively, to include the propagation loss due to the absorber. Here, $\exp(-\alpha)$ represents the attenuation of the SAW amplitude. The impedance at port 1 is then modified to

$$Z_1 = -V_1/I_1 = R_o[1 - r_a \exp(-2j\theta')]/[1 + r_a \exp(-2j\theta')], \qquad \text{[E-3]}$$

and

$$r_a = \exp(-2\alpha)r.$$

Since the tip is not covered with an absorber, the reflectance r at the tip remains the same. The reflectance appearing in the expression for the radiation impedance is the effective reflectance r_a, instead of the reflectance r at the tip.

Eqs. [E-1] and [E-2] indicate that the absorber is simply assumed to attenuate the SAW amplitude. The phase difference θ', hence θ, may also be affected by the SAW velocity change due to the mass loading effect of the absorber. This results in a shift of frequencies at the radiation resistance minima and maxima. Furthermore, the absorber may reflect the SAW back to the IDT, resulting in an interference pattern in the radiation resistance different from that due to the reflection at the tip. Observation of the radiation resistance of the styli, with or without an absorber, showed that the major effect of the absorber was to decrease the amplitude of the interference pattern in the frequency dependent radiation resistance. That is, the reflectance decreased from r ($=0.33$) to r_a ($=0.14$). However, little shift of the frequencies at the resistance minima and maxima was observed. These experimental results indicate that our assumption is plausible.

The SAW power radiated from port 1 is given by:

$$\begin{aligned} P_1 = P_{SAW} &= (V_1{}^*I_1 + V_1I_1{}^*)/2 \\ &= (1/Z_1 + 1/Z_1{}^*)V_1{}^*V_1/2 \\ &= [(1 - r_a{}^2)/R_o(1 - 2r_a \cos 2\theta' + r_a{}^2)]V_1{}^*V_1. \end{aligned} \qquad \text{[E-4]}$$

The SAW power reaching the tip is attenuated. The power at the tip, port 0, is expressed as

$$\begin{aligned} P_o &= (V_o{}^*I_o + V_oI_o{}^*)/2 = V_o{}^*V_o/R_L \\ &= [(1 + r)/R_o(1 - r)]V_o{}^*V_o. \end{aligned}$$

Using Eqs. [E-1] and [E-2], we can express V_o in terms of V_1. This results in the following expression for P_o:

$$P_o = e^{-2\alpha}[(1 - r^2)/R_o(1 - 2\, r_a \cos 2\theta' + r_a{}^2)]V_1{}^*V_1$$
$$= (r_a/r)[(1 - r^2)/(1 - r_a{}^2)]\, P_1. \qquad \text{[E-5]}$$

This equation corresponds to Eq. [10] in the text.

References:

[1] A. J. Slobodnik, Jr., *J. Appl. Phys.*, **43**, p. 2565 (1972).
[2] E. G. Lean, C. D. W. Wilkinson and P. F. Heidrich, the 8th Conf. on Solid State Devices, Tokyo, B-6-10 (1976).
[3] A. J. Slobodnik, Jr., and E. D. Conway, *Microwave Acoustic Handbook* (UASF Cambridge Res. Labs., Mass., 1970) Vol. 1, p. 58.
[4] W. R. Smith, H. M. Gerard, J. H. Collins, T. M. Reader, and H. J. Shaw, *IEEE Trans. Microwave Theory and Tech.*, **MTT-17**, p. 865 (1969).
[5] M. Toda and S. Osaka, *Trans. IECE Japan*, **E-60**, 237 (1977).
[6] D. A. Pinnow, *IEEE J. Quantum Electronics*, **QE-6**, p. 223 (1970).
[7] M. B. Schultz and J. H. Matsinger, *Appl. Phys. Lett.*, **20**, p. 367 (1972).
[8] R. V. Schmidt, *Appl. Phys. Lett.*, **17**, p. 369 (1970).
[9] Editorial Committee of Wireless Eng. Handbook, *Wireless Engineering Handbook* (OHM Co., Ltd. Tokyo, 1968) p. 2–20, in Japanese.
[10] F. S. Hickernell, *J. Appl. Phys.*, **44**, p. 1061 (1973).
[11] R. C. M. Li, H. L. Bertoni, and A. A. Oliver, *Electron. Lett.* **8**, p. 220 (1972).

Surface Acoustic Wave Stylus: Part 2—Relationship Between Rectangular and Fan-Shaped Interdigital Transducers

S. Tosima*

Abstract—In Part I, the operation of fan-shaped *interd*igital *t*ransducers (IDT) was analyzed using the established theory of operation for rectangular-shaped IDT having straight finger electrodes. Theory agreed with experiment better than expected. In this paper the theory is specifically modified to handle the fan-shaped case, and the reasons are sought for the success of the original theory despite the large difference in IDT geometries. The modified theory is applied to the quartz styli used in our experiments. The calculated results for the radiation resistance of these styli indicate that the modification arising from the geometrical difference is only a few percent, and thus negligible. The theory for a rectangular-shaped IDT is a good first-order approximation to a fan-shaped case, provided that the SAW amplitude and such physical parameters as acoustic characteristic impedance and electrode finger pair capacitance are properly normalized with respect to the distance from the stylus tip.

1. Introduction

The feasibility of applying surface acoustic waves (SAW) to pickup and record signals with a stylus have been reported in Part 1.[1] The stylus used in these experiments consisted of a plate with one end sharpened and having a fan-shaped interdigital transducer (IDT) fabricated on its shank. The IDT electrode fingers are curved to focus the SAW beam at the stylus tip. With this structure the input

* Present address: Corning Research, Inc., Machida City, Tokyo, 194–02, Japan.

power is effectively concentrated at the tip, an essential feature of the device.

In the analysis of the experimental results in Part 1, we used the established theory[2] for a rectangular-shaped IDT having straight electrode fingers. This theory explained the general features of the experimental results well despite our use of a fan-shaped IDT geometry. To corroborate these results, it is necessary to examine the validity of applying the rectangular theory to the fan-shaped IDT case.

The geometrical difference between a rectangular and a fan-shaped IDT affects the physical parameters involved in the theory of IDT operation. With a fan-shaped IDT, the SAW propagation direction toward the tip is distributed within the angle of the sharpened tip, and the width of the SAW beam varies along the propagation path. In addition, the SAW velocity V_{SAW} and the electromechanical coupling constant k^2 depend upon the propagation direction with respect to the crystal anisotropy when a single crystal is used for the stylus. However, the effect of crystal anisotropy can be made small by proper choice of stylus material, crystal cut, and stylus tip angle. This eliminates many complications. The anisotropy of V_{SAW} can be taken into account by shifting the center of curvature of each finger electrode from the tip position in the IDT design. The electromechanical coupling constant k^2 appears only in the parameter $\hat{R}_a$ which determines the magnitude of the IDT resistance R_a. An averaged value of the anisotropic k^2 over the propagation direction is taken as the k^2 value in the parameter $\hat{R}_a$.[1]

A crucial difference appears in such parameters as the electrical equivalent acoustic characteristic impedance R_o and the capacitance C_s of each electrode finger pair. These parameters depend upon the SAW beam width,[2] and this width changes as the dimensions of the IDT fingers change from about 4 mm to 1 mm.[1] In a SAW propagation region between the IDT and the tip, the beam width is further decreased to the tip width, which is a few, or a few tens of, a μm in size. Accordingly, the parameters are not constant and vary over a fairly wide range of values.

2. Three-Port Admittance Matrix of a Fan-Shaped Interdigital Transducer

Our calculation of the admittance matrix of a fan-shaped IDT is similar to that made by Smith et al.[2] for a rectangular-shaped IDT. They used two simplified configurations of the applied electric field, one perpendicular and one parallel to the acoustic propagation

vector, referring to these configurations as the "cross-field" and the "in-line" models, respectively. Results from these two models agree when the condition $[(4/\pi)k^2N]^2 << 1$ is valid,[2] where N is the number of finger pairs. For simplicity, we use the "cross-field" model, since the above condition is valid in most of our cases. Also, since the effect of crystal anisotropy is not serious, as previously mentioned, the anisotropy of the SAW velocity and the electro-mechanical coupling constant are ignored. This simplification does not affect the essential features of a fan-shaped IDT.

2.1 Equivalent Circuit Model for One IDT Section (Finger Pair)

The equivalent circuit of one section of a fan-shaped IDT composed of N periodic sections is shown in Fig. 1. The quantities e_n and i_n are the electrical equivalent force and particle velocity at the acoustic port n of the section (for details, see Ref. [2]). Following Ref. [2], the electrical equivalent acoustic characteristic impedance R_n at port n is expressed by

$$R_n = \frac{2\pi}{\omega_o C_n k^2}, \qquad [1]$$

where C_n is the equivalent finger pair capacitance at the port and ω_o is the angular resonant frequency of the IDT. Since the SAW beam width is proportional to the distance r_n from the origin of

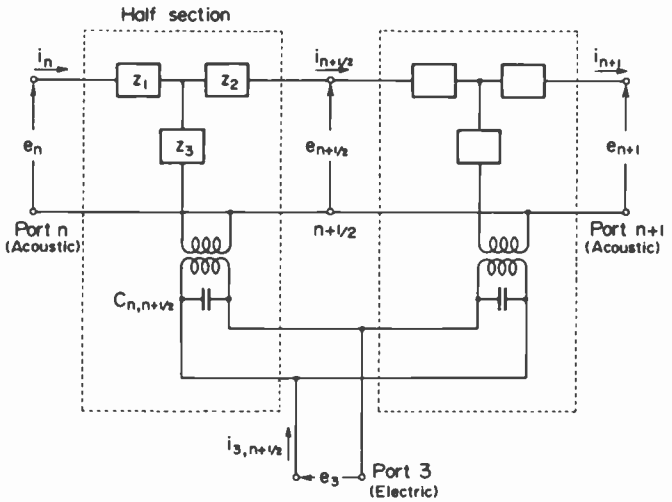

Fig. 1—Equivalent circuit for one IDT finger pair section.

coordinates at the center of curvature of the finger electrodes, C_n is also proportional to r_n, i.e.,

$$C_n = (r_n/r_o)C_s. \qquad [2]$$

If r_o is chosen to be the distance to the IDT center, C_s is the average finger pair capacitance. The quantity R_n is then inversely proportional to r_n and is given by

$$R_n = (r_o/r_n)R_o, \qquad [3]$$

where R_o is the acoustic characteristic impedance at the IDT center.

The SAW propagation equation between m-th and n-th acoustic ports is given by

$$\begin{bmatrix} e_n \\ i_n \end{bmatrix} = \begin{bmatrix} \sqrt{r_m/r_n}\cos(n-m)\theta & -jR_o\left(\dfrac{r_o}{\sqrt{r_m r_n}}\right)\sin(n-m)\theta \\ -jG_o\left(\dfrac{\sqrt{r_m r_n}}{r_o}\right)\sin(n-m)\theta & \sqrt{r_n/r_m}\cos(n-m)\theta \end{bmatrix} \begin{bmatrix} e_m \\ i_m \end{bmatrix} \qquad [4]$$

Here $G_o = 1/R_o$ and $\theta = 2\pi f/f_o$, where f is the actual operating frequency and f_o is the IDT center frequency. When either one of the acoustic ports is terminated with the corresponding characteristic impedance, R_n or R_m, the above equation describes the SAW propagation through the region between these two ports without reflection at the terminated port. The impedance Z_1, Z_2, Z_3 and the electrode capacitance $C_{n,n+1/2}$ of the half section between ports n and $n + 1/2$ (see Fig. 1) are then given by

$$\begin{aligned} Z_1 &= jR_o(r_o/\sqrt{r_n r_{n+1/2}})(1 - \sqrt{r_{n+1/2}/r_n}\cos\theta/2)\operatorname{cosec}\theta/2, \\ Z_2 &= jR_o(r_o/\sqrt{r_n r_{n+1/2}})(1 - \sqrt{r_n/r_{n+1/2}}\cos\theta/2)\operatorname{cosec}\theta/2, \\ Z_3 &= -jR_o(r_o/\sqrt{r_n r_{n+1/2}})\operatorname{cosec}\theta/2, \end{aligned} \qquad [5]$$

and

$$C_{n,n+1/2} = (C_s/2)(r_n + r_{n+1/2})/(2r_o).$$

Voltages and currents are normalized as follows:

$$\begin{aligned} E_n &= \sqrt{r_n/r_o}\, e_n, \\ I_n &= \sqrt{r_o/r_n}\, i_n, \\ E_3 &= e_3, \\ I_{3,n+1/2} &= i_{3,n+1/2}. \end{aligned} \qquad [6]$$

With these normalized quantities, and with reference to Fig. 1, we find the following equations for one section:

$$\begin{bmatrix} E_{n+1} \\ I_{n+1} \end{bmatrix} = [R] \begin{bmatrix} E_n \\ I_n \end{bmatrix} + \begin{bmatrix} d_1(n) \\ jG_o d_2(n) \end{bmatrix} E_3, \qquad [7]$$

or

$$\begin{bmatrix} E_n \\ I_n \end{bmatrix} = [R]^{-1} \begin{bmatrix} E_{n+1} \\ I_{n+1} \end{bmatrix} - \begin{bmatrix} f_1(n+1) \\ -jG_o f_2(n+1) \end{bmatrix} E_3, \qquad [8]$$

and

$$\begin{aligned} I_{3,n+1/2} = {} & j\omega C_{n+1/2} E_3 + 2jG_o k(n+1/2) \operatorname{cosec} \theta E_3 \\ & - jG_o \operatorname{cosec} \theta d_1(n) E_n + jG_o \operatorname{cosec} \theta f_1(n+1) E_{n+1}, \end{aligned} \qquad [9]$$

where

$$[R] = \begin{bmatrix} \cos\theta & -jR_o \sin\theta \\ -jG_o \sin\theta & \cos\theta \end{bmatrix}, \qquad [10]$$

$$d_1(n) = 2\sqrt{r_{n+1/2}/r_o} \cos\theta/2 - \sqrt{r_n/r_o} \cos\theta - \sqrt{r_{n+1}/r_o},$$

$$d_2(n) = \sqrt{r_n/r_o} \sin\theta - 2\sqrt{r_{n+1/2}/r_o} \sin\theta/2,$$

$$f_1(n+1) = 2\sqrt{r_{n+1/2}/r_o} \cos\theta/2 - \sqrt{r_{n+1}/r_o} \cos\theta - \sqrt{r_n/r_o},$$

$$f_2(n+1) = \sqrt{r_{n+1}/r_o} \sin\theta - 2\sqrt{r_{n+1/2}/r_o} \sin\theta/2,$$

$$k(n+1/2) = \sqrt{r_n/r_o}\, d_1(n) + \sqrt{r_{n+1}/r_o} f_1(n+1) + (\sqrt{r_n r_{n+1}} - r_{n+1/2})/r_o,$$

$$C_{n+1/2} = C_{n,n+1/2} + C_{n+1/2,n+1} = (r_{n+1/2}/r_o) C_s.$$

In cylindrical coordinates, convenient for analysis of the fan-shaped IDT, the wave is expressed in terms of a Bessel function. An asymptotic form of the function is a sinusoidal wave whose amplitude is inversely proportional to the square root of the distance r from the coordinate origin. In the rectangular-shaped IDT case, the wave is expressed in terms of a sinusoidal wave. It is then easily understood that the matrix $[R]$ reduces to that of a rectangular-shaped IDT if the SAW amplitude is normalized with the factor $\sqrt{r/r_o}$. This leads to the normalizations in Eq. [6].

2.2 Admittance Matrix for the Entire IDT

The three-port admittance matrix for the entire IDT is found by connecting N periodic sections acoustically in series and electrically

in parallel. Starting from $n = 1$ in Eq. [7] and applying the matrix $[R]$ N-times, we obtain

$$\begin{bmatrix} E_{N+1} \\ I_{N+1} \end{bmatrix} = [R]^N \begin{bmatrix} E_1 \\ I_1 \end{bmatrix} + \sum_{n=1}^{N} [R]^{N-n} \begin{bmatrix} d_1(n) \\ jG_o d_2(n) \end{bmatrix} E_3. \qquad [11]$$

The total IDT current I_3 is the sum of currents flowing into the N periodic sections:

$$\begin{aligned} I_3 = \sum_{n=1}^{N} I_{3,n+1/2} &= -jG_o D(N) \operatorname{cosec} N\theta \, E_1 \\ &+ jG_o F(N) \operatorname{cosec} N\theta \, E_{N+1} \\ &+ j[\omega C_{IDT} + G_o K(N) \operatorname{cosec} \theta] \, E_3, \end{aligned} \qquad [12]$$

where

$$D(N) = \sum_{\lambda=1}^{N} [\cos (N - \lambda)\theta d_1(\lambda) + \sin (N - \lambda)\theta d_2(\lambda)],$$

$$F(N) = \sum_{\lambda=1}^{N} [\cos \lambda\theta d_1(\lambda) - \sin \lambda\theta \, d_2(\lambda)],$$

$$\begin{aligned} K(N) = \sum_{n=1}^{N} &[2k(n + 1/2) \\ &+ \operatorname{cosec} N\theta\{f_1(n + 1) - d_1(n + 1)\} \\ &\{\sin N\theta D(n) - \sin n\theta D(N)\}], \end{aligned}$$

$$C_{IDT} = \sum_{n=1}^{N} C_{n+1/2} = NC_s.$$

Solving Eq. [11] with respect to I_1 and I_{N+1}, and using Eq. [12], we get the expression for the three-port admittance matrix $[Y]$ of the entire IDT. If the acoustic port $N + 1$ is referred to as port 2, and E_{N+1} and $-I_{N+1}$ are re-written as E_2 and I_2, respectively, we find

$$\begin{bmatrix} I_1 \\ I_2 \\ I_3 \end{bmatrix} = [Y] \begin{bmatrix} E_1 \\ E_2 \\ E_3 \end{bmatrix}. \qquad [13]$$

In calculating the elements of $[Y]$, the distance r_n of port n is expanded around the distance r_o of the IDT center. For example,

$$\sqrt{r_n/r_o} = [1 + (r_n - r_o)/r_o]^{1/2}$$

$$= 1 + \frac{1}{2}(\lambda_o/r_o)\left(\frac{r_n - r_o}{\lambda_o}\right) - \frac{1}{8}(\lambda_o/r_o)^2\left(\frac{r_n - r_o}{\lambda_o}\right)^2$$

$$+ \frac{1}{16}(\lambda_o/r_o)^3\left(\frac{r_n - r_o}{\lambda_o}\right)^3 - \ldots,$$

where λ_o is the periodic spacing of the IDT fingers.

For frequencies near the center frequency f_o, the matrix elements are approximately given by

$$\begin{aligned}
Y_{11} &= Y_{22} = -jG_o \cot 2x, \\
Y_{12} &= Y_{21} = jG_o \operatorname{cosec} 2x, \\
Y_{13} &= Y_{31} = jG_o(2N/x)(1 - a - b), \\
Y_{23} &= Y_{32} = -jG_o(2N/x)(1 - a - b), \\
Y_{33} &= j\omega C_{IDT} - j(\hat{G}_o/x)(1 + c),
\end{aligned} \qquad [14]$$

where

$$\begin{aligned}
x &= N\pi(f - f_o)/f_o, \\
\hat{G}_o &= 8N^2G_o = (4/\pi)k^2\omega_o C_s N^2, \\
a &= \frac{1}{2}\Delta^2[1 + 2(\cot x - 1/x)/x] + 0(\Delta^4), \\
b &= \Delta[1 - \tan x/x] + 0\,(\Delta^3), \\
c &= \Delta^2(1/x)^2[1 - \tan x/x] + 0\,(\Delta^4), \\
\Delta &= N\lambda_o/(4r_o).
\end{aligned}$$

When r_o approaches infinity, the geometry of the fan-shaped IDT reduces to that of the rectangular-shaped IDT and the matrix elements reduce to those of Smith's theory.[3]

3. Transducer Electrical Input Admittance

A circuit schematic of the SAW stylus is illustrated in Fig. 18 of Part 1. The SAW power launched from one side (port 1) of the IDT propagates toward the stylus tip (port 0) through the transmission medium (T.M.). At the stylus tip, some of the SAW power is dissipated by mode conversion to bulk waves and some by transfer to whatever material might be in contact with the tip. This total power dissipation is described by the normalized load resistance R_L terminating port 0. The SAW power launched from the other side (port 2) is totally absorbed by an absorber placed on the stylus surface. This power absorption is represented by the normalized characteristic impedance R_o terminating port 2.

The SAW propagation in the transmission medium is expressed in normalized form

$$\begin{bmatrix} E_o \\ I_o \end{bmatrix} = \begin{bmatrix} \cos\theta' & jR_o \sin\theta' \\ jG_o \sin\theta' & \cos\theta' \end{bmatrix} \begin{bmatrix} E_1 \\ I_1 \end{bmatrix}, \quad [15]$$

with $\theta' = 2\pi l'/\lambda$, where λ is the SAW wavelength and l' the length of the transmission medium. The SAW reflection at the tip is expressed in terms of the reflectance r, which is defined by[1]

$$r = (R_o - R_L)/(R_o + R_L). \quad [16]$$

The IDT input admittance Y_3 at port 3 is obtained by using the expression for the admittance matrix elements with Eqs. [15] and [16]. Straight-forward calculation leads to the following expression for Y_3:

$$\begin{aligned} Y_3 = I_3/E_3 &= j\omega C_{IDT} \\ &+ \hat{G}_a[(\sin x/x)^2 + \Delta^2 f(x) + 0(\Delta^4)]x[1 + r\exp[-j(\Theta - \alpha)]] \\ &+ j\hat{G}_a[(\sin 2x - 2x)/2x^2 - \Delta^2 g(x) + 0(\Delta^4)], \end{aligned} \quad [17]$$

where

$$\begin{aligned} f(x) &= \cos 2x/x^2 - 2\sin 2x/x^3 + 3(1 - \cos 2x)/2x^4, \\ g(x) &= \sin 2x/x^2 + (1 + 2\cos 2x)/x^3 - 3\sin 2x/2x^4, \\ \alpha &= 2\tan^{-1}[\Delta(\cot x - 1/x)/\{1 - \Delta^2(1/2 + (\cot x - 1/x)/x\})], \\ \Theta &= 4\pi l/\lambda = (4l/N\lambda_o)x + \varphi. \end{aligned}$$

Here, l is the distance between the IDT center and the stylus tip.

4. Applications and Conclusions

The radiation resistance R_a was measured for experimental quartz SAW styli.[1] For these styli, $r_o = 2.8$ mm, $\lambda_o = 0.16$ mm, and $N = 20$. The value of the parameter Δ in Eqs. [14] and [17] is then 0.29. The quantity Δ^4 is about 0.7%, and the fourth order term $0(\Delta^4)$ is negligibly small. Since $[(4/\pi)k^2N]^2 << 1$ and $N >> 1$, the radiation resistance R_a can be found using Eq. [17] as follows.

$$\begin{aligned} R_a &= R_e\,(1/Y_3) \\ &\approx \hat{R}_a[(\sin x/x)^2 + \Delta^2 f(x)][1 + r\cos\Theta_{eff}], \end{aligned} \quad [18]$$

where

$$\hat{R}_a = \hat{G}_a/(\omega C_{IDT})^2 = (4/\pi)k^2/(\omega_o C_s)$$

and

$$\Theta_{eff} = \Theta - \alpha.$$

The resistance $R_a/\hat{R}_a$ for $r = 0$ was calculated and the results are illustrated in Fig. 2. The correction term $\Delta^2 f(x)$ is very small and is only about -0.027 at the center frequency ($x = 0$).

The phase correction α is shown in Fig. 3 where it is seen to change linearly in the frequency region near the center frequency where the applitude of the oscillatory behavior in the radiation resistance is large. The term α is therefore expanded around $x = 0$, and Θ_{eff} is expressed as follows:

$$\Theta_{eff} \approx [(4l/N\lambda_o) + 2\Delta/3]x + \psi$$
$$= (4l_{eff}/N\lambda_o)x + \psi.$$

Since the position of the stylus tip is close to the coordinate origin ($l \approx r_o$), l_{eff} is found to be

$$l_{eff}/l \approx 1 + 2\Delta^2/3$$
$$\approx 1.05.$$

The distance between the IDT center and the tip is effectively about 5% longer than the physical length l.

The results for the radiation resistance indicate that the rectangular-shaped IDT theory[2] is a good first-order approximation to the fan-shaped IDT case, provided that the SAW amplitude and the electrical equivalent acoustic characteristic impedance R_o and the electrode finger pair capacitance C_s are interpreted as the properly

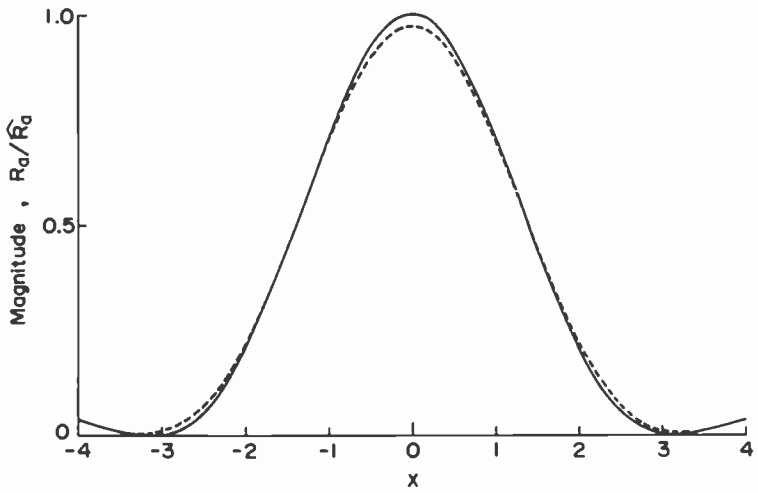

Fig. 2—Plot of the radiation resistance $R_a/\hat{R}_a$. The solid curve represents $(\sin x/x)^2$ for a rectangular-shaped IDT, and the dotted curve, $(\sin x/x)^2 + \Delta^2 f(x)$ for a fan-shaped IDT.

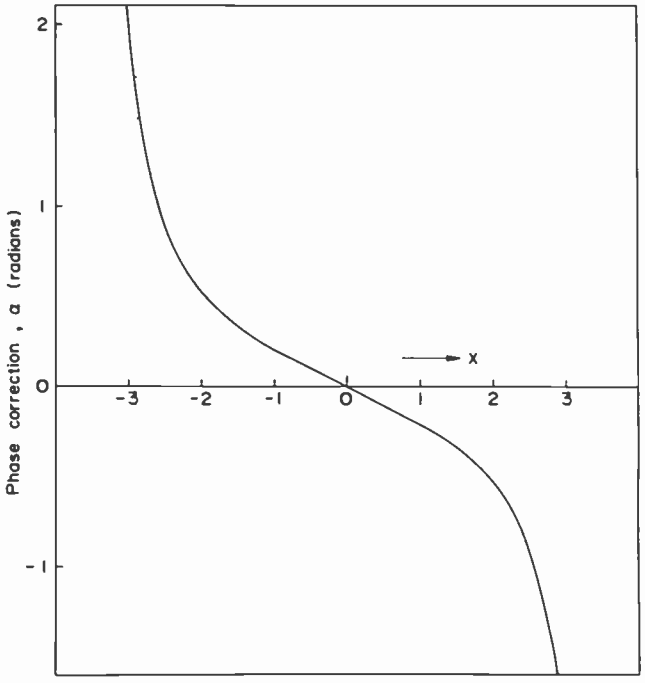

Fig. 3—Plot of the phase correction term α.

normalized ones, either with respect to SAW beam width or with respect to distance from the stylus tip.

Acknowledgment

The author would like to express his appreciation to Mr. E. O. Johnson, and to Dr. R. Shahbender of the RCA David Sarnoff Research Center, Princeton, NJ, for their critical reading of the manuscript and helpful suggestions.

References:

[1] S. Tosima, M. Nishikawa, T. Iwasa, and E. O. Johnson, *RCA Rev.*, **44**, p. 430, Sept. 1983 (this issue).
[2] W. R. Smith, H. M. Gerad, J. H. Collins, T. M. Reader, and H. J. Shaw, *IEEE Trans. Microwave Theory and Tech.*, **MTT-17**, p. 865 (1969).

Surface Acoustic Wave Stylus: Part 3—Optimum Tip Shape for Pickup Devices

S. Tosima* and M. Nishikawa*

Abstract—To find the tip shape of a surface acoustic wave (SAW) stylus for optimum pickup device operation, the radiation resistance was studied for various tip shapes acoustically loaded and unloaded. The major face of the stylus containing the IDT had one end sharpened at an angle of 60°. A minor face of the tip was sharpened at a tip angle ϕ like the bow of a boat as viewed from the side. The acoustic loading effect on the radiation resistance appeared as changes in amplitude and phase. The results indicate that stylus design for optimum operation occurs at a tip angles ϕ of about 55° and 75° where the resistance is most effectively modulated by acoustic loading. While a tip angle ϕ of 45° showed the largest amplitude of reflected SAW (about 60% of the incident SAW amplitude), the radiation resistance modulation due to loading modulation was of reduced effectiveness.

1. Introduction

It has been demonstrated that a surface acoustic wave (SAW) stylus can be used as a signal pickup device.[1] In the device, the reflected SAW carries signal information in terms of acoustic loading at the stylus tip. The reflected SAW signal picked up at the interdigital transducer (IDT), fabricated on the stylus shank, interferes with the incident signal and modulates the transducer impedance. The acoustic loading information at the tip is thus detected as an IDT impedance change.

The incident SAW focused at the load-free tip is converted into

* Present address: Corning Research, Inc., Machida City, Tokyo 194-02, Japan.

reflected SAW and bulk waves. If the tip is loaded by contact with a material, the incident SAW is partially converted to wave modes that are transferred into the material in addition to the reflected modes. These mode conversions depend upon boundary conditions at the tip, such as tip shape and acoustic loading. Since the mode effectively picked up by the IDT is the reflected SAW, the pickup device function seems best served with a stylus having a large SAW reflectance at the tip.

Acoustic loading effects on IDT radiation resistance have been studied in detail using a quartz stylus and were reported in Part 1.[1] The present paper describes the effect of changes in tip geometry on the radiation resistance and acoustic loading. The purpose is to determine optimal stylus design. For our studies, single-crystal quartz was used as the stylus material, since it can be conveniently cut and polished into various tip shapes and since its acoustic and piezoelectric properties are well known. The results obtained for the quartz styli are useful for the design of styli made of other materials, such as sapphire or diamond coated with a piezoelectric thin film.

2. Experimental Arrangement

Experimental samples were Y-cut quartz plates, typically 1.5-cm long along the X-axis, 5-mm wide, and 1-mm thick. One end of the major face of each plate was sharpened to an angle of 60° to make the sharpened tip. The tip was further sharpened in another plane to an angle ϕ, giving it a form like that of the bow of a boat when viewed from the side. The size of the stylus tip is then $a \times b$ where a is the width along the Z-axis and b the length along the Y-axis. These widths were measured with a microscope having a scale. The possible error is about 2 μm. A fan-shaped IDT was deposited near the tip on the flat major surface of the stylus plate. The periodicity λ_0 of the IDT is 160 μm, and the number N of electrode finger pairs is 20. The distance l between the tip and the IDT center is 2.76 mm. The SAW power radiated from the IDT in a direction opposite to that of the tip was absorbed with a piece of Scotch tape stuck to the stylus surface behind the IDT. The structure of the stylus described here is the same as that used in previous work and illustrated in Part 1.[1]

The minor angle ϕ was changed by successively polishing the stylus tip into a progressively sharper shape. This procedure avoids the variability in results that would be caused by using different samples; SAW reflectance is particularly dependent on the posi-

tioning of the IDT on the stylus shank. Errors in the IDT position cause a deviation of the focussing point of the SAW power from the tip.

The IDT driving power was applied to the IDT electrodes through a tuning inductor.

2. Radiation Resistance

The resistance R_f of the IDT for various tip angles ϕ was measured as a function of the driving frequency f when the tip was free from externally applied acoustic loading. Typical examples of the results are shown in Figs. 1a and 1b. The origins of the vertical coordinate for each angle ϕ is also shown in the figures. The bottom curve in Fig. 1a (ϕ = 90° (absorb.)) represents the resistance for the stylus

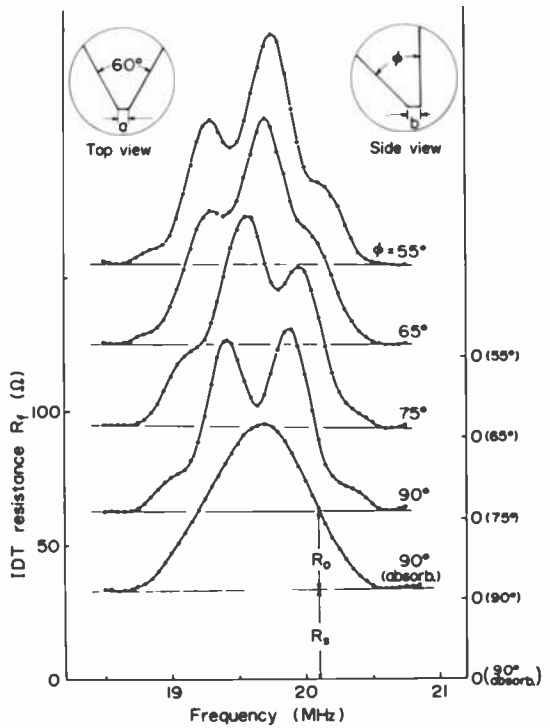

Fig. 1a—Frequency dependence of IDT resistance R_f for tip angles ϕ = 55°, 65°, 75°, 90°, and 90° with an absorber around the tip (stylus sample I with tip size 30 × 30μm^2). Origin of vertical coordinate for each tip angle ϕ shown on right-hand side. Inserts are top and side views of the stylus tip.

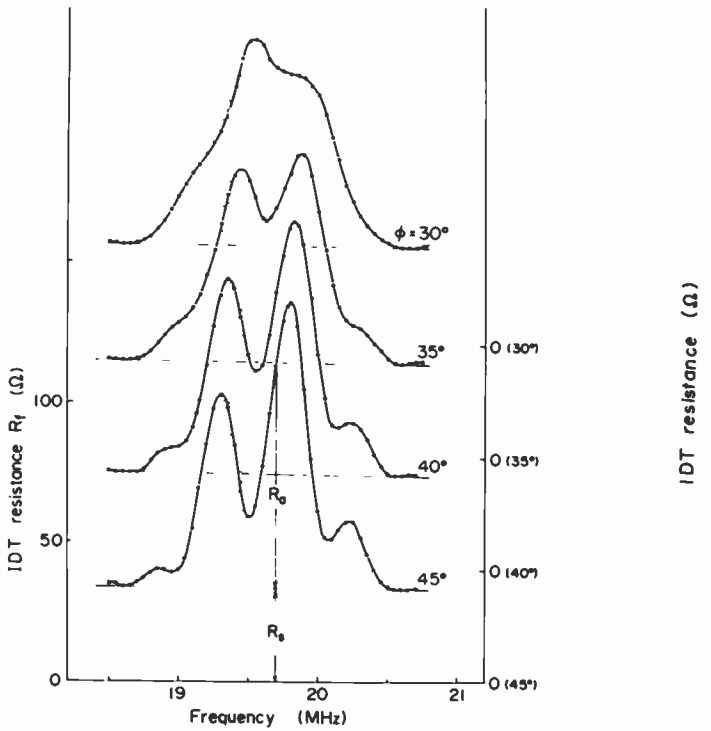

Fig. 1b—Same as Fig. 1a, but for tip angles ϕ = 30°, 35°, 40°, and 45°.

having an absorber around its tip to prevent acoustic power from being reflected back to the IDT. As expected for this case, the oscillatory behavior in the resistance does not appear. The other curves show oscillatory behavior that changes as the tip angle ϕ is changed.

The IDT radiation resistance R_a can be obtained by subtracting the circuit series resistance R_s.[1] The radiation resistance $R_o = R_a$ (o) (see Part 1) for the stylus whose tip is covered with the absorber has the $(\sin x/x)^2$-type frequency dependence[2] shown in Fig. 1a. If the SAW power loss due to the mode conversions at the tip is expressed in terms of an acoustic impedance Z and the acoustic characteristic impedance of quartz by $Z_o = R_o$ (see Part 1[1]), the SAW reflectance $r\exp(j\alpha)$ is, in general, a complex quantity and is given by

$$r \exp(j\alpha) = (Z_o - Z)/(Z_o + Z), \quad [1]$$

where α is a phase angle to be discussed later. The radiation resistance is then given by[1]

$$R_a = R_o (1 - r \cos\theta), \quad [2]$$

where

$$\theta = 4\pi l/\lambda + \alpha = (4\pi l/U)(f - f_o) + \psi,$$

and

$$\psi = 2\pi(2l/\lambda_o - \text{integer}) + \alpha.$$

Here, $l = 2.76$ mm is the distance between the IDT center and the tip, λ is the SAW wavelength along the X-axis, $f_o = 19.7$ MHz is the IDT center frequency, and $U = 3.16 \times 10^5$ cm/sec is the SAW propagation speed along the X-axis. The value of $4\pi l/U$ that gives the best fit to the observed values is $1.1 \sim 1.2 \times 10^{-5}$ sec. The second term in the parenthesis of Eq. [2] describes the oscillatory behavior of the radiation resistance. Eqs. [1] and [2] are an extension of Eqs. (A-4) and (1) in Part I,[1] respectively, and include the phase angle α of the reflectance. The term α is introduced to represent properly the effect of the acoustic loading at the tip on the radiation resistance. The acoustic loading effect may not be simply that of modifying the SAW power loss due to transferring the power into a material in contact, but also of modifying the acoustic properties of the tip, for example, by mass loading. Accordingly, the acoustic impedance Z at the tip can have a capacitive or an inductive component in addition to a resistive component. The acoustic loading effect in general affects both the reflectance amplitude r and the phase constant ψ. The latter is affected by way of α.

The reflectance amplitude r and the phase constant ψ are obtained from

$$r\cos\theta = R_a/R_o - 1 \qquad [3]$$

by substituting the observed values of R_a and R_o into this equation. Fig. 2 shows examples of the values of R_a and $R_a/R_o - 1$ as a function of frequency f. As expected, the $R_a/R_o - 1$ versus f plots show sinusoidal frequency dependence with a period, an amplitude r, and a phase constant ψ. The solid curve in the $R_a/R_o - 1$ versus f plot for $\phi = 85°$ is $r\cos\theta$ estimated with $4\pi l/U = 1.12 \times 10^{-5}$ sec, $r = 0.35$, and $\psi = 2.92$ radians. The value of $4\pi l/U$ corresponds to the observed value of 0.56 MHz for the period. These values gave good agreement of $r\cos\theta$ with the observed values of $R_a/R_o - 1$. For $\phi = 40°$, the values $4\pi l/U = 1.14 \times 10^{-5}$ sec, $r = 0.46$, and $\psi = -1.83$ radians gave the best fit of $r\cos\theta$ with the observed values. The solid curves in the R_a versus f plots were obtained by smoothly connecting the values of R_a calculated by using Eq. [2] with the best-fit values of r and ψ and with the observed values of R_o. As expected, the tip-shape dependence appeared in the oscillatory be-

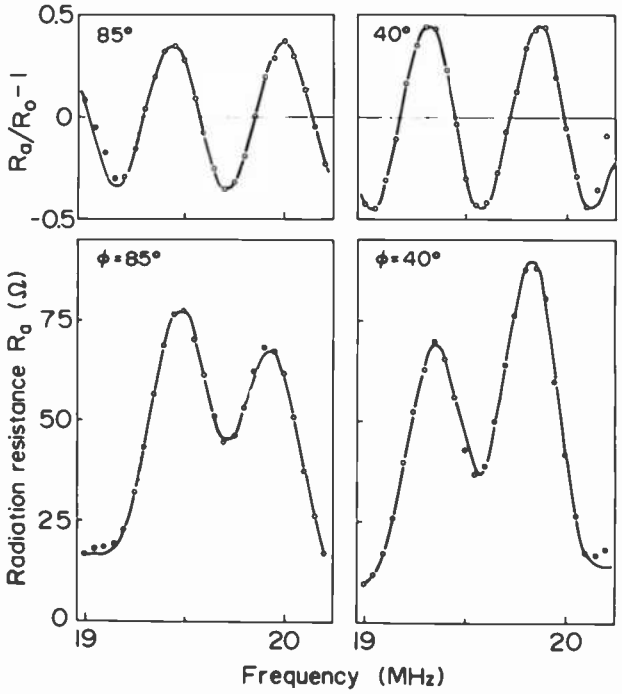

Fig. 2—Typical examples of radiation resistance R_a and oscillatory behavior of R_a normalized with R_o. Stylus sample I.

havior, $r\cos\theta$, of the radiation resistance R_a, especially in r and ψ.

The values of r and ψ thus obtained for each tip angle ϕ are shown in Fig. 3. The phase ψ decreases from that at $\phi = 90°$ as the tip is sharpened (i.e., the tip angle ϕ is decreased). The SAW power is distributed within a SAW wavelength of the material surface. Thus, the distance l which appeared in Eq. [2] effectively decreases as the tip is sharpened. Since the phase ψ is sensitive to distance, a slight decrease can cause an appreciable decrease in ψ. The assumption that the average depth of the SAW power is about one half a wavelength seems to explain the observed dependence of the phase ψ on the tip angle ϕ. For a detailed analysis, dependence of phase angle ϕ on tip shape is required. The reflectance amplitude r is minimum at about 0.2 around a tip angle ϕ of 70°, and is maximum at about 0.6 around ϕ of 45°.

4. Acoustic Loading Effect

To find optimum conditions for pickup operation, the effect of acoustic loading at a tip was studied. The IDT resistance R_f was

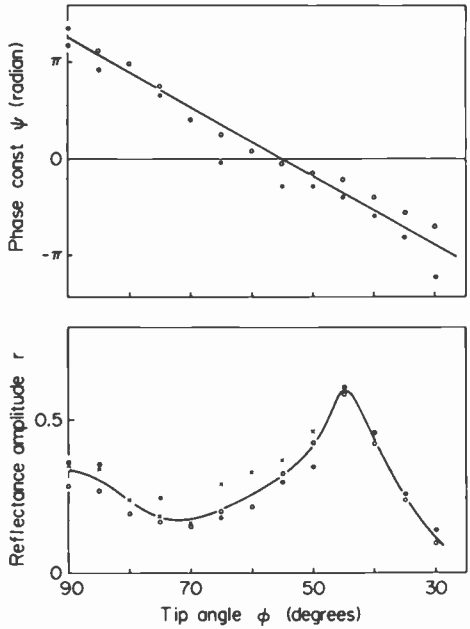

Fig. 3—Dependence of reflectance amplitude r and phase constant ψ upon tip angle ϕ: • are for sample I (tip size 30 × 30 μm^2); ○ for sample II (30 × 30 μm^2); and × for sample III (20 × 16 μm^2).

measured for a tip in contact with a Cu plate (5 × 5 × 1 mm^3). The Cu plate was placed on a glass plate and the tip was brought into contact with the Cu plate with a contacting force of about 1 gram. When the tip was brought close to the Cu plate, the IDT resistance R_f changed slightly possibly due to changes in circuit stray capacitance. The resistance changes were within a few %. These changes were much less than the resistance changes that occurred when the tip was brought into contact with the plate.

Typical examples of the results for R_a and $R_a/R_o - 1$ are shown in Fig. 4 for both acoustically loaded and the load-free tips. In this section, the load-free tips are defined as the ones brought close to the Cu plate. The dotted and solid curves were obtained in a fashion similar to that described in the preceeding section.

From the $R_a/R_o - 1$ versus f plots, best-fit values of the reflectance amplitude r and the phase constant ψ were obtained for each acoustic loading condition. The changes $\Delta r = r_{load} - r_{free}$ and $\Delta\psi = \psi_{load} - \psi_{free}$ due to the acoustic loading at the tip were estimated. The results are shown in Fig. 5. The acoustic loading effect on r is large at a tip angle ϕ around 75° and 55° and small at angles around

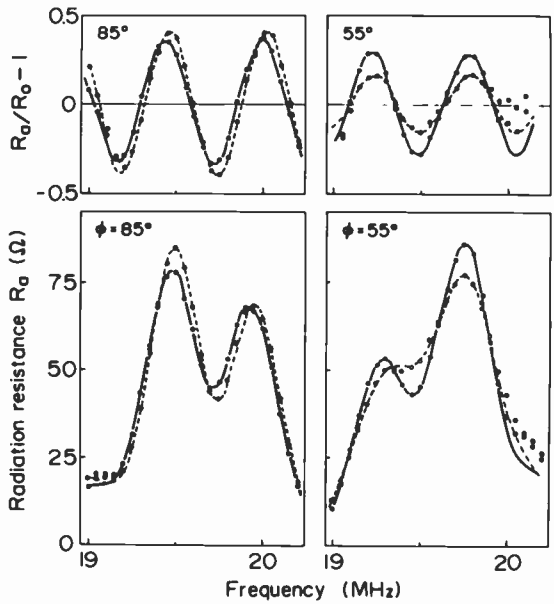

Fig. 4—Typical examples of R_a and $R_a/R_o - 1$ for two conditions of acoustic loading at tip (sample I): solid line is for load-free tip and dotted line for acoustically loaded tip.

67° and 43°. The effect is rather small at a tip angle of 45° where r is maximum at about 0.6. This means that the pickup device function is not necessarily larger for larger amplitudes of the reflected SAW. The acoustic loading affect on the phase ψ is on the order of $\pm 0.1\pi$ radian and is large in the vicinity of the tip angle $\phi = 90°$, or 65°, as shown in Fig. 5. No essential difference appeared in Δr and $\Delta\psi$, with r_{free} and ψ_{free} measured when the stylus tip was pulled away from the Cu plate.

5. Discussion and Conclusions

The frequency dependence of the radiation resistance shows oscillatory behavior as a result of interference between incident and reflected SAW. The reflected wave carries loading information picked up at the stylus tip. To find the stylus design for optimum pickup device operation, the oscillatory behavior and the effect of acoustic loading at the stylus tip upon radiation resistance were studied for various tip shapes. The tip shape was changed by gradual sharpening of the tip at an angle ϕ into a form like that of the bow of a boat when viewed from the side. Several optimum tip

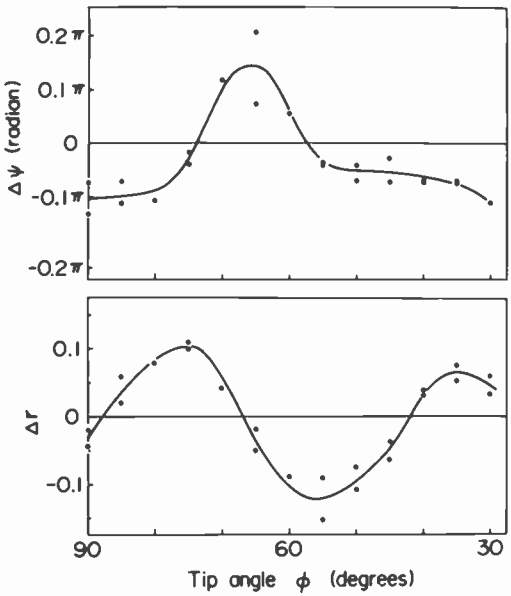

Fig. 5—Acoustic loading effect on reflectance amplitude r and phase constant ψ: solid dots are for sample I (30 × 30 μm^2) and circles are for sample II (30 × 30 μm^2).

angles for SAW reflection and acoustic loading at the tip were found. It is to be noted that the tip angle for optimum pickup operation is not necessarily the same as that for the largest SAW reflectance.

For practical device applications, it would be convenient to choose a tip angle, such as 75° or 55°, where $|\Delta r|$ is large but $|\Delta\psi|$ is small. At these tip angles, the acoustic loading effect on R_a appears at frequencies in the vicinity of the maxima and minima of R_a. Since the value of R_a is constant with frequency at these frequencies, a slight fluctuation of the IDT operating frequency will cause very little fluctuation of R_a. On the other hand, if the tip shape is chosen at an angle ϕ such as 67°, where $|\Delta r|$ is small and $|\Delta\phi|$ is large, the acoustic loading effect on R_a appears at the frequencies where the slope of the R_a versus f plot is steep. Under these conditions, fluctuation of the operating frequency f will cause relatively large changes in the radiation resistance R_a.

Acknowledgment

The authors wish to express their appreciation to Mr. E. O. Johnson for his continuous encouragement, helpful discussions, and critical

reading of the manuscript; and to Dr. R. Shahbender of RCA David Sarnoff Research Center, Princeton, NJ, for his critical reading of the manuscript and helpful suggestions.

References:

[1] S. Tosima, M. Nishikawa, T. Iwasa, and E. O. Johnson, *RCA Rev.*, **44**, p. 430, Sept. 1983 (this issue).
[2] W. R. Smith, H. M. Gerard, J. H. Collins, T. M. Reader, and H. J. Shaw, *IEEE Trans. Microwave Theory and Tech.*, **MTT-17**, p. 865 (1969).

Surface Acoustic Wave Stylus: Part 4—Pyramid-Shaped Surface Acoustic Wave Transducer for Signal Recording Cutterheads

S. Tosima* and M. Nishikawa*

Abstract—A new developmental type of cutterhead was demonstrated using surface acoustic waves (SAW) for impressing topographic signals into a recording medium. The waves are generated at modest power levels from fan-shaped interdigital transducers (IDT) located on the sloping side surfaces of a triangular pyramid made of $LiNbO_3$ and driven at an rf frequency of 7.2 MHz. The waves are concentrated at high power density at the apex of the pyramid where a cutting stylus would be attached. The 1000 Å observed mechanical displacement of the apex seems adequately large for practical recording applications.

1. Introduction

A stylus for mechanically impressing topographic signals into a recording medium is composed of a cutting stylus and a transducer driven by electric signals.[1] If the transducer is operated in an acoustic bulk-mode of mechanical oscillation, frequency response is limited by transducer dimensions; the dimensions must be small for high-frequency operation. To produce adequately large cutterhead motion amplitude at high frequencies, high power must be fed into the small volume of the transducer. The resulting high-power density causes undesirable heat generation and can cause electrical breakdown. These limit recording performance. To record video signals in real time, stringent requirements for frequency response and motion amplitude have to be satisfied simultaneously.

* Present address: Corning Research Inc., Machida City, Tokyo 194-02, Japan

One solution is to use a transducer operating in the surface acoustic wave (SAW) mode instead of the more conventional bulk-mode. In a SAW-mode transducer, a fan-shaped interdigital electrode structure operating at low power density on a substrate surface converts electric signals into acoustic signals that can be focussed to high power densities and usefully applied at another location where the cutting stylus is located. Frequency response depends mainly upon the spacial periodicity of the interdigital-transducer (IDT) finger-electrode array and the number of finger electrodes, and not upon the dimensions of the acoustic medium. Power concentration of SAW results from the inherent nature of SAW to be confined within an acoustic wavelength of the substrate surface and, also, the focussing effect of the curved electrodes of the fan-shaped IDT.[2,3] The acoustic power and the displacement amplitude of the cutting stylus are determined by the number and length of the finger electrodes. Spacial separation between the IDT and the cutting stylus is highly advantageous for design optimization, since frequency response and displacement amplitude can be separately optimized.

Fundamental behavior of a quartz SAW recording stylus was studied and reported in Part 1.[2] The design was composed of a quartz plate having one end sharpened into a stylus tip and a fan-shaped IDT deposited on its shank. The IDT focusses SAW power at the stylus tip, and the tip acts as the cutting stylus. Practical devices of this one-body structure require a harder, more durable stylus material such as diamond. Since such materials are usually not piezoelectric, an auxiliary piezoelectric layer, such as zinc oxide, must be deposited over the IDT electrodes.

2. Structure of a New SAW Cutterhead and Driving Circuits

2.1 Pyramid-Shaped SAW Transducer

The new structure consists of a pyramid-shaped acoustic medium having fan-shaped IDTs deposited near the bottom of the sloping side surfaces of a pyramid and a cutting stylus mounted on the pyramid apex, as shown in Fig. 1. This composite structure simultaneously achieves SAW power concentration in an acoustic medium having sufficiently large size and, if desired, the durability of a diamond cutting stylus. As an acoustic medium, a piezoelectric material such as $LiNbO_3$ or PZT may be used. Nonpiezoelectric material such as metal or fuzed quartz may also be used by overlaying

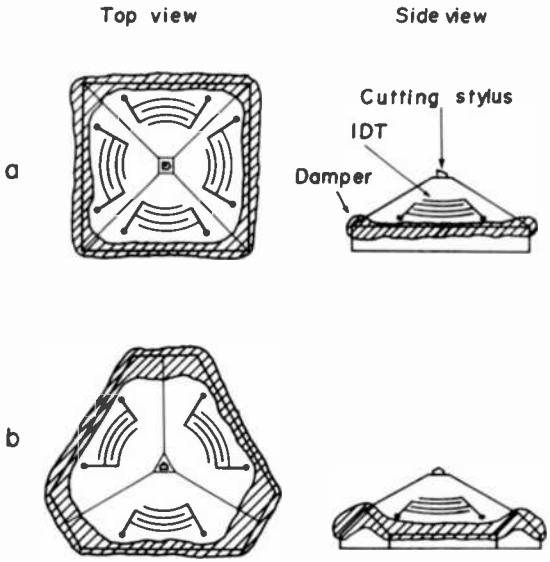

Fig. 1—Pyramid-shaped SAW transducer with cutting stylus: (a) square pyramid and (b) triangular (truncated) pyramid.

a thin layer of piezoelectric material, such as ZnO or PZT, onto the sloping side surfaces of the pyramid.

2.2 Frequency Response of the SAW Transducer

The radiation resistance of a SAW transducer should have a smooth response over a wide frequency range. For video signals, for example, the range extends from about 1 MHz to about 10 MHz. The frequency response of an IDT consists of side lobes around a main lobe that is centered at a center frequency f_o. The center frequency f_o is determined by the SAW velocity U and the space periodicity λ_0 of the IDT finger electrode array. The bandwidth of the main lobe is approximately $1/N$, where N is the number of electrode pairs.[4] A simple way to obtain wide bandwidth is to use an IDT having only one electrode pair. The generated SAW power is proportional to the square of N for a given length of finger electrodes and for a given voltage applied to the IDT electrodes.[2] Since the voltage is limited by electrical discharge breakdown and the IDT dimension is limited by the practical size of the transducer structure (in this case a pyramid), a single-pair IDT may not be sufficient to obtain adequately high power at the apex.

To obtain a wide-range frequency response, Shibayama and his collaborators proposed two methods. One is to use IDTs having varied finger electrode periodicity.[5] Since each periodicity corresponds to a different center frequency, overlapping of the main lobes occurs and provides wide-range frequency response. Another method is to use a delay line.[5,6,7] Successive electrode pairs are driven by successively time-delayed signals. The signal velocity of propagation along the delay line is chosen to be equal to the SAW propagation velocity. With this structure, Shibayama et al[6] obtained an extended range frequency response using IDTs having several electrode pairs. Their idea can be directly applied to the present SAW stylus; the relatively large areas of the pyramid's sloping side surfaces provide adequate space for such electrode systems, and the reduction of the number of electrode pairs to obtain wide frequency response can be avoided.

Although an individual IDT structure can have a wide range of relatively smooth frequency response, mutual interaction between multiple IDT can cause oscillatory response. For example, a SAW radiated from one IDT on one sloping surface of the pyramid is picked up by the IDT on the sloping surface of the opposite side. This pickup interferes with the input driving signal. Since the phase of the output signal relative to the input signal depends upon frequency and also on the distance between interacting IDTs, oscillatory behavior appears in the system frequency response. This behavior is similar to that of a SAW stylus in which an input signal interferes with the signal reflected from the stylus tip.[2] The amplitude of this oscillatory behavior can be reduced by using a triangular pyramid structure. In this triangular pyramid structure, IDT pairs do not face each other as shown in Fig. 1. That is, no IDT is on the path of a SAW beam passing through the apex, and no interference occurs among IDTs. This was experimentally demonstrated as described later. Since the shape of the pyramid's periphery does not affect its operation, the corners of the triangular periphery can be truncated or rounded to save volume of the acoustic medium.

Isotropic materials, such as metals and PZT, require no special care in fabricating the triangular pyramid. For single crystals, such as $LiNbO_3$, crystal orientation should be taken into account, because SAW propagation speed and the electro-mechanical coupling constant depend upon the direction of SAW propagation relative to the crystal axes. For $LiNbO_3$, a Z-cut plate is convenient for forming a triangular pyramid because the crystal has three-fold symmetry around the Z-axis. In other crystal cuts, IDT design is possible but

more complicated. Each of the three IDTs should be separately designed for optimization.

2.3 Electrical Adjustment of Cutting Stylus Position

The tip of the cutting stylus should preferably move only vertically; this vertical motion is obtained for a stylus located at the SAW focal point, the pyramid apex center where the stylus sits (see Fig. 1). The IDTs are arranged symmetrically arround this focal point. The symmetrical arrangement suggests that the apex should oscillate only vertically at the focal point when the SAW signals generated from each IDT are all in phase. If the cutting stylus is not located at the optimal mounting point, the stylus tip will oscillate elliptically with an undesirable horizontal motion component. However, this horizontal component can be cancelled by electrically adjusting the IDT position with a phase shifter. A signal phase shift in an IDT corresponds to a shift of the IDT geometrical position. By electrical rearrangement of IDT positions, the focussing point can be shifted to the actual cutting stylus position. An error of IDT position on a sloping surface can also be electrically adjusted in the same fashion.

3. Performance Calculations

The power required to generate the vertical displacement amplitude u_o at the pyramid apex can be roughly estimated. Suppose that the angle made by the sloping pyramid surface and the pyramid's bottom surface is small and that the geometry approximates that of a flat plate. The radiated SAW is then concentrated at the center of the circularly arranged IDTs. In that case, the SAW amplitude is considered to be expressed by the Bessel function $J_o(kr)$, where $k = 2\pi/\lambda$ is the SAW wave vector and r the distance from the focal center. The vertical displacement amplitude u is given by

$$u = u_o J_o(kr),$$

and

$$u \sim u_o \sqrt{2/\pi kr} \cos(kr - \pi/4) \qquad \text{for } kr >> 1.$$

The SAW power density P_{SAW} is approximately expressed as

$$P_{SAW} \approx c(\delta u/\delta r)^2 U$$
$$\approx cU(k/\pi r)ur_o^2 \qquad \text{for } kr >> 1,$$

where U is the SAW propagation speed and c is the effective elastic constant associated with the SAW. The c value is approximated by ρU^2, where ρ is the density of the acoustic medium. Since the SAW power is confined within the wavelength distance λ of the surface, the power passes through the cross-sectional area $2\pi r\lambda$ and is focussed at the pyramid apex center. Because of the bi-directionality of the IDT, approximately the same amount of power is launched toward the periphery of the pyramid. This power is absorbed with the damper shown in Fig. 1. The total acoustic power P_a is then given by

$$P_a \approx 4\pi\lambda r\, P_{SAW} = 8\pi\rho U^3 u_o^2.$$

The acoustic power required for $u_o = 500$ Å (1000 Å peak-to-peak) for several materials is estimated and listed in Table 1. Strictly speaking, as a result of the interference effect mentioned in Sec. 2.2, the amount of power launched toward the periphery is not necessarily the same as that of the power launched toward the apex. A similar situation existed in the quartz styli studied in Part 1.[2] For simplicity, this interference effect was ignored in the above rough estimation.

As for the required power, PZT seems suitable as an acoustic medium. However, it should be noted that the SAW wavelength should be sufficiently longer than the cutting stylus mounting dimensions, and that this wavelength is shorter for acoustic materials with a slower SAW speed U. In the choice of the acoustic material, the practical size of the cutting stylus and the wavelength in the desired frequency range should be taken into consideration.

4. Experiments

4.1 Amplitude of Mechanical Displacement at the Apex of a Square Pyramid

The amplitude of mechanical motion at a pyramid apex without a stylus was measured as one of the basic performance parameters. A Y-cut $LiNbO_3$ plate ($2.5 \times 2.3 \times 0.5$ cm^3) was cut and polished into a square pyramid shape. The angle between the sloping and bottom surfaces was 10°. Each fan-shaped IDT, deposited on each of the pyramid's four sloping surfaces, had a periodic length λ_0 of 0.54 mm, three electrode finger pairs, an aperture angle of 56°, and an effective capacitance of about 15 pF. The distance between IDT center and apex was about 9 mm. One pair of IDTs was aligned along the Z-axis and had a center frequency f_o of 6.5 MHz corresponding to the Rayleigh mode. Another pair of IDTs aligned along

the X-axis had a center frequency of 8.5 MHz corresponding to a mode that leaks SAW energy into the bulk material.[5]

Acoustic power concentration at the pyramid apex was studied for these modes. Fine powder was scattered over the pyramid surfaces, and the powder particle motion stimulated by the modes was observed. The Rayleigh mode showed power concentration, but the "leaky" mode did not. In the experiments on apex motion amplitude, only the two IDTs aligned along the Z-axis were used. The IDT circuits were connected in parallel.

The IDT resistance was observed as a function of frequency with a YHP 4191A rf impedance analyzer. No tuning circuit was used in this experiment. The result is shown in Fig. 2. The resistance showed oscillatory behavior due to interference effects between opposing IDTs. Similar oscillatory behavior was observed in the SAW stylus reported in Part 1.[2] The SAW stylus corresponds to the pyramid structure with one of the two facing IDTs rotated 180° around the apex and folded into a single surface and a single IDT. In other words, a SAW transmitted from an IDT toward the apex and a SAW incident to the IDT after being launched from another IDT and passing through the apex in the pyramid case corresponds, in the previously discussed quartz stylus case, to a SAW transmitted to the tip and reflected from it. Thus the previous discussion on the SAW stylus structure can be applied to the pyramidal case. For the SAW stylus structure, it is known that input power is effectively converted to SAW power transmitted to the stylus tip which, in this case, corresponds to the pyramid apex. This occurs at the radiation resistance minima, but less effectively at the maxima, because of interference effects.[2]

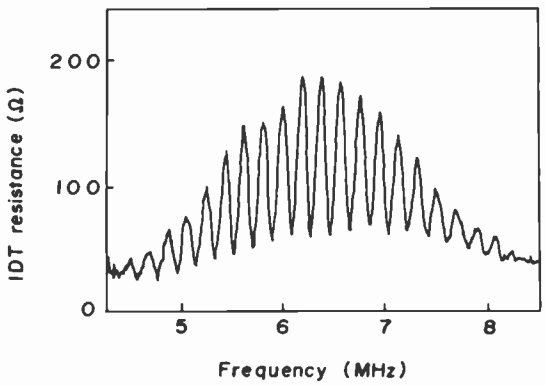

Fig. 2—IDT resistance, $LiNbO_3$ square pyramid.

The pyramid was mounted on a piezoelectric ceramic plate ($4 \times 4 \times 0.8$ cm^3) having a lowest resonance frequency f_r of 40.5 kHz. This frequency corresponds to a lateral size of the ceramic of 4 cm. At frequencies lower than 40.5 kHz, no resonance was observed. Apex motion was generated by applying a 6.4 MHz rf voltage to the IDTs, or by applying voltage at 5 kHz ($<<f_r$) to the ceramic oscillator. The ceramic oscillator is used as a mechanical motion reference that can be conveniently calculated from known constants of the material. An Au film deposited over the apex formed a capacitance with the stylus of a VideoDisc pickup shown in Fig. 3. Apex motion is detected as a capacitance change. The operation principle is similar to that of the signal readout from a VideoDisc.[8] The amplitude of the SAW-generated apex motion was compared with that of the known ceramic oscillator-generated apex motion. For valid comparisons, appropriate care was taken with the frequency response of the pickup assembly preamplifier.

An rf voltage at 6.4 MHz was applied across the IDT electrodes through a tuning circuit composed of an inductor and a capacitor, and the amplitude of apex motion was observed. The capacitive component of the IDT impedance was compensated and the resistance at the circuit entrance port was set at 50 Ω by adjusting the tuning circuit. The input power required to generate a motion amplitude of 1000 Å peak-to-peak was observed to be about 7 W, a value in fairly good agreement with the 11.5 W listed in Table 1. Similarly to the case of the quartz styli,[2] the voltage across the IDT electrodes was estimated. The estimation gave the value of 440 V peak-to-peak for an input power of 7 W. This value of the voltage is considerably lower than the discharge breakdown voltage estimated to be about 2.4 kV peak-to-peak.*

The frequency 6.4 MHz used in the experiment corresponds to the resistance minimum where the relatively low input power of 7 W was required. Here the conversion of input electric power to the SAW power transmitted to the pyramid apex is effective. At other frequencies corresponding to the resistance maxima, more power would be required for the same amount of mechanical motion amplitude at the apex. This expectation is based on the results from

* The value 2.4 kV peak-to-peak was estimated for an air gap between two parallel plate electrodes. The distance between the electrodes is 135 μm and is the same as that of the IDT used in the present experiments. The discharge breakdown experiments were carried out using a quartz stylus as reported in Part 1, Ref. [2]. The observed breakdown voltage was 1.6 kV peak-to-peak. This value is somewhat higher than the value 1.2 kV peak-to-peak estimated for two parallel plate electrodes having the same interelectrode distance of 40 μm.

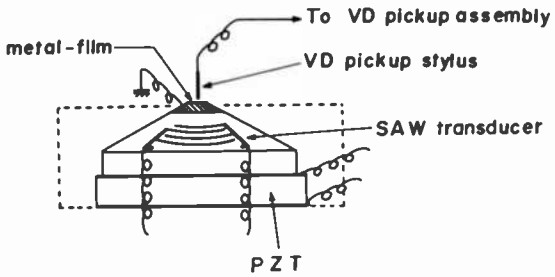

Fig. 3—Detection of pyramid apex motion.

the recording experiments described in Part 1.[2] Oscillatory behavior in the radiation resistance causes corresponding oscillatory behavior in the input power, and this causes some related SAW power to be transmitted toward the stylus tip. To obtain a smooth frequency response, the interference effect should be avoided.

4.2 Suppression of Interference Effect

Our method to avoid IDT interference effects is to use a triangular pyramid. The principle of this structure was described in Sec. 2.2. To avoid complexity arising from possible crystal anisotropy, an amorphous PZT material is used as the pyramid material. The fan-shaped IDTs have an aperture angle of 60°, consist of three electrode finger pairs, and have a center frequency f_o at 3.8 MHz. In the preparations to test this design, the radiation resistance of a square pyramid (3.5 × 3.5 × 0.8 cm^3; slope ~10°) was measured as a function of frequency. When two IDTs facing each other (180° apart) were used, oscillatory behavior was observed, similar to that of the $LiNbO_3$ square pyramid shown in Fig. 2. On the other hand, oscil-

Table 1—Required Acoustic Power

Material	$LiNbO_3$*	$LiNbO_3$#	PZT	Fused quartz	Duralumin	Titanium
Density ρ (g/cm^3)	4.6	4.6	7.8	2.2	2.8	4.5
SAW velocity U (10^5 cm/sec)	3.4	3.9	2.0	3.3	2.9	2.9
Wavelength (mm) at 6 MHz	0.57	0.65	0.33	0.55	0.49	0.48
Required power P_a (W)	11.5	17	3.9	5.0	4.4	7.0

* Z propagation on Y surface.
\# Y propagation on Z surface.

latory behavior did not appear when the IDTs were arranged orthogonally (90° apart). In the triangular pyramid, the three IDTs are arranged 120° apart from each other, and the amplitude of the oscillatory behavior was found to be suppressed to a few percent of that of the facing IDTs in the square pyramid structure. The small residual interference effect in the triangular structure seems to be due to SAW beam diffraction effects.

The orthogonal two-IDT arrangement in the square pyramid structure is not practical, because the arrangement is not symmetric with respect to the pyramid apex and the apex will not necessarily oscillate only vertically. It would also tend to oscillate with undesirable horizontal and tilting motion components. Symmetry considerations of the 120° arrangement suggests no such undesirable motion components. Accordingly, the triangular (or truncated triangular) pyramid seems the most promising geometry for a cutting transducer.

4.3 IDT Resistance and Apex Motion Amplitude of A Triangular Pyramid

A Z-cut $LiNbO_3$ plate was used to fabricate a triangular pyramid, taking into account three-fold crystal symmetry around the Z-axis. The 6-mm-thick plate was cut and polished into the shape of a truncated triangular pyramid. The shape of the pyramid bottom was then hexagonal, and its lateral size was about 3 cm. The angle between the sloping and bottom surfaces was 10°. Each fan-shaped IDT, deposited on each of the pyramid's three sloping surfaces, had six electrode finger pairs with a period of 0.58 mm, an aperture angle of about 52°, and a capacitance of about 25 pF. The distance between the IDT center and the apex was about 9 mm. Projection of the center line of the fan-shaped IDT to the Z-plane (bottom surface) is parallel to the Y-axis. The three IDTs were connected circuit-wise in parallel.

The IDT resistance was measured as a function of frequency with the result shown in Fig. 4. If spurious peaks are smoothed out, the resistance shows the well-known $(\sin x/x)^2$-type frequency dependence.[4] The smoothed resistance peaked at a frequency of about 7.2 MHz. This value is slightly higher than the center frequency of 6.7 MHz for Y-propagation on the Z-plane. The discrepancy is considered to be due to the 10° slope of the SAW propagation surface from the Z-plane. In contrast to the square pyramid case, the oscillatory behavior in the resistance was almost completely avoided using the triangular pyramid geometry. The spurious peaks were largely sup-

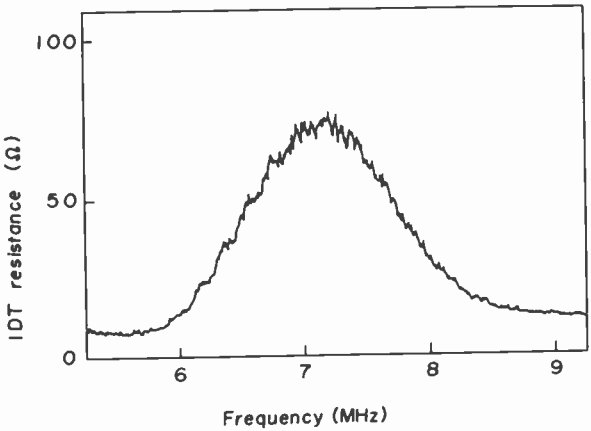

Fig. 4—IDT resistance ($LiNbO_3$ triangular pyramid).

pressed by applying an epoxy resin damper[9] around the pyramid's periphery, but some still remained and are observed in the result shown in Fig. 4.

Application of an input power of 9.0 W at 7.15 MHz across the IDT electrodes through a tuning circuit generated a motion amplitude of about 520 Å peak-to-peak at the pyramid apex. The tuning circuit was adjusted as mentioned in Sec. 4.1. Since the waveform of the signal from our power source became distorted when the power was further increased, the value for the input power corresponding to a motion amplitude of 1000 Å peak-to-peak was obtained by extrapolation of data at the low input power. The result for the input power was 33 W, and the corresponding value of the voltage at the IDT electrodes was estimated to be 580 V peak-to-peak. This value of voltage is considerably lower than the discharge breakdown voltage estimated to be 2.6 kV peak-to-peak.* The theoretical value of 17 W listed in Table 1 is corrected to 21 W by taking into account the increase in SAW velocity and the observed center frequency. The experimental value of 33 W is not unreasonably different from the theoretical value of 21 W. The discrepancy is considered to be due to the roughness of estimate of the various quantities used in the calculations, especially input power losses in the tuning circuit, the IDT electrodes, and elsewhere. These losses were ignored in the comparison mentioned above.

* The value 2.6 kV peak-to-peak was estimated for an air gap between two parallel plate electrodes. The distance between the electrodes was 145 μm, the same as that of the IDT used.

The applied voltage required for large mechanical amplitudes at the apex can be reduced by increasing the number of electrode finger pairs at a cost of narrower bandwidth, or by increasing the length of the finger electrodes as shown in Part 1.[2]

Propagation direction dependence of SAW velocity on the sloping side surfaces of the pyramid is not yet known, and the dependence was approximated with that known for the Z plane. SAW power concentration at the apex thus might not be very effective. Study of SAW propagation on the sloping surfaces are required to improve IDT design, especially the required curvature of the finger electrodes.

5. Discussion and Conclusions

Feasibility was demonstrated of using a SAW pyramid structure as a cutterhead transducer for high density signal recording, such as required for video recording. Signal frequency SAW are focussed at a pyramid apex after being launched from fan-shaped interdigital transducers deposited near the bottom of the sloping side surfaces of the pyramid. In this structure, the electric power density is low at the launch sites, and the acoustic intensity is high at the apex where mechanical motion is to be imparted to a diamond cutting stylus.

Adequately large mechanical amplitude (1000 Å peak-to-peak) was obtained at the apex of a square $LiNbO_3$ pyramid using 6.4 MHz SAW generated on two pyramid side surfaces. The applied voltages across the IDT electrodes and the input power to do this were 440 V peak-to-peak and about 7 W, respectively. At the apex of a triangular $LiNbO_3$ pyramid, the same amount of mechanical amplitude was obtained using 7.15 MHz SAW generated on three sloping surfaces. The corresponding voltage and the input power were 580 V peak-to-peak and 33 W, respectively. These values for both square and triangular $LiNbO_3$ pyramids agree fairly well with theoretically estimated ones and are comfortably lower than the electrical discharge breakdown limits. This fact suggests that design margins are large, thus allowing the possibility of wideband operation. The pyramids can be operated at frequencies where the radiation resistance (or conductance) is smaller, and a higher applied voltage is required than at the center frequency. That is, the frequency range for the required amplitude of cutterhead motion covers most of the frequency range for the IDTs used. The bandwidth of the IDT frequency range is inversely proportional to the number of the electrode finger pairs.

To operate the pyramid in the frequency range required for a

signal cutting tool, the frequency range of the IDTs should be expanded. This can be done by using a delay circuit, as reported elsewhere.

Another important factor is the smoothness of the cutterhead-motion amplitude versus frequency curve. It has been shown that the triangular pyramid is an appropriate geometry for a SAW transducer. Experiments using a square pyramid made of $LiNbO_3$ or PZT showed an oscillatory behavior in the radiation resistance versus frequency curve due to interference effects between opposing IDTs. Since the oscillatory behavior affects the frequency response of the motion amplitude, this behavior should be suppressed. Experiments using a $LiNbO_3$ or PZT triangular pyramid showed that the oscillatory behavior of the radiation resistance could be almost completely avoided because SAW from one IDT did not interfere with other IDTs.

Metal such as duralumin can also be used as a pyramid material. Although it requires a piezoelectric material deposited or bonded to the sloping side surfaces of the pyramid, the metal pyramid has advantages in electrical shielding, in heat removal, machinability, and in the techniques (e.g. swaging) for bonding a diamond cutting stylus to the apex.

In summary, a triangular pyramid shaped SAW transducer with its IDTs driven by a delay line and amplifiers seems to be close to the optimum acoustically-driven cutterhead for recording high-density video signals. To find optimum design conditions of the SAW transducer, further detailed studies are necessary. The studies should include such factors as the transducer material, SAW propagation on the sloping surfaces of a pyramid, IDT design, the driving electric circuitry, mounting of a cutting stylus onto a pyramid apex, stylus tip motion as a function of operating frequency, and the input drive voltage.

Acknowledgment

The authors wish to express their appreciation to Mr. E. O. Johnson for his continuous encouragement, helpful discussions, and reading of the manuscript. The authors are indebted to Dr. R. Shahbender of RCA David Surnoff Research Center, Princeton, for his critical reading of the manuscript and valuable suggestions.

References:

[1] J. B. Halter, US Patent 3,865,997, Feb. 11, 1975.
[2] S. Tosima, M. Nishikawa, T. Iwasa, and E. O. Johnson, *RCA Rev.*, **44**, p. 430, Sept. 1983 (this issue).

[3] S. Tosima, US Patent 4,281,407, July 28, 1981.
[4] W. R. Smith, H. M. Gerard, J. H. Collins, T. M. Reader, and H. J. Shaw, *IEEE Trans. Microwave Theory and Tech.*, **MTT-17,** p. 865 (1969).
[5] K. Shibayama, Kotai Butsuri, *Solid State Physics,* **5,** p. 589 (1970) (in Japanese). This review article includes the experiments cited in the text that were done by Shibayama and his collaborators. See also M. Toda, US Patent being applied.
[6] K. Shibayama, K. Yamanouchi, and K. Hyodo, 6th International Congress on Acoustics, Tokyo, Aug. 1968, H-1-3. See also M. Toda and E. Shima, US Patent being applied.
[7] T. O. Stanley, private communication, April 1, 1981.
[8] J. K. Clemens, *RCA Rev.,* **39,** p. 33 (1978).
[9] M. Toda and S. Osaka, *Trans. IECE Japan,* **E-60,** p. 237 (1977).

Patents Issued to RCA Inventors—Second Quarter 1983

April

J. Y. Avins and D. W. Phillion Circuit for Detecting Phase Relationship Between Two Signals (4,379,221)
S. L. Bendell Image Tube Suppression Circuit (4,379,310)
J. C. Bleazey Track Skipper for Video Disc Player (31,223)
R. W. Chambers, M. L. McNeely, and L. A. Torrington Apparatus for Molding a Recorded Disc (4,379,686)
A. M. Goodman Self Aligned Aluminum Polycrystalline Silicon Contact (4,380,773)
M. E. Hertzler and J. S. Stelzer Apparatus for Checking for Electrical FRIT Breakdown in Kinescopes (4,381,486)
R. W. Jebens Optical Focus Sensor (4,381,557)
L. A. Kaplan Current Amplifier (4,380,740)
W. L. Lehmann Input Selection Arrangement for Applying Different Local Oscillator Signals to a Prescaler of a Phase-Lock Loop Tuning System (4,379,271)
J. D. Mazgy Photocurrent Comensation for Electronic Circuitry Exposed to Ionizing Radiation (4,380,741)
P. Nyul Method for Supplying a Low Resistivity Electrical Contact to a Semiconductor Laser Device (4,380,862)
A. N. Prabhu and K. W. Hang Low Value Resistor Inks (4,379,195)
A. N. Prabhu and K. W. Hang Indium Oxide Resistor Inks (4,380,750)
G. A. Reitmeier and F. J. Marlowe Digital Error Detection Using Bracketing (4,380,069)
R. Torres and O. M. Woodward Loop Antenna Arrangement for Inclusion in a Television Receiver (4,380,011)
D. H. Ziegel Method and Apparatus for Sorting Stones (4,379,510)

May

T. N. Altman Video Disc Player With Multiple Signal Recovery Transducers (4,386,375)
J. G. Amery and J. H. Wharton Video Disc Systems With Plural Preemphasis/ Deemphasis Networks (4,385,326)
R. L. Angle Digital Control of Number of Effective Rows of Two-Dimensional Charge-Transfer Imager Array (4,382,267)
A. R. Balaban and S. A. Steckler Start-up Circuit for a Power Supply (4,385,264)
A. J. Banks Memory Conservation Method in a Programmable ROM Sync Generator System (4,386,368)
W. H. Barkow Television Deflection Yoke (4,383,233)
S. Berkman and J. F. Corboy Susceptor for Rotary Disc Reactor (4,386,255)
D. Botez and J. K. Butler Positive Index Lateral Waveguide Semiconductor Laser (4,383,320)
D. Botez Phase-Locked CDH-LOC Injection Laser Array (4,385,389)
D. J. Channin Liquid Crystal Lens Display System (4,385,805)
J. J. Colgan, Jr. Television Camera Tube Assembly and Electrical Contact for Target Electrode (4,384,233)
P. J. Coyle and M. S. Crouthamel Vacuum Lamination Fixture (4,382,833)
C. B. Dieterich Disc Record System Employing Signal Redundancy (4,382,299)
M. Ettenberg Optical Recording Medium and Information Record With Indented Overcoat (4,383,311)
J. B. George and W. J. Testin Phase Locked Loop Tuning Control System Including a Timed Sync Activated AFT Signal Seeking Arrangement (4,385,315)
J. B. George Wired Remote Control Apparatus for a Television Receiver (4,386,371)
W. G. Gibson and R. M. Christensen Vertical and Horizontal Detail Signal Processor (4,386,434)
L. A. Harwood and E. J. Wittman Filter and Phase Shift Circuit for a Television Automatic Flesh Color Correction System (4,385,311)

L. A. Harwood and R. L. Shanley, 2nd Clamping Arrangement for a Video Signal Peaking System (4,386,370)
R. B. Hollo Static Discharge Device (4,385,824)
R. E. Hunter, Jr. TV Interface RF Modualation Circuitry (4,386,377)
H. F. Inacker and E. L. Henderson Temperature Compensation of a Flux Drive Gyromagnetic System (4,382,237)
K. C. Kelleher Video Disc Player With RFI Reduction Circuit Including an AGC Amplifier and Dual Function Peak Detector (4,385,374)
S. W. Kessler, Jr. and R. E. Reed Center Gate Transcalent Device (4,386,362)
C. P. Kocher and A. Abramovich Television Remote Control System for Selectively Controlling External Apparatus Through the AC Power Line (4,386,436)
F. C. Liu Variable Peaking Control Circuit (4,384,306)
S. Liu Method for Enhancing Electron Mobility in GaAs (4,383,869)
B. E. Lock Method and Apparatus for Separating a Stamper From a Mold (4,381,964)
D. W. Luz and D. H. Willis Television Receiver, Push-Pull Inverter, Ferroresonant Transformer Power Supply Synchronized With Horizontal Deflection (4,385,263)
J. Makino Video Disc Player With a Freeze Frame Feature (4,383,276)
M. E. Malchow Automatic Gain Control Arrangement Useful in an FM Radio Receiver (4,385,400)
R. U. Martinelli, N. W. Brackelmanns, and P. H. Robinson High-Current, High-Voltage Semiconductor Devices Having a Metallurgical-Grade Substrate (4,383,268)
V. D. McGinniss ESR Analysis of Conductive Video Disc Components (4,386,319)
M. L. McNeely and H. Rees Method for Producing Injection Molded and Centrally Apertured Disc Records (31,235)
R. M. Mendelson Self-Quenching Circuit (4,382,192)
F. R. Nyman, B. N. Stevens, and L. Ekstrom Drying Process for Video Discs (4,383,961)
J. J. Prusak Cathode Head (4,385,978)
A. Rosen Method for Fabricating a Low Loss Varactor Diode (4,381,952)
P. M. Russo Double Layer Liquid Crystal Device for a DOT Matrix Display (4,384,763)
O. H. Schade, Jr. Amplifier Circuits (31,263)
R. L. Schelhorn Structure for Mounting a Semiconductor Chip to a Metal Core Substrate (4,383,270)
H. G. Schwarz Composite Video Signal Limiter (4,384,302)
R. L. Shanley, 2nd and R. P. Parker Compensated Clamping Circuit in a Video Signal Peaking System (4,386,369)
G. A. Swartz Electrolytic Etch for Eliminating Shorts and Shunts in Large Area Amorphous Silicon Solar Cells (4,385,971)
B. K. Taylor Video Disc Player Having Stylus Position Sensing Apparatus (4,382,292)
I. T. Wacyk and R. G. Stewart Pulse Generating Circuit Using Current Source (4,386,248)
P. P. Webb Avalanche Photodiode and Method of Making Same (4,383,267)
C. M. Wine Single Button Control (4,385,204)

June

R. Amantea and C. F. Wheatley, Jr. Transistor With Improved Second Breakdown Capability (4,388,634)
R. L. Angle CCD Triple-Split Gate Electrode Transversal Filter (4,387,354)
N. A. Arroyo, N. V. Desai, and J. F. Buchanan Method to Determine Carbon Black Content (4,388,410)
W. E. Babcock and F. S. Wendt Television Receiver Ferroresonant Power Supply Using a Two-Material Magnetizable Core Arrangement (4,390,819)
A. R. Balaban, S. A. Steckler, and R. E. Fernsler Television Receiver High Voltage Protection Circuit (4,389,676)
A. J. Banks TV Sync Generator System for PAL Standards (4,390,892)
A. E. Bell Optical Recording Medium and Information Record With Tracking Aid (4,387,381)

J. M. Bessolo and J. E. Gillberg Watch Circuit With Oscillator Gain Control (4,387,350)
H. Chen Color Picture Tube Having an Expanded Focus Lens Type Inline Electron Gun With an Improved Stigmator (4,388,553)
D. Chin, J. G. Henderson, and R. J. Maturo Tuning Display for a Television Receiver (4,390,902)
C. A. Clark, Jr. Self-Starting Transformer-Coupled FET Multivibrators (4,390,937)
P. Datta, E. S. Poliniak, and V. S. Ban High Density Information Record Lubricants (4,389,441)
P. Datta and E. S. Poliniak Doped Polyphenylene Ether Lubricant for High Density Information Discs (4,390,579)
W. F. Dietz Integrated Circuit Interface in a Vertical Sync Circuit (4,387,397)
R. A. Dischert and G. A. Reitmeier De-Emphasis for Digitized Composite Color Television Signals (4,388,638)
D. L. Dodds Electron Beam Influencing Apparatus Incorporating Vertical Beam Movement Function (4,388,602)
P. T. Greninger Color Picture Tube Having an Improved Expanded Focus Lens Type Inline Electron Gun (4,388,552)
P. D. Griffis Semiconductor Apparatus With Integral Heat Sink Tab (4,387,413)
J. R. Harford AFT Lockout Prevention System (4,388,649)
L. A. Harwood, R. L. Shanley, 2nd, and J. Hettiger Predictably Biased DC Coupled Video Signal Peaking Control System (4,388,647)
L. A. Harwood, R. L. Shanley, 2nd, and J. Hettiger Frequency Selective DC Coupled Video Signal Control System Insensitive to Video Signal DC Components (4,388,648)
R. E. Harwood Method of Forming Reference Flats on Styli (4,387,540)
L. V. Hedlund, D. G. Herzog, and F. L. Putzrath Search-Mode Arrangement for VTR (4,388,657)
J. G. Henderson and R. J. Maturo Carrier Detector Apparatus Useful in a Multiband Sweep Type Tuning System (4,387,401)
W. Hinn Automatic Kinescope Bias Control System With Digital Signal Processing (4,387,405)
K. Katagi Apparatus for Angularly Scanning Memory Addresses (4,387,370)
E. O.Keizer Technique for Uniform Stylus Configuration (4,388,714)
C. W. Key and E. W. Christensen, 2nd Apparatus for Influencing Electron Beam Movement (4,390,815)
M. F. Leahy Calibration Device and Method for an Optical Defect Scanner (4,386,850)
H. W. Lehmann, K. Frick, and R. W. Widmer Reactive Sputter Etching of Aluminum (4,387,013)
A. L. Limberg Adjustable-Gain Current Amplifier for Temperature-Independent Trimming (4,389,619)
L. W. Martinson Multi-Purpose Retimer Driver (4,387,341)
G. N. Mehrotra Video Disc Player With Selectively Enabled Audio Signal Expander Circuitry (4,388,654)
K. D. O'Mara Method of Making a Laminated Recorded Disc (4,390,487)
T. R. Pampalone Sulfur Dioxide Cured Coatings (4,389,433)
J. D. Pollack Carriage Translating Mechanism for Video Disc Player (4,390,978)
J. P. Powell Sensing Focus of a Color Kinescope (4,387,394)
R. N. Rhodes Color Filter Having Vertical Color Stripes With a Nonintegral Relationship to CCD Photosensors (4,388,640)
J. A. Strother Low-Distortion Detection of Pulses Superimposed on an Unknown and Variable Background Signal (4,388,646)
D. M. Weber and R. A. Alleman Method of Etching Apertures Into a Continuous Moving Metallic Strip (4,389,279)
D. H. Willis Remote Responsive Television Receiver Ferroresonant Power Supply Protection Circuit (4,387,324)
D. H. Willis Television Receiver Ferroresonant Load Power Supply Disabling Circuit (4,390,820)
C. M. Wine Video Disc Player Having Auxiliary Vertical Synchronizing Generator (4,387,407)

AUTHORS

Stanley Bloom received a BS degree in physics and mathematics from Rutgers University in 1948, and a PhD in physics from Yale University in 1952. His dual thesis was on ion clustering in gases and on the theory of spectral-line broadening. He joined RCA Laboratories in 1952 and is a Senior Member, Technical Staff. He has worked on electron-beam microwave tubes, quantum electronics, plasmas, parametric amplifiers, and energy-band theory of semiconductors. More recently, he has been involved in studies of cathodoluminescence and of electron optics with emphasis on flat-panel television and on color-tube focus masks.

Dr. Bloom served as Head, Electron Tube Devices from 1961 to 1966. In 1966 he was awarded an RCA Laboratories Overseas Fellowship for a year of study in solid-state physics at the University of Cambridge. He has received five RCA Laboratories Outstanding Achievement Awards, three for work on noise reduction in traveling-wave tubes, one for work on semiconductor alloys, and one for work on focus masks. Dr. Bloom is a senior member of the IEEE and has been active on IEEE standards committees and research conference committees. He is also a member of the American Physical Society and Phi Beta Kappa.

Basab B. Dasgupta received his B.Sc. and M.Sc. degrees in physics from the University of Calcutta, India and Ph.D. degree from the University of Wisconsin in 1976. He worked as a faculty member of physics at two different campuses of the University of Wisconsin system and as a member of the Electrical Engineering faculty at Marquette University. His area of research has involved electronic, electromagnetic, and acoustic properties of solid surfaces. He joined RCA Consumer Electronics in 1981 as a member of the engineering staff associated with the Advanced Yoke Development group.

E. F. Hockings received the Ph.D. degree in chemistry from the University of London, England. He joined RCA Laboratories in 1957, where he worked on the preparation and properties of ternary compound semiconductors for use in thermoelectric cooling and power generation. Subsequently he was involved with the preparation of magnetic materials for digital recording in disc storage devices. He has also worked on insulators for electron-gun structures in picture tubes. More recently, he has been concerned with the design and evaluation of high-transmission color-selection masks for use in picture tubes.

Dr. Hockings is a member of the Society of Chemical Industry and a Fellow of the Royal Society of Chemistry.

John Howard received the B.Sc. degree in Electrical and Electronic Engineering at University College, Cardiff, Wales in 1974 and the M.Sc. degree in Microwaves and Modern Optics at University College, London in 1975. In 1981 he received the Ph.D. in E.M. Theory at Chelsea College, University of London. In 1978, he worked for British Aerospace, Stevenage, U.K. From 1978 to 1982, he was with Marconi Space and Defence Systems Ltd., Frimley, U.K.. In 1982 he joined RCA Astro Electronics, Princeton, N.J.. He is presently with Narda Microwave Corp., Hauppauge, N.Y. His main interests include E.M. theory, microwave propagation, filter theory, passive and active microwave components and subsystems, and antennas.

He is a member of the Institution of Electrical Engineers (U.K.) and a Senior member of the Institute of Electrical and Electronic Engineers (U.S.A.).

Sheng T. Hsu received the B.S. degree in electrical engineering from National Taiwan University, Taipei, Taiwan, in 1958, the M.S.E.E. degree from National Chiao-Tung University, Hsienchu, Taiwan, in 1960 and the Ph.D. degree in electrical engineering from the University of Minnesota, Minneapolis, in 1966. From 1966 to 1970, he was with Fairchild Semiconductor Research and Development Laboratory, Palo Alto, California, as a Member of the Technical Staff. From 1970 to 1972, he was an Assistant Professor of the Department of Electrical Engineering, University of Manitoba, Winnipeg, Man., Canada. He is now a staff member of RCA Laboratories, Princeton, N.J., working on semiconductor devices and VLSI technologies.

Tatsuru Iwasa obtained the BSEE degree from the University of Kogakuin in 1970. From 1970 to 1971 he was in a post-graduate course at the University of Kogakuin. He joined RCA Research Laboratories, Inc., Tokyo, in 1965 where he worked on transport phenomena in ferromagnetic semi-conductor chalcogenide spinels, acoustic surface-wave devices, and piezoelectric thin-film materials. Since 1978 he has been a study-student at the Cancer Institute in Tokyo and has been engaged in the study of the biophysics and biochemistry of DNA. In 1982 he became a technologist in the Corning Research Center of Corning Japan Inc. where he has been doing research on electronic materials.

Mr. Iwasa is a member of the Institute of Electronics and Communication Engineers of Japan, the Physical Society of Japan, the Surface Science Society of Japan, the Japanese Biochemical Society, and the Japanese Cancer Association.

Edward O. Johnson received a BSEE degree from Pratt Institute of Brooklyn in 1948 and attended graduate courses at the Swiss Federal Institute of Technology and at Princeton University. In 1948 he joined RCA Research Laboratories where he worked in plasma physics to help develop gas plasma analogues to the transistor, double probe methods which have been widely used in ionospheric and plasma research, semiconductor surface measurement techniques, and concepts for understanding the limits of solid-state

device performance. In various managerial capacities from 1959 to 1972, he was with the Solid-State and Tube Products Divisions, and from 1973 to 1975 with Licensing Operations. From 1975 to 1982 he was director of the RCA Research Laboratories in Tokyo, Japan. In 1982 he transferred to Corning Research, Inc., in a similar capacity.

In 1953, with W. M. Webster, he received the IEEE Editor's Award, and in 1960 the Eta Kappa Nu Recognition. In 1966 he was a member of the U.S. Department of Commerce Panel on Electric Automobiles. He has received several RCA achievement awards and has over 30 issued patents.

Masayoshi Nishikawa obtained his BSEE degree from Kanagawa University in 1973. He joined RCA Research Laboratories, Tokyo, in 1973, where he performed research in the field of surface acoustic waves in piezo crystals and ceramics. Mr. Nishikawa is currently a Technologist in Corning Japan Incorporated. He is a member of the Institute of Electronics and Communication Engineers of Japan.

Donald J. Tamutus attended St. Bonaventure University, University of Heidelberg and Rutgers University. After a tour in the U.S. Army, he joined RCA Laboratories in 1962, and is presently Manager, Process Technology. He is responsible for photo artwork generation, printed circuits boards and etched masks, electrodischarge and ultrasonic machining, electrochemical deposition, precision grinding, optical polishing, and chemical control for the Laboratories. He has worked on a number of projects including photovoltaic systems, metalized bead suppressor for TV, flat panel television and Video Disc. In 1981 he was awarded an RCA Laboratories Outstanding Achievement Award.

Soitiro Tosima received the B.Sc. degree in physics from Kyushu University in 1951, and the D.Sc. degree in physics from Osaka University in 1962. From 1953 to 1961, he was a Research Associate in the Physics Department of Kyushu University. He joined RCA Research Laboratories, Tokyo, in 1961. In 1964, he spent six months as a visiting research scientist at RCA Laboratories in Princeton. In 1965, Dr. Tosima became manager of the Applied Physics Group. His principal areas of interest have been the theories of transport phenomena in semiconductors, semimetals, and ferromagnetic semiconductors, particularly at high electric fields; instabilities in solid state plasmas; and magnetic bubbles. More recently his areas of interest have been high intensity surface acoustic waves and the physics of the soldering process. In 1982 he transferred to Corning Research, Inc., in Japan.

Dr. Tosima is a member of the Physical Society of Japan.